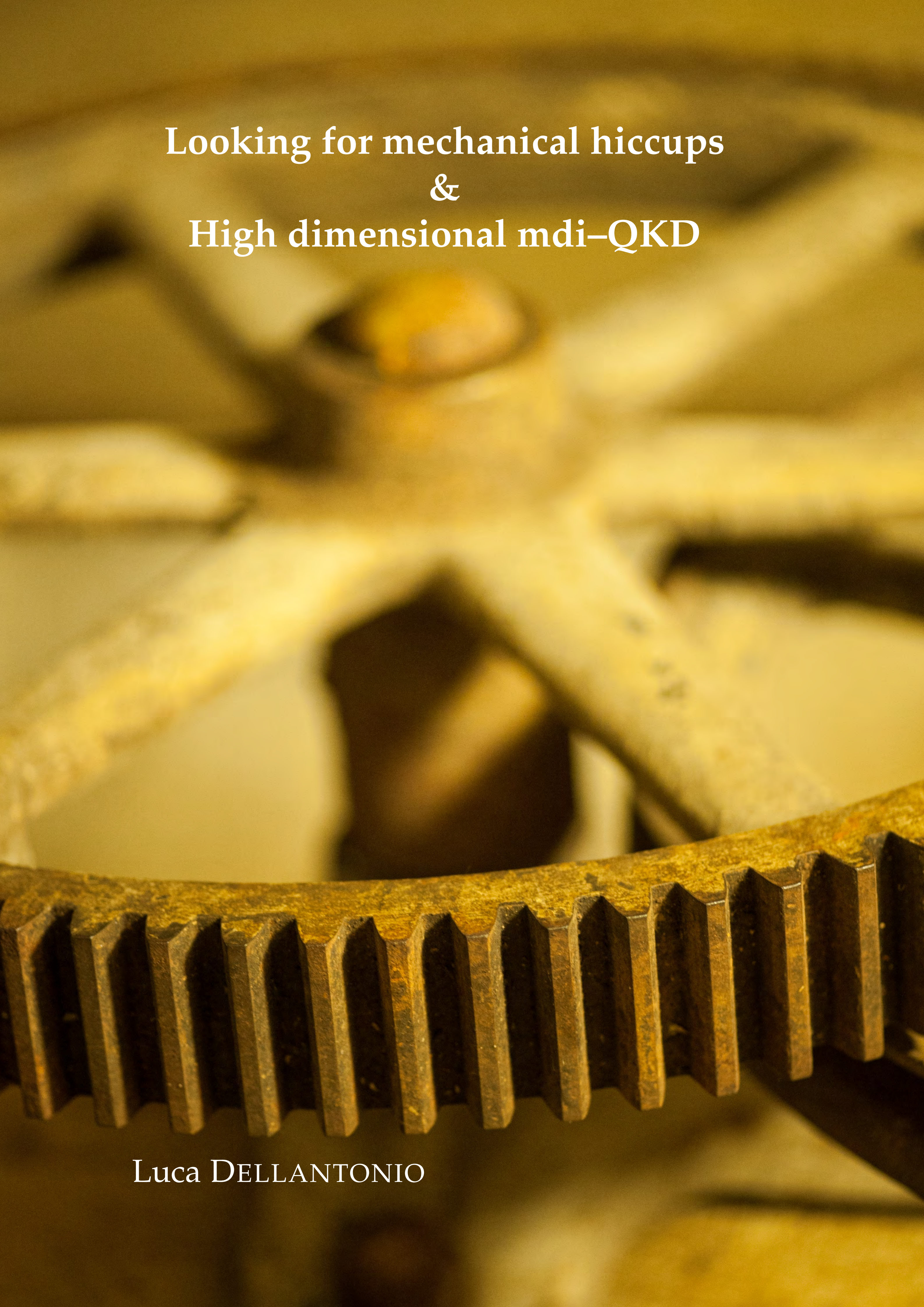

Looking for mechanical hiccups
&
High dimensional mdi–QKD

Luca Dellantonio

University of Copenhagen

Niels Bohr Institute

Looking for mechanical hiccups & High dimensional mdi–QKD

Ph.D. thesis

Author:
Luca Dellantonio

Supervisor:
Prof. Anders S. Sørensen

This thesis has been submitted to
the Ph.D. School of the Faculty of Science, University of Copenhagen

October 1, 2018

To everyone who made these beautiful years

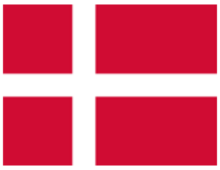

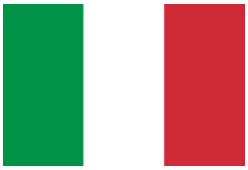

UNIVERSITY OF COPENHAGEN

Abstract

Niels Bohr Institute
Faculty of Science

Ph.D. thesis

Looking for mechanical hiccups
&
High dimensional mdi–QKD

by Luca DELLANTONIO

The fields of opto- and electromechanics have facilitated numerous advances in the areas of precision measurement and sensing, ultimately driving the studies of mechanical systems into the quantum regime. To date, however, the quantization of the mechanical motion and the associated quantum jumps between phonon states remains elusive. For optomechanical systems, the coupling to the environment was shown to preclude the detection of the mechanical mode occupation, unless strong single photon optomechanical coupling is achieved. Here, we propose and analyse different setups, which allow us to overcome this limitation and resolve the energy levels of a mechanical oscillator. We find that the heating of the membrane, caused by the interaction with the environment and unwanted couplings, can be suppressed for carefully designed electromechanical systems. The results suggest that phonon number measurement is within reach for modern technology.

Quantum key distribution (QKD) provides ultimate cryptographic security based on the laws of quantum mechanics. For point–to–point QKD protocols, the security of the generated key is compromised by detector side channel attacks. This problem can be solved with measurement device independent QKD (mdi–QKD). However, mdi–QKD has shown limited performances in terms of the secret key generation rate, due to post–selection in the Bell measurements. We show that high dimensional (Hi–D) encoding (qudits) improves the performance of current mdi–QKD implementations. The scheme is proven to be unconditionally secure even for weak coherent pulses with decoy states, while the secret key rate is derived in the single photon case. Our analysis includes phase errors, imperfect sources and dark counts to mimic real systems. Compared to the standard bidimensional case, we show an improvement in the key generation rate.

UNIVERSITY OF COPENHAGEN

Dansk Resumé

Niels Bohr Institute
Faculty of Science

Ph.D. thesis

Looking for mechanical hiccups
&
High dimensional mdi–QKD

by Luca DELLANTONIO

Brugen af opto- og elektromekanik indenfor præcisionsmåling og sensing har ført til stor fremgang i feltet og har bragt studiet af mekaniske systemer til det kvantemekaniske regime. På trods af den øgede interesse for området, er kvantiseringen af den mekanisk bevægelse og de tilhørende kvantespring mellem fonon-tilstandene endnu ikke blevet observeret. Koblingen af optomekaniske systemer til omgivelserne har vist sig at forhindre detektion af af populationen af mekanisk tilstande medmindre en stærk enkelt-foton optomekanisk kobling opnås. Vi foreslår og analyserer her alternative metoder til at overvinde denne begrænsning og derved observere energiniveauerne af en mekanisk oscillator. Vi viser, at opvarmningen af membranen ved interaktion med omgivelserne gennem uønskede koblinger kan undertrykkes i omhyggeligt designede elektromekaniske systemer. Resultaterne tyder således på, at en måling af antallet af fononer er indenfor rækkevidde for moderne teknologi.

Quantum key distribution (QKD) giver ultimativt kryptografisk sikkerhed baseret på kvantemekaniske love. For punkt-til-punkt QKD protokoler, trues sikkerheden af den genererede kode af detektor-sidekanal-angreb. Dette problem kan håndteres ved måleapparat-uafhængig QKD (mdi–QKD). For mdi-QKD er der dog begrænsninger i raten, hvormed kodenøglen genereres på grund af post-udvælgelse i Bell-målingerne. Vi viser her, at højdimensional (Hi-D) kodning (qudits) forbedrer opførslen af de nuværende mdi-QKD implementeringer og at det er ubetinget sikkert også for svage kohærente pulser med lokke tilstande. Desuden udleder vi kode-raten i enkelt-foton tilfældet. For as simulere rigtige systemer indeholder vores analyser fase fejl, ufuldkomne kilder og mørke tællinger og viser en forbedring i kode-raten sammenlignet med det almindelige bidimensionale tilfælde.

Acknowledgements

For the friends expecting these acknowledgments to be 'creative', I apologize. With few hours left to the submission deadline, I have no time to thank everybody, but just those directly involved in this thesis. At least, I add a pinch of pathos, since this last page really is a race against Time.

First, I would like to thank Anders. I will always remember our little chit chats in the morning, the irreverent jokes, and the challenge of proving him wrong. The latter not being an easy task, the time I was the nearest he told me: "In being wrong, you were actually right". And, of course, he was correct. How annoying is that? Anyway, since a good work environment is fundamental for happiness, I thank him for that. And even if the group is not made only by him, I am convinced that a nice group is found where a good supervisor resides. And we surely have a very positive and constructive atmosphere. Even if he never admitted that I have been his best PhD student (despite I asked him), once he told me that I surely was the funniest (hopefully not *because* I asked him). I consider this to be a moral victory and decided to be satisfied. Wherever I'll be, I am going to miss Anders.

Another person very much related with my PhD is Florian. I had the luck of spending almost 5 months with him, during which I learned new techniques and found new wonderful friends. Florian and his group made my stay in Erlangen just fantastic, and I hope to have other chances to spend more time there.

The work done during my PhD, as it is presented here, wouldn't have been possible without Sasha and Davide. They guided me in deriving many results, always with a positive attitude and a ready laugh. I couldn't have hoped for better help.

I thank Jessica, Camille, Rodrigo, Giulia, and Martina for helping with the manuscript. I like to think that there is a little bit of all of them in the next pages.

Finally, I thank (again) Martina for the moral support throughout these years, which has been considerably intensified in the last weeks of writing.

For all those who I did not mention, recall that this thesis is dedicated to you. You, that really made these beautiful years, and every day a new adventure.

Per tutti gli assenti, sappiate che questa tesi è dedicata a voi. Voi, che avete reso questi ultimi anni eccezionali, e ogni giorno una piccola nuova avventura.

Contents

List of Figures

Chapter 1

Introduction

In this manuscript, we present the work of the past three years. With our results on spin squeezing summarized elsewhere [1, 2], we focus on electromechanics, optomechanics and quantum key distribution (QKD). In chapter 2, we expand the results of Ref. [3] on the phonon quantum nondemolition (QND) measurement. Chapter 3 contains unpublished work, that generalizes Ref. [3] to the optical domain. We investigate possible strategies to increase the secret key rate in measurement device independent (mdi) QKD [4] in chapter 4, and finally present conclusions and outlooks in chapter 5.

1.1 Looking for mechanical hiccups

Energy quantization is one of the hallmarks of quantum mechanics. First theorized for light by Einstein and Planck, it was found to be ubiquitous in nature and represents a cornerstone of modern physics. It has been observed in various microscopic systems starting from nuclei, atoms, and molecules, to larger mesoscopic condensed matter systems such as superconductors [5]. For macroscopic systems, however, the observation of energy quantization is hindered by the smallness of the Planck constant. Thus, although being a milestone of contemporary physics, up to date the discrete energy spectrum of mechanical resonators has never been seen directly.

Extreme progress in studying mechanical systems has been achieved in experiments exploiting radiation pressure. This is the core of optomechanics [6], where photons and phonons of the optical and mechanical subsystems interact with each other. A similar type of coupling can be realized in the microwave domain with electrical circuits, leading to the field of electromechanics [7, 8, 9, 10, 11, 12]. The numerous advances of optomechanics and electromechanics include ground state cooling [13, 14, 8, 15, 9, 16], ultra precise sensing [17, 18, 19, 20, 21], generation of squeezed light and mechanical states [22, 23, 24, 11, 12], back action cancellation [25, 26], and detection of gravitational waves [27]. In all of these systems, however, the operation in the single photon/phonon regime is challenging due to the small value of the bare coupling [7, 28]. Instead, experiments exploit an enhanced linearized effective coupling induced by a large driving field. This severely limits the nature of the interactions [29] and possible quantum effects. In particular, it precludes the observation of the energy quantization in mechanical resonators.

Our work extends the available interactions in opto- and electromechanics. We provide a theoretical framework that allows determining if, for a given experimental setup, nonlinear interactions do play a role, or are hindered by other couplings. This is crucial if the realm of mechanical oscillators wants to be extended to computing or other complex tasks. Whether this will be useful or not, depends on future developments of other platforms. For instance, ions and neutral atoms have long coherence times and allow for high fidelity gates (single and two qubits) [30, 31].

However, despite substantial progress in building up bigger lattices [32, 33], these systems are hardly scalable. Moreover, arbitrary two-qubit gates are generally challenging, with often only next-neighbour interactions available. Quite the opposite is true for superconducting circuits and artificial atoms [30]. Sitting on a junk of nuclear spins and/or other noise sources, dephasing is a central issue, with coherence times limited to few microseconds [34]. However, scalability is considered to be quite straightforward[1], and gate fidelities have proven to approach unity [35]. Both kinds of platforms managed to run simple quantum algorithms with small computational depths [36, 37], but did not irrefutably prove the so-called quantum supremacy [38]. Mechanical oscillators, on the other side, have both long coherence times [39], and can be built in arrays of potentially unlimited elements. Big enough to make the fabrication deterministic, but small to fit millions in a squared decimetre, their operational time can be of few microseconds, and can be interfaced with optical or microwave light. These advantages come at the cost of a small interaction strength, consequence of their 'macroscopic' sizes, and a potentially noisy environment. Despite experiments have demonstrated nonlinear interactions in optomechanical systems [40, 41], it is not yet clear how to exploit these for computing purposes. As such, the role of mechanics in quantum information is limited to few auxiliary applications. For instance, membranes could act as transducers [13, 42] in a hybrid machine, or could be used to deterministically change the light propagation direction [43]. Alternatively, their long coherence could be used for storage purposes[2], in a similar scheme to the one proposed by Gorshkov et al. for atomic ensembles [44]. In chapters 2 and 3, we discuss about phonon QND measurement. Already investigated [45, 46, 47, 48, 49] but never accomplished, we determine the main limitations and prove that it is available for current technologies. What will be useful for, and the outlook for future researches, is discussed in chapter 5.

1.2 High dimensional mdi–QKD

Digital security is important for several aspects of modern life. Classical cryptography only promises to make decryption hard, but not impossible. On the contrary, quantum key distribution (QKD) is based on the laws of physics, theoretically allowing parties to share cryptographic keys in an unconditionally secure way [50]. However, several physical requirements have to be satisfied to provide unconditional security, and most experimental implementations of QKD have proven to be vulnerable to attacks [51, 52, 53, 54, 55, 56, 57, 58, 59, 60]. These attacks mainly exploit weaknesses in the detectors, whereas the sources are less vulnerable. To overcome this limitation, device independent (di–QKD) [61, 50, 62, 63], and measurement device independent QKD (mdi–QKD) [64] were introduced to decrease the reliance on the physical setup. While di–QKD remains challenging due to technical limitations, including the need for extremely efficient detection [50], mdi–QKD is ready to be implemented in real networks.

Mdi–QKD was introduced by Lo et al. in Ref. [64]. Here, the two parties Alice and Bob only use photon sources, while the detection is performed by a third party, Charlie. Different degrees of freedom have been used to demonstrate the feasibility of this scheme (e.g.: polarization, phase, time, and space) [64, 65, 66]. Compared to other QKD protocols, however, mdi-QKD has shown low key generation rates. To reduce this limitation, high-dimensional (Hi–D) encoding can be used to improve

---

[1] Fabrication imperfections in the devices may be, however, a limiting factor for the next years.

[2] Currently under development in the group.

the photon information efficiency (PIE) [67]. Recent results have shown how spatial or temporal modes can be used to increase the dimension of the Hilbert space [68, 69, 70, 71, 72] for standard QKD. We propose a protocol, where Alice and Bob generate qudits (quantum states in N–dimensions) encoded in different paths or time slots of the photons. These photons then interfere at Charlie's Beam Splitters (BS), as shown in Fig. 4.1. As discussed below, the measurement projects the qubits into a two dimensional subspace, which can be used for QKD. In the following, we analyse this high dimensional mdi–QKD protocol, considering the main sources of errors, such as imperfect photon generation, dark counts and (unknown) phase shifts. We prove that high dimensional mdi–QKD is unconditionally secure for coherent states with the decoy state technique [64, 73], and analyse the key generation rate for single photon sources. In analogy to a similar result for standard QKD [72], we find that our Hi–D mdi–QKD protocol is advantageous, particularly in the detector saturation regime, where the time between photon clicks at Charlie's detectors is comparable to the detectors' dead time τ_d. We study the protocol both for time and space encoding and analyse the practical constraints that make one encoding better than the other. A different Hi–D mdi–QKD scheme was proposed in Ref. [67], but remains experimentally unfeasible, since discriminating Bell states in high dimensions is impossible by simple means [74, 75]. In comparison, our protocol can be implemented without a significant increase in the complexity of existing setups. In particular, for weak coherent states and time encoding, no change in the hardware is required.

Chapter 2

QND measurement for mechanical motion quanta

In this chapter, we present the results summarized in [3]. In section 2.1, we explain the main results, allowing the reader to understand the potential and problems of the setup. Later on in section 2.2, we present the derivations. Conclusions are then given in section 2.3.

2.1 Main results

Quantization of mechanical energy can be observed by a quantum nondemolition (QND) measurement [76, 77] of an oscillator's phonon number operator $\hat{n}_\mathrm{b}$. Here, QND means that the interaction, which couples the mechanical system with the measurement apparatus, does not affect the observable we are interested in. This is achieved if the total Hamiltonian commutes with $\hat{n}_\mathrm{b}$, and the influence of the environment is minimized. Considering the electromechanical setups in Fig. 2.1, we show that QND detection is feasible for a capacitor in which one of the electrodes is a light micromechanical oscillator. By choosing an antisymmetric mode for the oscillator, the interaction between the electrical and mechanical subsystems is quadratic in the displacement. Along with the suppression of the linear coupling, this ensures the QND nature of the measurement, as originally proposed in Refs. [45, 46] for an optomechanical system. In that system, however, it was shown in Refs. [78, 79] that the combination of unwanted losses and the coupling to an orthogonal electromagnetic mode spoils the interaction, unless strong single photon coupling is achieved. Here, we show that for the considered electromechanical setup the equivalent orthogonal mode can have dramatically different properties, allowing for the phonon QND detection. We derive general conditions under which the QND measurement is possible, and characterize its experimental signatures. As compared to previous approaches to phonon QND measurement [45, 46, 47, 48, 49], our procedure does not impose stringent requirements on the single photon optomechanical coupling, but relies on the ratio of the involved coupling constants. This makes our approach attractive even for systems where the interaction is limited, e.g., due to stray capacitances in the setup. For a measurement of the square displacement, a similar advantage was identified in Ref. [48].

We first study an *RLC* circuit with one capacitor plate being an oscillating membrane, without assuming the symmetry discussed above [Fig. 2.1(b)]. The mechanical motion of the plate shifts the resonance frequency of the circuit, while the electric potential exerts a force on the membrane. In order to perform a QND measurement of the phonon number, we require this interaction to be proportional to $\hat{n}_\mathrm{b}$. We therefore Taylor expand the inverse of the capacitance to second order in the

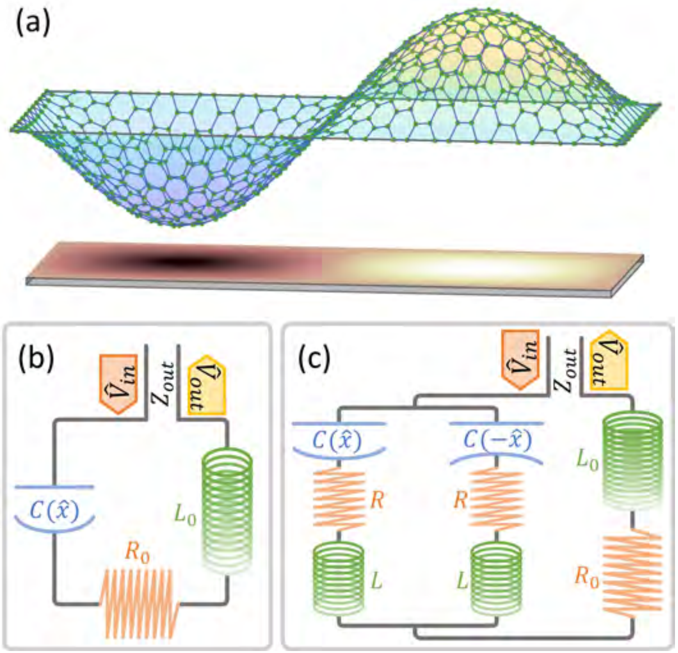

FIGURE 2.1: **(a)** Sketch of a capacitor with an oscillating plate, here represented by a graphene membrane [top]. We consider an antisymmetric $(2, 1)$ mechanical mode. **(b)** RLC oscillator formed by the inductance L_0, resistance R_0, and position–dependent capacitance $C(\hat{x})$. The circuit is driven by the input voltage $\hat{V}_{\text{in}}$ through a transmission line of impedance Z_{out}. $\hat{V}_{\text{out}}$ is the reflected signal. **(c)** Model circuit for an RLC system where the capacitor has the same form as in **(a)**. The membrane has a vanishing linear coupling to the symmetric electrical mode used for probing the system. The antisymmetric mode, residing in the small loop containing parasitic inductances L and resistances R, describes the redistribution of charge on the capacitor.

displacement, $1/C(\hat{x}) \simeq C_0^{-1} + \tilde{g}_1(\hat{b} + \hat{b}^\dagger) + \tilde{g}_2(\hat{b} + \hat{b}^\dagger)^2/2$, where we replaced the position $\hat{x}$ with the creation $\hat{b}^\dagger$ and annihilation $\hat{b}$ operators of the mechanical motion, and $\tilde{g}_{1,2}$ denote linear and quadratic coupling constants. Within the rotating wave approximation, $\tilde{g}_2(\hat{b} + \hat{b}^\dagger)^2/2 \simeq \tilde{g}_2\hat{n}_\text{b}$, leading to the desired QND interaction, while the $\tilde{g}_1$ term adds unwanted heating that spoils the phonon measurement.

The main aim of this work is to identify conditions under which the QND measurement is feasible, despite the presence of heating. We first consider the simple circuit in Fig. 2.1(b), and assume the incoming signal $\hat{V}_{\text{in}}$ to be in a coherent state resonant with the circuit. The quadratic interaction then shifts the electrical resonance frequency proportionally to the phonon number $\tilde{g}_2\hat{n}_\text{b}$. For small $\tilde{g}_2$, this shift leads to a phase change of the outgoing signal $\hat{V}_{\text{out}}$, that can be determined by homodyne measurement. Different phononic states will thus lead to distinct outcomes V_M, as shown in Fig. 2.2. The distance d between output signals for different $\hat{n}_\text{b}$ and the standard deviation σ of the noise define the signal to noise ratio $D = d/\sigma$ (see Fig. 2.2), that needs to be maximised.

In order to have a successful QND measurement, the phonon number $\hat{n}_\text{b}$ must be conserved. If the mechanical state jumps during a measurement, the outcome V_M will end up in between the desired peaks. This leads to a reduced contrast, as illustrated by the distribution in the background of Fig 2.2. The probability for $\hat{n}_\mathrm{b}$ to change is generally state–dependent, in the sense that higher Fock states are more likely to jump. A state–independent characterization of this heating, is given by the average phonons Δn_b added to the ground state during the measurement time T. The jump probability for any state can then be derived from Δn_b using standard results for harmonic oscillators (see section 2.2.3).

Both D and Δn_b are proportional to the incoming intensity. We therefore characterize a setup by the parameter $\lambda = D^2/\Delta n_\mathrm{b}$, where $\lambda \gg 1$ is required for successful QND detection. For the RLC circuit in Fig. 2.1(b) we find below that

$$\lambda = \frac{1}{2(1+2\bar{n}_\mathrm{e})^2}\left(\frac{g_2}{g_1}\right)^2\left(\frac{\omega_\mathrm{m}}{\gamma_\mathrm{t}}\right)^2, \tag{2.1}$$

where $g_1 = \tilde{g}_1 C_0 \omega_\mathrm{s}$, $g_2 = \tilde{g}_2 C_0 \omega_\mathrm{s}$ and $\bar{n}_\mathrm{e}$ is the thermal occupation of R_0 and Z_out (assumed equal, $R_0 = Z_\mathrm{out}$). Here, ω_m and $\omega_\mathrm{s} = (C_0 L_0)^{-1/2} \gg \omega_\mathrm{m}$ are the mechanical and electrical frequencies, respectively, and $\gamma_\mathrm{t} = Z_\mathrm{out}/L_0$ corresponds to the output coupling rate. A result similar to Eq. (2.1) is derived in Ref. [80].

Despite progress in reaching the resolved sideband regime $\omega_\mathrm{m} \gg \gamma_\mathrm{t}$ in both opto– and electromechanical systems, g_2 is generally much smaller than g_1, implying $\lambda \ll 1$ in Eq. (2.1). To circumvent this problem, we use the second fundamental mode of the membrane in the capacitor, as depicted in Fig. 2.1(a). The first order coefficient $\tilde{g}_1$ of the $1/C(\hat{x})$ expansion then vanishes, leaving $\tilde{g}_2$ to be the largest contribution to the electromechanical coupling. In this situation λ seemingly grows indefinitely, the induced heating disappears, and the QND measurement of the phonon number is easily realized. In practice, however, two effects will limit the achievable value of λ. First, inaccuracies in the nanofabrication can cause misalignments and, consequently, a residual linear coupling. Second, the oscillation of the membrane induces a charge redistribution in the capacitor to maintain it at an equipotential. The associated antisymmetric electrical mode introduces an effective linear coupling, and a similar heating mechanism as the one identified in Ref. [78] for the optomechanical setup of Refs. [45, 46]. In these papers, the quadratic interaction results from a hybridization of two modes linearly coupled to the mechanical position, and the QND detection was found to be impossible unless the single–photon coupling g_1 exceeded the intrinsic cavity damping. In our case, the QND interaction arises directly from the Taylor expansion of the capacitance. Hence, there is no constraint tying the second–order coupling g_2 to the properties of the symmetric and antisymmetric electrical modes, which can have vastly different resonance frequencies and dampings (see section 2.2.2). This inhibits the mechanical heating and ultimately allows for the QND detection of the phonon number. We model the charge redistribution in the capacitor by parasitic inductances (L) and resistances (R) in the equivalent circuit of Fig. 2.1(c). Each of the two arms containing R and L represents one half of the capacitor, with opposite dependence on the membrane position, $C(\hat{x})$ and $C(-\hat{x})$.

2.1.1 'Single-arm' RLC circuit

In the following, we derive Eq. (2.1) for the RLC circuit in Fig. 2.1(b). The methods sketched here will then be generalised for the 'double-arm' circuit in Fig. 2.1(c). Using the standard approach [81], we write the circuit Hamiltonian as $\hat{\mathcal{H}}(\hat{x}) = \hat{\Phi}^2/\left[2L_0\right] + \hat{Q}^2/\left[2C(\hat{x})\right]$, where the conjugate variables $\hat{Q}$ and $\hat{\Phi}$ are the charge and magnetic flux, respectively. We can expand $\hat{\mathcal{H}}(\hat{x})$ in the mechanical position $\hat{x} \propto$

$\hat{b} + \hat{b}^\dagger$, in order to obtain the circuit Hamiltonian $\hat{\mathcal{H}}_\mathrm{e} = \hat{\mathcal{H}}(\hat{x} = 0)$ and the coupling Hamiltonian $\hat{\mathcal{H}}_\mathrm{em} = g_1\omega_\mathrm{s}L_0\hat{Q}^2(\hat{b} + \hat{b}^\dagger)/2 + g_2\omega_\mathrm{s}L_0\hat{Q}^2(\hat{n}_\mathrm{b} + \hat{b}\hat{b}/2 + \hat{b}^\dagger\hat{b}^\dagger/2)$. The total Hamiltonian $\hat{\mathcal{H}}_\mathrm{tot} = \hat{\mathcal{H}}_\mathrm{e} + \hat{\mathcal{H}}_\mathrm{em} + \hat{\mathcal{H}}_\mathrm{m}$ is therefore the sum of the circuit, interaction, and the mechanical Hamiltonian $\hat{\mathcal{H}}_\mathrm{m} = \hbar\omega_\mathrm{m}\hat{b}^\dagger\hat{b}$.

Next, we describe the environmental effects corresponding to decay and heating of the modes. Associating each resistor R_i with its own Johnson–Nyquist noise $\hat{V}_{Ri}$, we find the equations of motion of the composite system

$$\dot{\hat{Q}} = \frac{\hat{\Phi}}{L_0} \tag{2.2a}$$

$$\begin{aligned}\dot{\hat{\Phi}} = &-\frac{\hat{Q}}{C_0} - (\gamma_\mathrm{t} + \gamma_\mathrm{r})\hat{\Phi} - g_1\omega_\mathrm{s}L_0\hat{Q}\left(\hat{b} + \hat{b}^\dagger\right) \\ &- g_2\omega_\mathrm{s}L_0\hat{Q}\left(\hat{n}_\mathrm{b} + \frac{\hat{b}\hat{b} + \hat{b}^\dagger\hat{b}^\dagger}{2}\right) + 2\left(\hat{V}_\mathrm{in} + \hat{V}_\mathrm{R0}\right)\end{aligned} \tag{2.2b}$$

$$\begin{aligned}\dot{\hat{b}} = &-i\omega_\mathrm{m}\hat{b} - g_1\frac{i\omega_\mathrm{s}L_0\hat{Q}^2}{2\hbar} - g_2\frac{i\omega_\mathrm{s}L_0\hat{Q}^2}{2\hbar}\left(\hat{b} + \hat{b}^\dagger\right) \\ &- \frac{\gamma_\mathrm{b}}{2}\hat{b} + i\frac{x_\mathrm{z}}{\hbar}\hat{F}_\mathrm{b},\end{aligned} \tag{2.2c}$$

where $\gamma_\mathrm{r} = R_0/L_0$, γ_b is the intrinsic mechanical damping rate with associated noise $\hat{F}_\mathrm{b}$, and $x_\mathrm{z} = \sqrt{\hbar/(2m\omega_\mathrm{m})}$ is the amplitude of the zero–point motion for a membrane of mass m. From now on, we consider optimally loaded setups with $\gamma_\mathrm{r} = \gamma_\mathrm{t}$. Eqs. (2.2) fully characterize the dynamics of the system, and represent the starting point for our detailed analysis.

The feedback of the membrane's motion on the electrical circuit is described by Eq. (2.2b). Driving the system at the electrical resonance frequency ω_s, the terms proportional to $g_1(\hat{b} + \hat{b}^\dagger)$ and $g_2(\hat{b}\hat{b} + \hat{b}^\dagger\hat{b}^\dagger)$ give rise to sidebands at frequencies $\omega_\mathrm{s} \pm \omega_\mathrm{m}$ and $\omega_\mathrm{s} \pm 2\omega_\mathrm{m}$, respectively, whereas $g_2\hat{n}_\mathrm{b}$ induces a phonon–dependent frequency shift of the microwave cavity. Since homodyne detection is only sensitive to signals at the measured frequency, the sidebands are removed in the outcome V_M, which is defined as the phase quadrature of $\hat{V}_\mathrm{out} = \hat{V}_\mathrm{in} - \gamma_\mathrm{t}\hat{\Phi}$. This allows us to neglect oscillating terms in the calculation of V_M[1]. The only contribution to V_M is therefore the phonon–dependent frequency shift, that allows us to resolve the mechanical state. On the contrary, the electrically induced mechanical heating only involves the sidebands $\omega_\mathrm{s} \pm \omega_\mathrm{m}$ and $\omega_\mathrm{s} \pm 2\omega_\mathrm{m}$, being unaffected by the term $g_2\hat{n}_\mathrm{b}$ in the Hamiltonian. For the RLC circuit in Fig. 2.1(b), the heating is dominated by the linear term, since $g_1 \gg g_2$, and we shall neglect g_2 for the calculation of Δn_b below.

Below, we quantify the heating of the membrane and the phonon–dependent LC–frequency shift. We first assume that the mechanical state does not jump during the measurement. Then, the equations of motion of the two subsystems decouple and we find

$$D^2 = g_2^2|\alpha|^2/[4(1+2\bar{n}_\mathrm{e})\gamma_\mathrm{t}^2], \tag{2.3}$$

where the number of photons $|\alpha|^2$ sent into the circuit within the measurement time T sets the measurement strength. As discussed above, Δn_b is the average phonon number at the end of the measurement $\Delta n_\mathrm{b} = \langle\hat{n}_\mathrm{b}(T)\rangle$, with the mechanics initially in its ground state. For T much shorter than the mechanical lifetime γ_b^{-1}, Δn_b can be linearised to find the rate at which the membrane heats up. For the RLC circuit in

---

[1] The linear term also leads to mechanically induced damping of the electrical circuit, but this is typically negligible compared to γ_t.

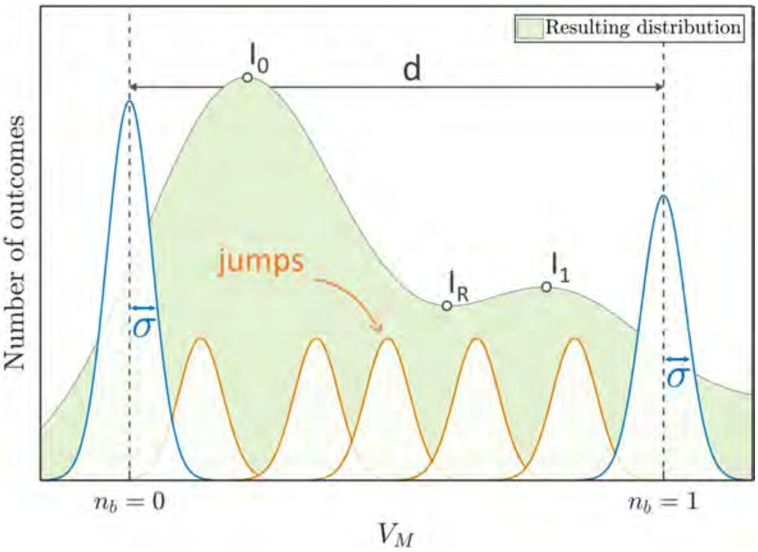

FIGURE 2.2: Distribution of outcomes V_{M} for two different phonon numbers: $n_{\mathrm{b}} = 0$ (first peak to the left) and $n_{\mathrm{b}} = 1$ (last peak to the right). For a given value of n_{b}, repeated measurements are Gaussian distributed with a variance $\sigma^2 \propto 1 + 2\bar{n}_{\mathrm{e}}$ of the outgoing signal $\hat{V}_{\mathrm{out}}$, consisting of vacuum and thermal noise. The distance d between the two peaks depends on the circuit parameters and the number of incident photons, and identifies the signal to noise ratio $D = d/\sigma$. Ideally, for each shot of the measurement, the mechanics is either in its ground or first excited state. However, for $\Delta n_{\mathrm{b}} > 0$ there will be events where the mechanical state jumps, resulting in outcomes V_{M} in between the peaks relative to $n_{\mathrm{b}} = 0$ and $n_{\mathrm{b}} = 1$ (smaller peaks in the figure). This leads to the smeared distribution shown in the back. The visibility of the QND measurement is quantified by the values at the peaks and valleys, as indicated by I_0, I_1 and I_R [see Eq. (2.8)]. The figure is for illustration only, and is not to scale.

Fig. 2.1(b), we find

$$\Delta n_{\mathrm{b}} = (1 + 2\bar{n}_{\mathrm{e}}) g_1^2 |\alpha|^2 / (2\omega_{\mathrm{m}}^2). \tag{2.4}$$

The parameter λ given in Eq. (2.1) is then found as the ratio $\lambda = D^2/\Delta n_{\mathrm{b}}$. For details, see section 2.2.1.

2.1.2 'Double arm' circuit

With the overall linear coupling vanishing, the parameter λ will be limited by fabrication imperfections and coupling to the antisymmetric mode. To model these phenomena we consider the circuit in Fig. 2.1(c), where the antisymmetric mode resides inside the small loop containing the two capacitors, and the symmetric one probes the system. We derive g_1 and g_2 from the expansion of *each* of the two capacitors: $1/C\,(\pm\hat{x}) \simeq C_0^{-1} \pm \tilde{g}_1(\hat{b} + \hat{b}^\dagger) + \tilde{g}_2 \hat{n}_{\mathrm{b}}$, so that in the absence of fabrication imperfections the *total* capacitor $C_{\mathrm{tot}} = C\,(\hat{x}) + C\,(-\hat{x})$ is not linearly coupled to the symmetric mode. The coefficients g_1 and g_2 are related to their tilde counterparts in the same way as before, and the parameters D^2 and Δn_{b} are evaluated in a similar fashion as we did for the *RLC* circuit. Since we quantify two sources of heating, it is convenient to write $\lambda = (\lambda_{\mathrm{b}}^{-1} + \lambda_{\mathrm{p}}^{-1})^{-1}$, where λ_{b} takes into account heating from charge redistribution, and λ_p describes the influence of fabrication imperfections[2]. With the details presented in section 2.2.2, we find

$$\lambda_b = \frac{2}{(1+2\bar{n}_e)^2}\left(\frac{g_2}{g_1}\right)^2\left(\frac{\omega_s}{\gamma_t}\right)^2\frac{Z_{out}}{R}, \tag{2.5a}$$

$$\lambda_p = \frac{2}{(1+2\bar{n}_e)^2}\left(\frac{g_2}{g_1}\right)^2\left(\frac{g_1}{g_r}\right)^2\left(\frac{\omega_m}{\gamma_t}\right)^2, \tag{2.5b}$$

where $\omega_s = [C_0(L+2L_0)]^{-1/2}$ is the frequency of the symmetric mode, $\gamma_t = [2Z_{out}]/[L+2L_0]$ is the decay to the transmission line and $g_r = 2C_0 x_z \omega_s \partial_x C_{tot}^{-1}(x)$ is the residual linear coupling induced by fabrication imperfection. We use the same notation introduced for the *RLC* circuit to allow a direct comparison. Eqs. (2.5) express the gain of our approach to QND detection. First, Eq. (2.5b) quantifies the advantage of symmetry: λ dramatically improves compared to Eq. (2.1) by having a small residual linear coupling $g_r \ll g_1$. Second, Eq. (2.5a) is multiplied by the factor $(\omega_s/\omega_m)^2$ with respect to Eq. (2.1). For microwave readout of a MHz oscillator, this factor can be substantial. Furthermore, the mechnical oscillator is now only susceptible to the noise associated with charge redistribution on the capacitor, and not to the resistance in the inductor. This gives an additional improvement if $R < Z_{out}$.

To describe a realistic situation, we numerically simulate the case in which the parasitic resistances R, inductances L and the two bare capacitances C_0 differ from each other. In Fig. 2.3, we test the system with these asymmetries and the physical parameters given below. In the left plot, the role of a residual linear coupling g_r is investigated. In the right one, we consider unbalanced resistances $R \pm \delta R$, inductances $L \pm \delta L$, and capacitances $C_0 \pm \delta C$. The results show that our analytical predictions accurately describe a system with non-zero g_r and δC. Furthermore, the numerical points confirm that δR and δL enter as higher order perturbations. In fact, we generally find that Eqs. (2.5) are accurate for relatively large perturbations (up to 25%).

Inspired by recent experiments [82, 83, 84, 85, 21], we estimate the value of λ, which can be reached in state–of–the–art setups. We consider a rectangular monolayer graphene membrane of length 1 μm and width 0.3 μm, with a mechanical frequency of $\omega_m = (2\pi)80$ MHz and a quality factor $Q = 10^6$. It is suspended $d_0 = 10$ nm above a conducting plate, forming the capacitor [see sketch in Fig. 2.1(a)]. Assuming that the membrane is clamped to the substrate along its boundaries, we identify the ratio of the coupling coefficients for each capacitor $C(\pm\hat{x})$ in Fig. 2.1(c) to be $g_2/g_1 = \pi^2 x_z/(8d_0)$ [86]. Considering that for these geometries stray capacitances C_s are typically preponderant with respect to C_0, we take $g_1 \simeq (2\pi)7$ kHz and $g_2 \simeq (2\pi)1$ Hz, corresponding to $C_s \simeq 100C_0$. For comparison, a value of $C_s = 50\ f$F is obtained in Ref. [82], for a graphene membrane about two and a half times the size considered here. This stray capacitance would be 376 times $C_0 \simeq 13\ f$F. Assuming a reduction of C_s due to the smaller dimensions, we take $C_s = 100C_0$.

With an electrical reservoir at zero temperature $\bar{n}_e \simeq 0$ (valid for milliKelvin experiments), an electrical frequency $\omega_s = (2\pi)7$ GHz, and decay rate $\gamma_t = (2\pi)150$ kHz, we get $\lambda_b = 105 \times Z_{out}/R$ and $\lambda_p = 0.014 \times (g_1/g_r)^2$. Since the graphene coupling can be tuned via electric fields [87, 88, 89], we assume $g_1/g_r \sim 100$, which fixes λ between 60 ($R = Z_{out}$) and 122 ($R = Z_{out}/10$), mostly restricted by λ_p. This limit is well above the threshold for having a good visibility of the phonon number states

---

[2] The simple analytical expressions for λ_p given in the text is valid for the parasitic elements of the circuit being larger than the non-parasitic ones.

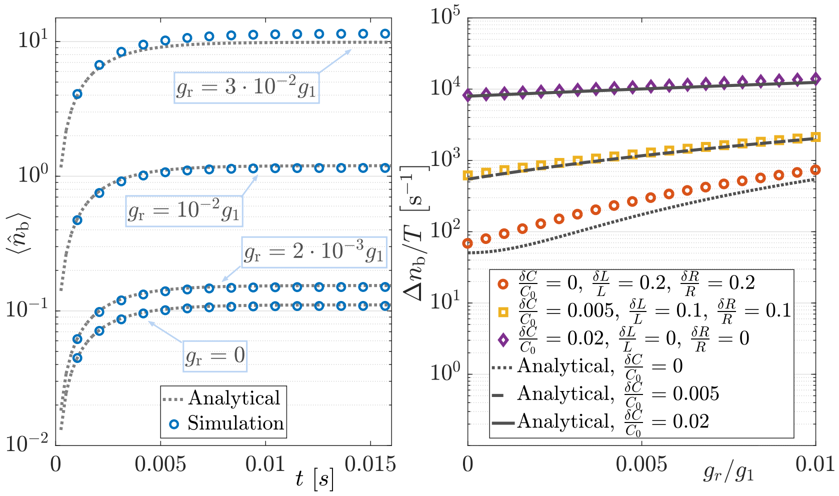

FIGURE 2.3: **Left**: Average phonon number $n_\mathrm{b}(t)$ as a function of time. We present a comparison between the analytical curves (grey, dotted lines) and the full simulations of the system (blue dots). From the bottom to the top we set g_r/g_1 to be 0, $2\cdot 10^{-3}$, 10^{-2} and $3\cdot 10^{-2}$. We use $\delta R = \delta L = \delta C = 0$. **Right**: heating rate $\Delta n_\mathrm{b}/T$ as a function of the normalised residual linear coupling g_r/g_1. Here we analyse the system in presence of asymmetries in the parasitic elements of the circuit. The three dark grey lines are the analytical predictions for $\delta C/C_0$ being equal to 0 (dotted), 0.005 (dashed) and 0.02 (full). The circles, squares and diamonds are the simulated results for the values $\delta R/R$, $\delta L/L$, and $\delta C/C$ reported in the legend. We assume $L/L_0 = 10^{-2}$, $R/Z_\mathrm{out} = 10^{-1}$, $\omega_\mathrm{s} = (2\pi)7$ GHz, $\omega_\mathrm{m} = (2\pi)80$ MHz, $\gamma_\mathrm{r} \simeq \gamma_\mathrm{t} = (2\pi)0.15$ MHz, $\gamma_\mathrm{b} = (2\pi)80$ Hz, $g_1 = (2\pi)7$ kHz, $\bar{n}_\mathrm{e} = \bar{n}_\mathrm{m} = 0$, and an incident photon flux $|\tilde{\alpha}|^2 = 1.15\cdot 10^{15}\ \mathrm{s}^{-1}$.

(see below), and can be further improved by either increasing the sideband resolution $\omega_\mathrm{m}/\gamma_\mathrm{t}$, the electrical frequency ω_s, or by reducing the size of the membrane. In Fig. 2.4(b), we show the linear coupling g_1 as a function of the stray capacitance. For small values of C_s, we reach the strong coupling regime, where $g_1 \geq \gamma_\mathrm{t}$. In the realistic scenario described above, where $C_\mathrm{s} \gg C_0$, our scheme still allows for phonon QND measurement even for $g_1, g_2 \ll \gamma_\mathrm{t}$. This is in contrast to the optomechanical regime, where strong coupling $g_1 > \gamma_\mathrm{t}$ is required [78]. Regardless of how much C_s reduces the coupling constants, it is in principle always possible to compensate by using stronger power.

2.1.3 Measurement

We now evaluate how well a given value of λ allows for the QND detection of the phonon number. To this end we consider a situation where the system is continuosly probed and measured. The output is then turned into discrete results by averaging over a suitable time T, and a histogram is constructed from the measured values V_M. We assume that the heating of the continuous QND probing is in equilibrium with the mechanical damping and the associated reservoir. In this case, one also needs to consider the thermal bath of the membrane. In addition to Δn_b determined above, the total heating out of the ground state is thus $\Delta n_\mathrm{b} + \gamma_\mathrm{b}\bar{n}_\mathrm{m}T$. This additional term

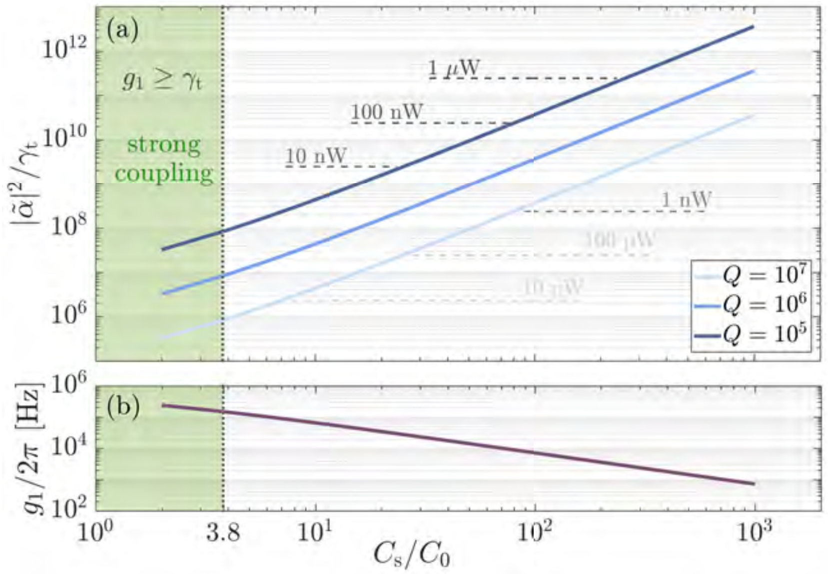

FIGURE 2.4: **(a)**: average intracavity photons $|\tilde{\alpha}|^2/\gamma_t$ required for the QND measurement, as a function of the relative value of the stray capacitance C_s/C_0. The three lines correspond to different values of the mechanical quality factor, as indicated in the legend. We assume $\Delta n_b = 0.3$ and equal contributions from the mechanical and electrically induced reservoirs $\bar{n}_m = \bar{N}_{\text{eff}}/2 = 3$. As a reference, the grey dashed lines indicate the associated powers of the probe. **(b)**: linear coupling g_1 as a function of C_s/C_0. For both figures, the shadowed region indicates the strong coupling $g_1 \geq \gamma_t$, where QND detection is feasible with other approaches [45, 48, 49].

leads to a redefinition of the parameter λ to

$$\lambda' = \lambda \frac{\Delta n_b}{\Delta n_b + \gamma_b \bar{n}_m T}, \tag{2.6}$$

and the equilibrium average mechanical occupation, resulting from both the mechanical reservoir and the QND probe, becomes

$$\bar{N}_{\text{eff}} \simeq \bar{n}_m \frac{\lambda}{\lambda - \lambda'}. \tag{2.7}$$

The phonon QND measurement is then characterized by λ', which is desirable to have as close as possible to its maximum λ. This can be achieved by choosing a sufficiently strong probing power and a short measurement time T, such that the mechanical heating can be neglected. This leads to a large $\bar{N}_{\text{eff}}$, that does not significantly change the contrast of the QND measurement [see Eq. (2.9) and Fig. 2.5(b)], but increases the time for acquiring significant statistics (the mechanical system spends less time in each Fock state).

Given λ', we now want to optimize all remaining parameters of the system, to be able to discern the ground and first excited states with the largest contrast. We simulate the mechanical system with the quantum–jump method, and pick Gaussian distributed random values for the electrical vacuum and thermal noise. From this, we make the histogram of the resulting output voltages V_M presented in Fig. 2.5(a), where the induced heating Δn_{b} is optimized numerically. For the optimization we consider the visibility

$$\xi = \frac{\frac{1}{2}\left(I_0 + I_1\right) - I_{\mathrm{R}}}{\frac{1}{2}\left(I_0 + I_1\right) + I_{\mathrm{R}}}, \tag{2.8}$$

where I_0 and I_1 are the heights of the peaks corresponding to $n_{\mathrm{b}} = 0$ and $n_{\mathrm{b}} = 1$ phonons, while I_{R} is the lowest height in between I_0 and I_1 (see Fig. 2.2).

Additionally, we make an analytical model where we allow for one jump during each measurement period. We can extract the asymptotic behaviour of the visibility

$$\xi\left(\lambda', \bar{N}_{\mathrm{eff}}\right) = 1 - 8\frac{3 + 5\bar{N}_{\mathrm{eff}}}{1 + 2\bar{N}_{\mathrm{eff}}}\frac{\sqrt{\pi \log \lambda'}}{\lambda'}, \tag{2.9}$$

reflecting the compromise between the contributions to I_{R} from the noise $\propto \exp(-D^2/8)$ and from the jumps during the measurements $\propto \Delta n_{\mathrm{b}}$.

The results of simulations and model are shown in Fig. 2.5(a). The blue points are the numerical optimization, which are in good agreement with the analytical result (red, dotted line). Notice that for small values of λ', the optimal Δn_{b} is sufficiently high to allow multiple jumps during the measurement time T, leading to minor discrepancies. The black, solid line is Eq. (2.9), and the shadowed region corresponds to the predicted values of λ for the parameters introduced above. Qualitatively, clear signatures of the mechanical energy quantization are present for $\lambda' \gtrsim 40$, where the visibility exceeds 20%.

For the experimental parameters considered above, the maximum attainable value of λ' is $\lambda = 122$ (for $R = Z_{\mathrm{out}}/10$), and is achieved with a strong probe such that $\bar{N}_{\mathrm{eff}} \gg \bar{n}_{\mathrm{m}}$. The incident power and the measurement time T provide a handle to optimize the performance for given experimental conditions. Qualitatively, a short value of T minimizes the effects of the mechanical heating, and makes $\lambda' \simeq \lambda$. On the other hand, the required power to reach such a regime can be troublesome [90], and we may need to integrate for too long time to have sufficient statistics (since $\bar{N}_{\mathrm{eff}} \gg 1$). This last problem can be solved by adding an electrical cooling, red–detuned by $\omega_{\mathrm{m}} \gg \gamma_{\mathrm{t}}$ from the QND probe. This cooling would not affect the parameter λ', since it does not heat up the system, but only reduces $\bar{N}_{\mathrm{eff}}$. The visibility ξ thus remains almost unaltered [see Eq. (2.9) and Fig. 2.5(b)], but the probability to find the membrane in low excited states is increased, reducing the experimental time.

As an example, assume that the heating from the electrical feedback and the mechanical bath are equal, such that $\lambda' = \lambda/2 = 61$. Considering a cryogenic temperature of 14 mK [84], the average mechanical occupation is $\bar{n}_{\mathrm{m}} \simeq 3$, implying $\bar{N}_{\mathrm{eff}} = 6$. The optimal Δn_{b} is then 0.3, and can be obtained with a driving power of 16 nW and a measurement time of 0.1 ms for a mechanical quality factor $Q = 10^6$ and a stray capacitance $C_{\mathrm{s}} = 100C_0$. For other values of Q and C_{s}, the driving power can be varied to fulfil the constraint $\bar{N}_{\mathrm{eff}} = 2\bar{n}_{\mathrm{m}}$, as shown in Fig. 2.4(a). The incident field is rather intense, which may cause additional heating to the system. In the setup of Ref. [90], such additional heating has been observed above an intracavity photon number of 10^8. For comparison, in Fig. 2.4(a) we show the intracavity photon number $|\tilde{\alpha}|^2/\gamma_{\mathrm{t}}$ for our system, where $|\tilde{\alpha}|^2 = |\alpha|^2/T$ is the photon flux. Depending on the parameters, we see that $|\tilde{\alpha}|^2/\gamma_{\mathrm{t}}$ will be similar or higher than 10^8 for $C_{\mathrm{s}} \gtrsim 100C_0$. These devices cannot, however, be compared directly. Nevertheless, since Ref. [90] indicates that the source of this heating is electrical, we believe that it would be strongly suppressed for the QND measurement considered here. Since the linear coupling

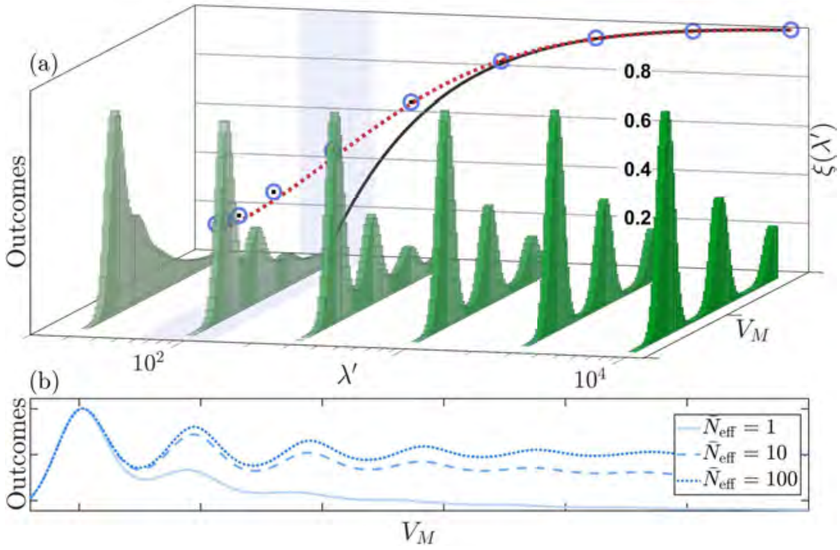

FIGURE 2.5: **(a), 3D plot**: histograms of outcomes for different λ' (from left to right, $\lambda' = 32$, 10^2, $3 \cdot 10^2$, 10^3, $3 \cdot 10^3$ and 10^4). The optimal values of Δn_{b} are (from left to right) 0.43, 0.27, 0.12, 0.05, $2 \cdot 10^{-3}$ and $8 \cdot 10^{-4}$, and have been determined by a numerical optimization. The shadowed region corresponds to the estimated visibility for state–of–the–art technology, $\lambda \simeq 60 - 130$. **2D plot (back)**: maximum visibility ξ for different values of the parameter λ'. The blue circles have been evaluated numerically from the histograms in the 3D plot (and others). The error bars of the Monte Carlo simulation (black lines inside) have been determined assuming Poissonian statistics in each bin, and are negligible on this scale. The red dotted curve comes from our model for the visibility, and the black solid curve is the simplified expression presented in Eq. (2.9). We consider $\bar{N}_{\text{eff}} = 1$. See Methods for more details. **(b)**: expected outcomes for $\lambda' = 75$ and $\bar{N}_{\text{eff}}$ being 1 (full), 10 (dashed) and 100 (dotted line). The parameter Δn_{b} has been optimized to achieve maximum visibility for each value of $\bar{N}_{\text{eff}}$.

is almost cancelled by symmetry, the resulting heating rate is likely reduced by a factor $(g_{\text{r}}/g_1)^2 \simeq 10^{-4}$. In absence of this suppression, conducting our experiment in a pulsed regime may substantially reduce other heating mechanisms (see section 2.2.4).

2.2 Derivations

Here we provide additional details to support the above results. In subsection 2.2.1 we carefully study the *RLC* circuit. We describe how the QND interaction allows for reading out the mechanical state, and the dynamics induced by the linear coupling. In subsection 2.2.2, we derive the figure of merit λ for the circuit in Fig. 2.1(c). We consider both the symmetric case, for which analytical results are given, and the most general case of an antisymmetric system. In subsection 2.2.3 we look at a possible measurement scheme, both analytically and numerically. Finally, in subsection 2.2.4, we present an investigation of the required experimental parameters for a concrete realization of our setup. Throughout, we present several numerical simulations to support our analytical results.

2.2.1 RLC circuit

We consider an *RLC* circuit where the capacitor contains an oscillating element. Following the standard procedure for quantizing an electrical circuit [81], we can write the Hamiltonian of the setup presented in Fig. 2.6 as

$$\begin{aligned}\hat{\mathcal{H}} =& \hbar\omega_{\rm m}\hat{b}^\dagger\hat{b} + \frac{\hat{\Phi}^2}{2L_0} + \frac{\hat{Q}^2}{2C_0} + \frac{g_1\omega_{\rm s}L_0}{2}\hat{Q}^2(\hat{b}+\hat{b}^\dagger) \\ &+ \frac{g_2\omega_{\rm s}L_0}{2}\hat{Q}^2\left(\hat{b}^\dagger\hat{b} + \frac{\hat{b}\hat{b}+\hat{b}^\dagger\hat{b}^\dagger}{2}\right) - 2\hat{Q}(\hat{V}_{\rm in}+\hat{V}_{\rm R0}) - x_{\rm z}\hat{F}_{\rm b}(\hat{b}+\hat{b}^\dagger),\end{aligned} \tag{2.10}$$

where the conjugate position $\hat{Q}$ and momentum $\hat{\Phi} = L_0\hat{I}$ are the electrical charge and flux, respectively. $x_{\rm z} = \sqrt{\hbar/(2m\omega_{\rm m})}$ is the zero–point motion amplitude for a membrane of mass m, and $\hat{b}$ ($\hat{b}^\dagger$) denotes the mechanical annihilation (creation) operator. $\omega_{\rm m}$ and $\omega_{\rm s} = (C_0L_0)^{-\frac{1}{2}}$ are the mechanical and electrical resonance frequencies. C_0, g_1 and g_2 are derived from the expansion of the inverse capacitance,

$$C^{-1}(\hat{b}+\hat{b}^\dagger) \simeq C_0^{-1} + g_1L_0\omega_{\rm s}(\hat{b}+\hat{b}^\dagger) + g_2L_0\omega_{\rm s}\left(\hat{b}+\hat{b}^\dagger\right)^2, \tag{2.11}$$

where the coupling required for the QND interaction comes from the rotating wave approximation: $(\hat{b}+\hat{b}^\dagger)^2 \simeq 2\hat{n}_{\rm b}+1$. Finally, $\hat{V}_{\rm in}$ is the input field, $\hat{V}_{\rm R0}$ is the Johnson–Nyquist noise associated with the resistor R_0, and $\hat{F}_{\rm b}$ is the random force related to the mechanical reservoir that slowly thermalizes the membrane. From Eq. (2.10) we can derive the Heisenberg equations of motion for the electromechanical system operators $\hat{Q}$, $\hat{\Phi}$ and $\hat{b}$. Adding decays and noises to the equations of motion we have

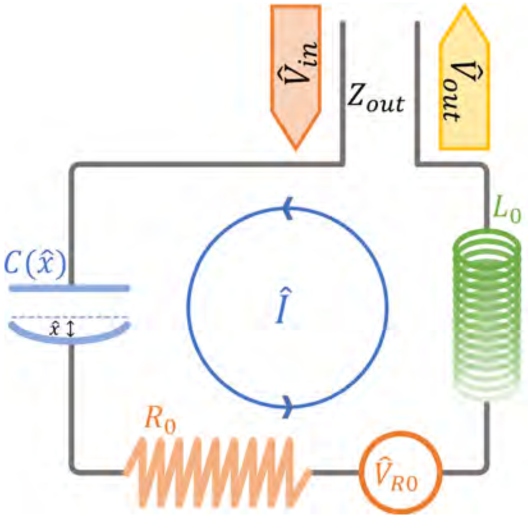

FIGURE 2.6: Circuit diagram for an RLC circuit coupled capacitively to a mechanical oscillator, with the position operator denoted as $\hat{x}$. R_0 and L_0 are the inductance and resistance of the electrical circuit, while $C(\hat{x})$ is the position–dependent capacitance. The setup is driven by the microwave (MW) field $\hat{V}_{\rm in}$ through the semi–infinite transmission line of impedance $Z_{\rm out}$. $\hat{V}_{\rm out}$ is the reflected signal, $\hat{V}_{\rm R0}$ the Johnson–Nyquist noise associated with R_0, and $\hat{I}$ is the current flowing in the circuit.

$$\dot{\hat{Q}} = \frac{\hat{\Phi}}{L_0}, \tag{2.12a}$$

$$\begin{aligned}\dot{\hat{\Phi}} = &- \frac{\hat{Q}}{C_0} - g_1\omega_s L_0 \hat{Q}\left(\hat{b}+\hat{b}^\dagger\right) - g_2\omega_s L_0\hat{Q}\left(\hat{n}_b + \frac{\hat{b}\hat{b}+\hat{b}^\dagger\hat{b}^\dagger}{2}\right) \\ &- (\gamma_t+\gamma_r)\hat{\Phi} + 2\left(\hat{V}_{in}+\hat{V}_{R0}\right),\end{aligned} \tag{2.12b}$$

$$\dot{\hat{b}} = - i\omega_m\hat{b} - g_1\frac{i\omega_s L_0\hat{Q}^2}{2\hbar} - g_2\frac{i\omega_s L_0\hat{Q}^2}{2\hbar}\left(\hat{b}+\hat{b}^\dagger\right) - \frac{\gamma_b}{2}\hat{b} + i\frac{x_z}{\hbar}\hat{F}_b. \tag{2.12c}$$

Importantly, these expressions are just the familiar Kirchoff's laws, which provide the form of the electrical decay rates $\gamma_r = R_0/L_0$ and $\gamma_t = Z_{out}/L_0$. The mechanical decay rate γ_b is an intrinsic property of the membrane, and we have assumed that the mechanical reservoir can be treated using the Markov approximation. Finally, the reflected signal is determined by the input/output relations

$$\hat{V}_{out} = \hat{V}_{in} - \gamma_t\hat{\Phi}, \tag{2.13}$$

that read the same in the time and frequency domains.

QND measurement of the phonon number

As explained in the section 2.1, there are three mechanisms with which the mechanical system influences the electrical one. These are the two terms $g_1(\hat{b}+\hat{b}^\dagger)$ and $g_2(\hat{b}\hat{b}+\hat{b}^\dagger\hat{b}^\dagger)$, which generate sidebands at frequencies $\omega_s \pm \omega_m$ and $\omega_s \pm 2\omega_m$, and a phonon–dependent frequency shift proportional to $g_2\hat{n}_b$ [see Eq. (2.12b)]. When we perform homodyne measurement at the resonant frequency of the electrical circuit ω_s, the sidebands contribution to the measurement outcome averages out, and we are left with the phonon–dependent frequency shift. The main detrimental effect of g_1 will be to cause heating. We consider this in subsection 2.2.1, and in the following discussion of the readout we thus assume that the phonon number is conserved, $\hat{n}_b(t) \to \hat{n}_b =$ constant. Under these assumptions, the electrical readout is independent of the mechanical dynamics, and can be described by

$$\dot{\hat{Q}} = \frac{\hat{\Phi}}{L_0}, \tag{2.14a}$$

$$\dot{\hat{\Phi}} = - \frac{\hat{Q}}{C_0} - g_2\omega_s L_0\hat{Q}\hat{n}_b - (\gamma_t+\gamma_r)\hat{\Phi} + 2\left(\hat{V}_{in}+\hat{V}_{R0}\right). \tag{2.14b}$$

As it is instructive to look at these equations in the frequency domain, we introduce the Fourier series of any operator $\hat{O}(t)$ by

$$\hat{O}(t) = \sum_{k=-\infty}^{\infty}\hat{O}[\Omega_k]\frac{e^{-i\Omega_k t}}{\sqrt{\tau}}, \tag{2.15}$$

with $\Omega_k = 2\pi k/\tau$ ($k \in \mathbb{Z}$) being the allowed frequencies, and τ is the time period used to define the Fourier series. For now we will let τ be equal to the measurement time T, but later we shall consider a larger value to describe heating on longer time scales. The Fourier coefficients $\hat{O}[\Omega_k]$ are then defined by

$$\hat{O}[\Omega_k] = \int_0^\tau \hat{O}(t)\frac{e^{i\Omega_k t}}{\sqrt{\tau}}dt. \tag{2.16}$$

It is possible to rewrite equations (2.14) in the frequency domain:

$$-i\Omega_k\hat{\Phi}[\Omega_k] = -\frac{\hat{Q}[\Omega_k]}{C_0} - g_2\omega_{\mathrm{s}}L_0\hat{Q}[\Omega_k]\hat{n}_{\mathrm{b}} - (\gamma_{\mathrm{r}}+\gamma_{\mathrm{t}})\hat{\Phi}[\Omega_k] + 2(\hat{V}_{\mathrm{in}}[\Omega_k] + \hat{V}_{\mathrm{R0}}[\Omega_k]), \tag{2.17a}$$

$$-i\Omega_k\hat{Q}[\Omega_k] = \frac{\hat{\Phi}[\Omega_k]}{L_0}. \tag{2.17b}$$

From these two relations we derive $\hat{\Phi}[\Omega_k]$, which can then be used in Eq. (2.13) for determining $\hat{V}_{\mathrm{out}}[\Omega_k]$:

$$\hat{V}_{\mathrm{out}}[\Omega_k] = [1-\zeta(\Omega_k,\hat{n}_{\mathrm{b}})]\,\hat{V}_{\mathrm{in}}[\Omega_k] - \zeta(\Omega_k,\hat{n}_{\mathrm{b}})\hat{V}_{\mathrm{R0}}[\Omega_k], \tag{2.18a}$$

$$\zeta(\Omega_k,\hat{n}_{\mathrm{b}}) = \frac{2\gamma_{\mathrm{t}}\Omega_k}{-i(\Omega_k^2-\omega_{\mathrm{s}}^2-g_2\omega_{\mathrm{s}}\hat{n}_{\mathrm{b}}) + \Omega_k(\gamma_{\mathrm{r}}+\gamma_{\mathrm{t}})}. \tag{2.18b}$$

These expressions describe the principle of the QND measurement: the quadratic interaction shifts the resonance frequency of the circuit by an amount proportional to $g_2 n_{\mathrm{b}}$ [denominator of Eq. (2.18b)]. By sending a signal resonant with the electrical circuit, it is possible to detect this frequency change as a phase shift of the reflected signal.

From the quantized form of $\hat{V}_{\mathrm{in}}[\Omega_k]$ and $\hat{V}_{\mathrm{R0}}[\Omega_k]$ [77], we have the Fourier components

$$\hat{V}_{\mathrm{in}}[\Omega_k] = \sqrt{\frac{\hbar\Omega_k Z_{\mathrm{out}}}{2}}\hat{a}_{\mathrm{in},k}, \tag{2.19a}$$

$$\hat{V}_{\mathrm{R0}}[\Omega_k] = \sqrt{\frac{\hbar\Omega_k R_0}{2}}\hat{a}_{\mathrm{R0},k}, \tag{2.19b}$$

where $\hat{a}_{\mathrm{in},k}$ and $\hat{a}_{\mathrm{R0},k}$ are the annihilation operators for the input field and the electrical reservoir, and satisfy the standard commutation relations. The measurement outcome $\hat{V}_{\mathrm{M}}$ is obtained by homodyne detection, meaning that we have access to

$$\hat{V}_{\mathrm{M}}[\Omega_k] = \frac{e^{i\frac{\theta}{2}}\hat{V}_{\mathrm{out}}[\Omega_k] + e^{-i\frac{\theta}{2}}\hat{V}^{\dagger}_{\mathrm{out}}[\Omega_k]}{2}, \tag{2.20}$$

where θ is an arbitrary phase that allows choosing the quadrature of the reflected signal to be measured.

Having now all the operator equations describing the system in the Heisenberg formalism, we need to define the input state $\hat{\rho}_{\mathrm{in}}$. Assuming that the semi–infinite transmission line of impedance Z_{out} and the resistor R_0 are connected to reservoirs at the same temperature T_{e}, and that we drive the circuit with a coherent field at the resonant frequency ω_{s}, we have:

$$\hat{\rho}_{\mathrm{in}}(\tilde{\alpha},\beta_{\mathrm{R}}) = \frac{1}{\mathbf{Z}}\hat{D}(\tilde{\alpha})e^{-\beta_{\mathrm{R}}\hat{\mathcal{H}}_{\mathrm{R}}}\hat{D}^{\dagger}(\tilde{\alpha}). \tag{2.21}$$

Here, $\mathbf{Z} = \mathrm{Tr}\left\{e^{-\beta_{\mathrm{R}}\hat{\mathcal{H}}_{\mathrm{R}}}\right\}$ is the partition function, $\hat{D}(\tilde{\alpha}) = \exp\big(\int_0^T \tilde{\alpha}(t)\hat{a}^{\dagger}_{\mathrm{in},s}(t) - \tilde{\alpha}^*(t)\hat{a}_{\mathrm{in},s}(t)dt\big)$ is the displacement operator, $|\tilde{\alpha}|^2$ is the photon flux, $\hat{\mathcal{H}}_{\mathrm{R}} = \sum_k \{\hbar\Omega_k\hat{a}^{\dagger}_{\mathrm{in},k}\hat{a}_{\mathrm{in},k} + \hbar\Omega_k\hat{a}^{\dagger}_{\mathrm{R0},k}\hat{a}_{\mathrm{R0},k}\}$ is the reservoir Hamiltonian, and $\beta_{\mathrm{R}}^{-1} = k_{\mathrm{B}}T_{\mathrm{e}}$ with k_{B} being the Boltzmann constant. Using $\hat{\rho}_{\mathrm{in}}(\tilde{\alpha},\beta_{\mathrm{R}})$ it is possible to calculate the average measured signal $V_{\mathrm{M}} = \langle\hat{V}_{\mathrm{M}}\rangle$ and the variance $(\Delta\hat{V}_{\mathrm{M}})^2 = \langle\hat{V}_{\mathrm{M}}^2\rangle - \langle\hat{V}_{\mathrm{M}}\rangle^2$ for an incident field at the resonance frequency ω_s:

$$V_\mathrm{M}(n_\mathrm{b}) = -\alpha\sqrt{\frac{\hbar\omega_\mathrm{s}Z_\mathrm{out}}{2}}\mathrm{Im}\{\zeta(\omega_\mathrm{s}, n_\mathrm{b})\}, \tag{2.22a}$$

$$(\Delta\hat{V}_\mathrm{M})^2 = \frac{\hbar\omega_\mathrm{s}Z_\mathrm{out}}{2}\left[1 + 2\bar{n}_\mathrm{e}(\omega_\mathrm{s}, T_\mathrm{e})\right], \tag{2.22b}$$

where $|\alpha|^2 = \int_0^T |\tilde{\alpha}(t)|^2 dt$ is the number of photons sent into the circuit during the measurement. The imaginary part is denoted with $\mathrm{Im}\{\cdot\}$, and $\bar{n}_\mathrm{e}(\omega_\mathrm{s}, T_\mathrm{e}) = [\exp(\hbar\beta_\mathrm{R}\omega_\mathrm{s}) - 1]^{-1}$ is the average number of photons at frequency ω_s in the electrical reservoir. Note that we have taken $\theta = \pi$ in Eq. (2.20), and $\tilde{\alpha}(t) = \alpha/\sqrt{T}$ to be purely real. With this choice, we measure the phase quadrature, which optimizes the signal for small g_2 (see Fig. 2.7).

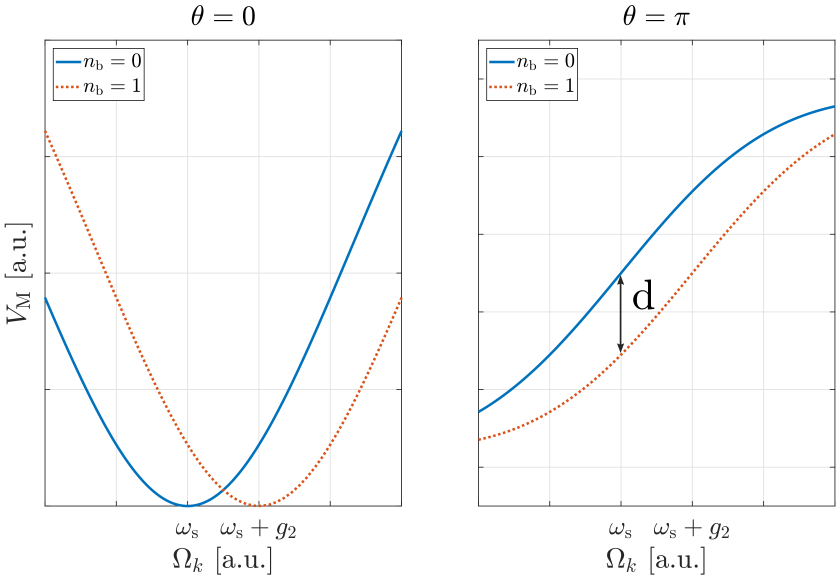

FIGURE 2.7: Example of amplitude **(left)** and phase **(right)** quadratures of the measured operator $\hat{V}_\mathrm{M}$. The plain and dotted curves refer, respectively, to the cases in which the membrane is in its ground ($n_\mathrm{b} = 0$) or in its first excited ($n_\mathrm{b} = 1$) state. As one can see, the quadratic coupling g_2 induces a frequency shift, proportional to the phonon number. The quantity d, derived analytically in Eq. (2.23), is indicated. We assumed optimally loaded setups with $\gamma_\mathrm{r} = \gamma_\mathrm{t}$. Compared to the realistic scenario $g_2 \ll \gamma_\mathrm{t}$, the frequency shift is here exaggerated. Whenever $g_2 \ll \gamma_\mathrm{t}$, the frequency shift is more easily detected by looking at the phase quadrature $\theta = \pi$ of the reflected signal.

It is now possible to derive the parameter $D^2 = d^2/\sigma^2$ introduced in section 2.1. We defined d to be the difference between two outcomes with one and zero phonons respectively,

$$d = V_\mathrm{M}(n_\mathrm{b} = 1) - V_\mathrm{M}(n_\mathrm{b} = 0) = \alpha\sqrt{\frac{\hbar\omega_\mathrm{s}Z_\mathrm{out}}{2}}\mathrm{Im}\{\zeta(\omega_\mathrm{s}, n_\mathrm{b} = 0) - \zeta(\omega_\mathrm{s}, n_\mathrm{b} = 1)\}. \tag{2.23}$$

Considering that σ^2 is the variance $(\Delta\hat{V}_{\rm M})^2$, we find

$$D^2 = \frac{d^2}{\sigma^2} = \frac{4}{1+2\bar{n}_{\rm e}} \frac{g_2^2|\alpha|^2\gamma_{\rm t}^2}{\left[g_2^2 + (\gamma_{\rm t}+\gamma_{\rm r})^2\right]^2}. \tag{2.24}$$

This last equation reduces to Eq. (2.3) by setting $\gamma_{\rm r} = \gamma_{\rm t}$ and noticing that typically $g_2 \ll \gamma_{\rm r} + \gamma_{\rm t}$.

Membrane heating

In this subsection we study the time evolution of the average phonon number $n_{\rm b}(t) = \langle \hat{n}_{\rm b}(t)\rangle$, and determine the parameter $\Delta n_{\rm b}$ that characterizes the probability for the mechanical state to jump during the measurement time T. It is convenient to introduce creation $\hat{a}^\dagger$ and annihilation $\hat{a}$ operators for the electrical charge $\hat{Q}$ and flux $\hat{\Phi}$ operators,

$$\hat{Q} = \sqrt{\frac{\hbar C_0\omega_{\rm s}}{2}}(\hat{a}+\hat{a}^\dagger), \tag{2.25a}$$

$$\hat{\Phi} = i\sqrt{\frac{\hbar}{2C_0\omega_{\rm s}}}(\hat{a}^\dagger - \hat{a}). \tag{2.25b}$$

Using these we can rewrite the Hamiltonian in Eq. (2.10) as

$$\begin{aligned}\hat{\mathcal{H}} =& \hbar\omega_{\rm s}\hat{a}^\dagger\hat{a} + \hbar\omega_{\rm m}\hat{b}^\dagger\hat{b} + \frac{\hbar g_1}{2}\hat{a}^\dagger\hat{a}(\hat{b}+\hat{b}^\dagger) + \frac{\hbar g_2}{2}\hat{a}^\dagger\hat{a}\left(\hat{b}^\dagger\hat{b} + \frac{\hat{b}\hat{b}+\hat{b}^\dagger\hat{b}^\dagger}{2}\right)\\ &- \hbar\sqrt{\frac{2C_0\omega_{\rm s}}{\hbar}}(\hat{a}+\hat{a}^\dagger)(\hat{V}_{\rm in}+\hat{V}_{\rm R0}) - x_{\rm z}\hat{F}_{\rm b}(\hat{b}+\hat{b}^\dagger),\end{aligned} \tag{2.26}$$

where we have used the rotating wave approximation to neglect terms which are off–resonant with the electrical frequency $\omega_{\rm s}$. Given that the coupling coefficients g_1 and g_2 are small compared to all other parameters, we linearize $\hat{a}$ and $\hat{a}^\dagger$ such that only deviations from their steady states are considered: $\hat{a}^{(\dagger)} = \langle\hat{a}^{(\dagger)}\rangle + \hat{\delta a}^{(\dagger)}$, where

$$\langle\hat{a}(t)\rangle \xrightarrow{\text{steady}} \frac{2i\alpha\sqrt{\gamma_{\rm t}}e^{-i\omega_{\rm s}t}}{\sqrt{T}(\gamma_{\rm t}+\gamma_{\rm r})}. \tag{2.27}$$

If the experiment is performed in a pulsed fashion with incoming pulses varying on a timescale comparable to the circuit's lifetime $(\gamma_{\rm r}+\gamma_{\rm t})^{-1}$, Eq. (2.27) should be replaced by a suitable expression that takes into account the transient dynamics [91]. Here we restrict ourselves to the cases in which either fields are applied continuously, or pulses are slowly varying on the timescale identified by $(\gamma_{\rm r}+\gamma_{\rm t})^{-1}$. In the latter case, the simple replacement $\alpha \to \alpha(t)$ in Eq. (2.27) is sufficient.

Considering that $g_2 \ll g_1$, we can neglect the quadratic coupling in the Hamiltonian Eq. (2.26) for calculating the heating. The Hamiltonian can then be rewritten in the form

$$\begin{aligned}\hat{\mathcal{H}} =& \hbar\omega_{\rm m}\hat{b}^\dagger\hat{b} + i\frac{\hbar g_1\alpha}{\gamma_{\rm t}+\gamma_{\rm r}}\sqrt{\frac{\gamma_{\rm t}}{T}}(\hat{\delta a} - \hat{\delta a}^\dagger)(\hat{b}+\hat{b}^\dagger) - x_{\rm z}\hat{F}_{\rm b}(\hat{b}+\hat{b}^\dagger)\\ &- \hbar\sqrt{\frac{2C_0\omega_{\rm s}}{\hbar}}\left[\hat{\delta a}^\dagger\left(\delta\hat{V}_{\rm in}+\hat{V}_{\rm R0}\right) + \hat{\delta a}\left(\delta\hat{V}_{\rm in}^\dagger + \hat{V}_{\rm R0}^\dagger\right)\right],\end{aligned} \tag{2.28}$$

where we have switched to the rotating frame using the unitary transformation $\hat{U} = e^{it\omega_\mathrm{s}\hat{\delta a}^\dagger\hat{\delta a}}$. Notice that we linearized the operator $\hat{V}_\mathrm{in} = \langle\hat{V}_\mathrm{in}\rangle + \delta\hat{V}_\mathrm{in}$, with its average given by the coherent field α at the frequency ω_s, and neglected a term $\propto |\alpha|^2(\hat{b}+\hat{b}^\dagger)$, that can be removed by changing the rest position of the mechanical oscillator.

The equations of motion for the operators $\hat{b}$ and $\hat{\delta a}$ are then given by

$$\dot{\hat{\delta a}} = \frac{g_1\alpha}{\gamma_\mathrm{t}+\gamma_\mathrm{r}}\sqrt{\frac{\gamma_\mathrm{t}}{T}}(\hat{b}+\hat{b}^\dagger) - \frac{\gamma_\mathrm{t}+\gamma_\mathrm{r}}{2}\hat{\delta a} + i\sqrt{\frac{2C_0\omega_\mathrm{s}}{\hbar}}(\delta\hat{V}_\mathrm{in}+\hat{V}_{R_0}), \tag{2.29a}$$

$$\dot{\hat{b}} = -i\omega_\mathrm{m}\hat{b} - \frac{g_1\alpha}{\gamma_\mathrm{t}+\gamma_\mathrm{r}}\sqrt{\frac{\gamma_\mathrm{t}}{T}}(\hat{\delta a}-\hat{\delta a}^\dagger) - \frac{\gamma_\mathrm{b}}{2}\hat{b} + i\frac{x_\mathrm{z}}{\hbar}\hat{F}_\mathrm{b}, \tag{2.29b}$$

where we have linearised in the operators $\hat{\delta a}$ and $\hat{\delta a}^\dagger$. A formal solution in the time domain for these two differential operator equations then reads

$$\begin{aligned}\hat{\delta a}(t) =& \hat{\delta a}(0)e^{-\frac{\gamma_\mathrm{t}+\gamma_\mathrm{r}}{2}t} + \frac{g_1\alpha}{\gamma_\mathrm{t}+\gamma_\mathrm{r}}\sqrt{\frac{\gamma_\mathrm{t}}{T}}\int_0^t e^{-\frac{\gamma_\mathrm{t}+\gamma_\mathrm{r}}{2}(t-\tau)}\left[\hat{b}(\tau)+\hat{b}^\dagger(\tau)\right]d\tau \\ &+ i\sqrt{\frac{2C_0\omega_\mathrm{s}}{\hbar}}\int_0^t e^{-\frac{\gamma_\mathrm{t}+\gamma_\mathrm{r}}{2}(t-\tau)}\left[\delta\hat{V}_\mathrm{in}(\tau)+\hat{V}_{R_0}(\tau)\right]d\tau,\end{aligned} \tag{2.30a}$$

$$\begin{aligned}\hat{b}(t) =& \hat{b}(0)e^{-\left(i\omega_\mathrm{m}+\frac{\gamma_\mathrm{b}}{2}\right)t} - \frac{g_1\alpha}{\gamma_\mathrm{t}+\gamma_\mathrm{r}}\sqrt{\frac{\gamma_\mathrm{t}}{T}}\int_0^t e^{-\left(i\omega_\mathrm{m}+\frac{\gamma_\mathrm{b}}{2}\right)(t-\tau)}\left[\hat{\delta a}(\tau)-\hat{\delta a}^\dagger(\tau)\right]d\tau \\ &+ i\frac{x_\mathrm{z}}{\hbar}\int_0^t e^{-\left(i\omega_\mathrm{m}+\frac{\gamma_\mathrm{b}}{2}\right)(t-\tau)}\hat{F}_\mathrm{b}(\tau)d\tau.\end{aligned} \tag{2.30b}$$

Since we are interested in the average phonon number $\langle\hat{b}^\dagger\hat{b}(t)\rangle$, we can substitute Eq. (2.30a) into Eq. (2.30b), to derive the time evolution of the operator $\hat{b}$ as a function of the noises $\delta\hat{V}_\mathrm{in}$, $\hat{V}_\mathrm{R0}$ and $\hat{F}_\mathrm{b}$:

$$\begin{aligned}\hat{b}(t) =& \hat{b}(0)e^{-\left(i\omega_\mathrm{m}+\frac{\gamma_\mathrm{b}}{2}\right)t} + i\frac{x_\mathrm{z}}{\hbar}\int_0^t e^{-\left(i\omega_\mathrm{m}+\frac{\gamma_\mathrm{b}}{2}\right)(t-\tau)}\hat{F}_\mathrm{b}(\tau)d\tau \\ &- \frac{2g_1\alpha\left[\hat{\delta a}(0)-\hat{\delta a}^\dagger(0)\right]}{(\gamma_\mathrm{t}+\gamma_\mathrm{r})(\gamma_\mathrm{t}+\gamma_\mathrm{r}-\gamma_\mathrm{b}-2i\omega_\mathrm{m})}\sqrt{\frac{\gamma_\mathrm{t}}{T}}\left(e^{-\frac{\gamma_\mathrm{t}+\gamma_\mathrm{r}}{2}t} - e^{-\left(i\omega_\mathrm{m}+\frac{\gamma_\mathrm{b}}{2}\right)t}\right) \\ &+ \frac{ig_1\alpha}{\gamma_\mathrm{t}+\gamma_\mathrm{r}}\sqrt{\frac{\gamma_\mathrm{t}}{T}}\sqrt{\frac{2C_0\omega_\mathrm{s}}{\hbar}}\int_0^t\int_0^{\tau_1}\left\{e^{-\left(i\omega_\mathrm{m}+\frac{\gamma_\mathrm{b}}{2}\right)(t-\tau_1)}e^{-\left(\frac{\gamma_\mathrm{t}+\gamma_\mathrm{r}}{2}\right)(\tau_1-\tau_2)}\right. \\ &\left.\times\left[\delta\hat{V}_\mathrm{in}(\tau_2)+\delta\hat{V}^\dagger_\mathrm{in}(\tau_2)+\hat{V}_\mathrm{R0}(\tau_2)+\hat{V}^\dagger_\mathrm{R0}(\tau_2)\right]\right\}d\tau_1 d\tau_2.\end{aligned} \tag{2.31}$$

Importantly, because we choose to probe the system at the electrical resonance frequency ω_s, the oscillating terms proportional to $\hat{b}(\tau)$ and $\hat{b}^\dagger(\tau)$ in Eq. (2.30a) cancel each other, such that the result simplifies to Eq. (2.31). The above expression is an integral operator equation, the solution of which fully describes the mechanical annihilation operator $\hat{b}(t)$. An analogous relation can be obtained for the creation operator $\hat{b}^\dagger(t)$, by taking the adjoint of Eq. (2.31). In general, this integral is difficult to evaluate. However, assuming the Markov approximation, we can compute the second moments of all the noise operators involved. Thus, even if we cannot solve Eq. (2.31) for $\hat{b}(t)$ or $\hat{b}^\dagger(t)$, we can use (2.31) for determining $n_\mathrm{b}(t) = \langle\hat{b}^\dagger(t)\hat{b}(t)\rangle$. In particular, we use:

$$\left\langle \delta\hat{V}_{\mathrm{in}}^{\dagger}(\tau_1)\delta\hat{V}_{\mathrm{in}}(\tau_2)\right\rangle = \frac{\hbar\gamma_{\mathrm{t}}}{2C_0\omega_{\mathrm{s}}}\bar{n}_{\mathrm{e}}(\omega_{\mathrm{s}},T_{\mathrm{e}})\delta(\tau_2-\tau_1), \tag{2.32a}$$

$$\left\langle \delta\hat{V}_{\mathrm{in}}(\tau_1)\delta\hat{V}_{\mathrm{in}}^{\dagger}(\tau_2)\right\rangle = \frac{\hbar\gamma_{\mathrm{t}}}{2C_0\omega_{\mathrm{s}}}\left[\bar{n}_{\mathrm{e}}(\omega_{\mathrm{s}},T_{\mathrm{e}})+1\right]\delta(\tau_2-\tau_1), \tag{2.32b}$$

$$\left\langle \hat{V}_{\mathrm{R0}}^{\dagger}(\tau_1)\hat{V}_{\mathrm{R0}}(\tau_2)\right\rangle = \frac{\hbar\gamma_{\mathrm{r}}}{2C_0\omega_{\mathrm{s}}}\bar{n}_{\mathrm{e}}(\omega_{\mathrm{s}},T_{\mathrm{e}})\delta(\tau_2-\tau_1), \tag{2.32c}$$

$$\left\langle \hat{V}_{\mathrm{R0}}(\tau_1)\hat{V}_{\mathrm{R0}}^{\dagger}(\tau_2)\right\rangle = \frac{\hbar\gamma_{\mathrm{r}}}{2C_0\omega_{\mathrm{s}}}\left[\bar{n}_{\mathrm{e}}(\omega_{\mathrm{s}},T_{\mathrm{e}})+1\right]\delta(\tau_2-\tau_1), \tag{2.32d}$$

$$\left\langle \hat{F}_{\mathrm{b}}^{\dagger}(\tau_1)\hat{F}_{\mathrm{b}}(\tau_2)\right\rangle = 2\hbar m\omega_{\mathrm{m}}\bar{n}_{\mathrm{m}}(\omega_{\mathrm{m}},T_{\mathrm{m}})\delta(\tau_2-\tau_1), \tag{2.32e}$$

$$\left\langle \hat{F}_{\mathrm{b}}(\tau_1)\hat{F}_{\mathrm{b}}^{\dagger}(\tau_2)\right\rangle = 2\hbar m\omega_{\mathrm{m}}\left[\bar{n}_{\mathrm{m}}(\omega_{\mathrm{m}},T_{\mathrm{m}})+1\right]\delta(\tau_2-\tau_1), \tag{2.32f}$$

where $\bar{n}_{\mathrm{e}}(\omega_{\mathrm{s}},T_{\mathrm{e}})$ and $\bar{n}_{\mathrm{m}}(\omega_{\mathrm{m}},T_{\mathrm{m}})$ are the average thermal occupation numbers of the electrical and mechanical reservoirs at temperatures T_{e} and T_{m}, respectively. In the following, we omit their argument, assuming that they refer to the frequencies ω_{s} (electrical) and ω_{m} (mechanical), and temperatures T_{e} (electrical) and T_{m} (mechanical) of the respective systems. The requirements on the reservoirs necessary to write the second moments of the noises as in Eqs. (2.32) are the following. First, the mechanical force $\hat{F}_{\mathrm{b}}$ needs to vary on a timescale much faster than the membrane's decay time, which is fulfilled for $\gamma_{\mathrm{b}} \ll \omega_{\mathrm{m}}$. Second, we have neglected the difference between the electrical excitation number $\bar{n}_{\mathrm{e}}$ at the central frequency and the mechanical sidebands. This means that the electrical resonance frequency has to be much bigger than the mechanical one ($\omega_{\mathrm{s}} \gg \omega_{\mathrm{m}}$). Both these requirements are satisfied for the considered experimental parameters.

Knowing the second moments of all noise operators, and neglecting the term proportional to $\langle \hat{\delta a}^{\dagger}(0)\hat{\delta a}(0)\rangle$, using Eq. (2.31) we can find $n_{\mathrm{b}}(t) = \langle \hat{n}_{\mathrm{b}}(t)\rangle$ to be

$$\begin{aligned} n_{\mathrm{b}}(t) =& n_{\mathrm{b}}(0)e^{-\gamma_{\mathrm{b}}t} + \bar{n}_{\mathrm{m}}\left(1-e^{-\gamma_{\mathrm{b}}t}\right) - \frac{4g_1^2|\alpha|^2\gamma_{\mathrm{t}}(1+2\bar{n}_{\mathrm{e}})e^{-(\gamma_{\mathrm{t}}+\gamma_{\mathrm{r}})t}}{T(\gamma_{\mathrm{t}}+\gamma_{\mathrm{r}})^2\left[(-\gamma_{\mathrm{b}}+\gamma_{\mathrm{t}}+\gamma_{\mathrm{r}})^2+4\omega_{\mathrm{m}}^2\right]} \\ &+ \frac{8g_1^2|\alpha|^2\gamma_{\mathrm{t}}(1+2\bar{n}_{\mathrm{e}})e^{-\frac{\gamma_{\mathrm{b}}+\gamma_{\mathrm{t}}+\gamma_{\mathrm{r}}}{2}t}}{T(\gamma_{\mathrm{t}}+\gamma_{\mathrm{r}})\left[(-\gamma_{\mathrm{b}}+\gamma_{\mathrm{t}}+\gamma_{\mathrm{r}})^2+4\omega_{\mathrm{m}}^2\right]}\left(\frac{e^{-i\omega_{\mathrm{m}}t}}{\gamma_{\mathrm{b}}+\gamma_{\mathrm{t}}+\gamma_{\mathrm{r}}+2i\omega_{\mathrm{m}}}\right. \\ &+ \left.\frac{e^{i\omega_{\mathrm{m}}t}}{\gamma_{\mathrm{b}}+\gamma_{\mathrm{t}}+\gamma_{\mathrm{r}}-2i\omega_{\mathrm{m}}}\right) + \frac{4g_1^2|\alpha|^2\gamma_{\mathrm{t}}(\gamma_{\mathrm{b}}+\gamma_{\mathrm{t}}+\gamma_{\mathrm{r}})(1+2\bar{n}_{\mathrm{e}})}{T\gamma_{\mathrm{b}}(\gamma_{\mathrm{t}}+\gamma_{\mathrm{r}})^2\left[(-\gamma_{\mathrm{b}}+\gamma_{\mathrm{t}}+\gamma_{\mathrm{r}})^2+4\omega_{\mathrm{m}}^2\right]} \\ &- \frac{4g_1^2|\alpha|^2\gamma_{\mathrm{t}}(1+2\bar{n}_{\mathrm{e}})e^{-\gamma_{\mathrm{b}}t}}{T\gamma_{\mathrm{b}}(\gamma_{\mathrm{t}}+\gamma_{\mathrm{r}})\left[(-\gamma_{\mathrm{b}}+\gamma_{\mathrm{t}}+\gamma_{\mathrm{r}})^2+4\omega_{\mathrm{m}}^2\right]}, \end{aligned} \tag{2.33}$$

where the first two terms $n_{\mathrm{b}}(0)e^{-\gamma_{\mathrm{b}}t} + \bar{n}_{\mathrm{m}}\left(1-e^{-\gamma_{\mathrm{b}}t}\right)$ describe the usual time evolution of a free membrane influenced by its own thermal bath, and everything else is the dynamics induced from the electrical system.

Eq. (2.33) represents an exact result in the limit in which the photonic ($\bar{n}_{\mathrm{e}}$) and phononic ($\bar{n}_{\mathrm{m}}$) reservoirs are Markovian. However, it can be better understood if we assume the mechanical damping γ_{b} to be much smaller than the electrical one, $\gamma_{\mathrm{t}}+\gamma_{\mathrm{r}}$. In particular, if we are probing the system on a time scale that is much longer than the electrical lifetime, i.e. $t \gg (\gamma_{\mathrm{t}}+\gamma_{\mathrm{r}})^{-1}$, we can rewrite Eq. (2.33) as

$$n_{\mathrm{b}}(t) = n_{\mathrm{b}}(0)e^{-\gamma_{\mathrm{b}}t} + \left[\bar{n}_{\mathrm{m}} + \frac{\Gamma_{\mathrm{b}}}{\gamma_{\mathrm{b}}}(1+2\bar{n}_{\mathrm{e}})\right]\left(1-e^{-\gamma_{\mathrm{b}}t}\right), \tag{2.34}$$

where we have defined the induced heating Γ_b to be

$$\Gamma_\mathrm{b} = \frac{4g_1^2|\alpha|^2\gamma_\mathrm{t}}{T(\gamma_\mathrm{t}+\gamma_\mathrm{r})\left[(\gamma_\mathrm{t}+\gamma_\mathrm{r})^2+4\omega_\mathrm{m}^2\right]}. \tag{2.35}$$

Equation (2.34) has been compared with numerical simulations of the master equation of the Hamiltonian in Eq. (2.28), taking into account the electrical and mechanical reservoirs. Examples are given in Fig. 2.8.

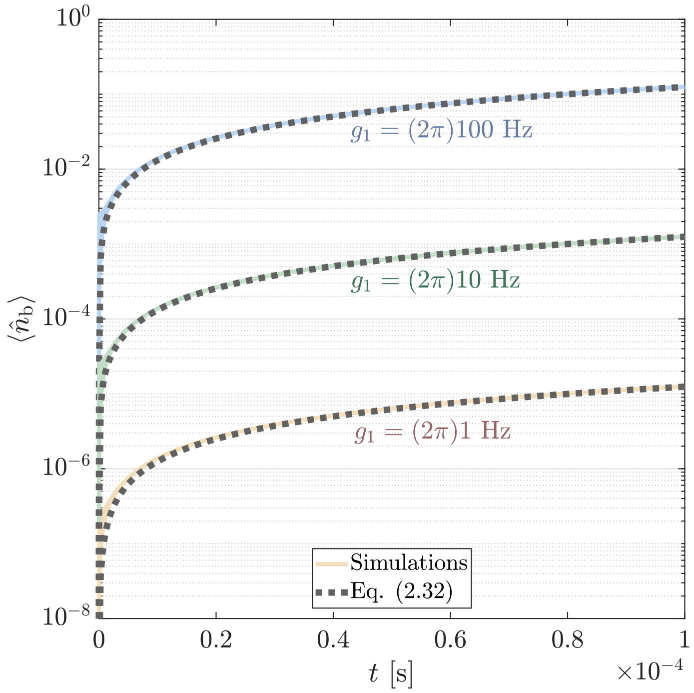

FIGURE 2.8: Examples for the dynamics of the average mechanical phonon number $n_\mathrm{b}(t)$. The dotted curves are the analytical results given in Eq. (2.34). The solid curves comes from numerically solving the master equation with the Hamiltonian of Eq. (2.28) and the electrical and mechanical reservoirs (using the Markov approximation). The three sets differ from the parameter g_1, that has been taken to be equal to $(2\pi)100$ Hz (top set), $(2\pi)10$ Hz (middle set), and $(2\pi)1$ Hz (bottom set). We assume that $|\alpha|^2 = 10^{12}$ photons are sent into the system for the duration T of the measurement, and we used the parameters: $\omega_\mathrm{m} = (2\pi)100$ MHz, $\omega_\mathrm{s} = (2\pi)5$ GHz, $\gamma_\mathrm{r} = \gamma_\mathrm{t} = (2\pi)1$ MHz, $\gamma_\mathrm{b} = (2\pi)100$ Hz, $T = 100$ μs, $\bar{n}_\mathrm{e} = 0$ and $\bar{n}_\mathrm{m} = 0$.

From the above expressions, we can determine the parameter Δn_b by finding the first order expansion of the function $n_\mathrm{b}(t)$ in Eq. (2.34) with $n_\mathrm{b}(0) = 0$,

$$\Delta n_\mathrm{b} = \gamma_\mathrm{b}\bar{n}_\mathrm{m}T + \Gamma_\mathrm{b}(1+2\bar{n}_\mathrm{e})T. \tag{2.36}$$

The form of Δn_b given in Eq. (2.4) assumes $\gamma_\mathrm{b} \ll \frac{\Gamma_\mathrm{b}}{\bar{n}_\mathrm{m}}$. Having determined both D^2 and Δn_b, it is possible to derive the general form of the parameter λ in Eq. (2.1), including the contribution from the mechanical reservoir.

2.2.2 ‘Double arm’ circuit

In the following we derive the parameter λ for the ‘double arm’ circuit, introduced to take into account the coupling to the antisymmetric mode associated with the redistribution of charge on the membrane. This is depicted in Fig. 2.9. We include possible asymmetries in the fabrication process, the effect of which can be described by a residual linear coupling g_r. The contribution to λ from other kinds of asymmetries – different parasitic resistances and inductances – will only be investigated numerically, since the analytical results are too long and complicated in this case.

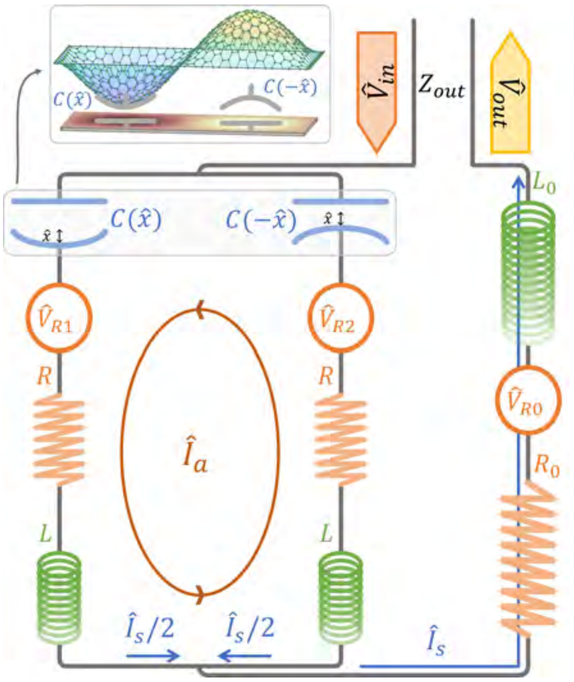

FIGURE 2.9: ‘Double arm’ model of the considered electromechanical setup, with parasitic resistances (R) and inductances (L). We take into account the Johnson–Nyquist noises associated with the main resistor R_0 and the two parasitic ones: $\hat{V}_{R0}$, $\hat{V}_{R1}$ and $\hat{V}_{R2}$, respectively. $\hat{I}_s$ and $\hat{I}_a$ are the two electrical currents considered in our analysis, and $C(\pm\hat{x})$ represent the two halves of the capacitor. In the inset we sketch how $C(\pm\hat{x})$ may arise.

Using the currents $\hat{I}_s$ and $\hat{I}_a$ and their associated charges $\hat{Q}_s$ and $\hat{Q}_a$, we can determine the Hamiltonian of the circuit in Fig. 2.9 to be

$$\begin{aligned}\hat{\mathcal{H}} =& \hbar\omega_m \hat{b}^\dagger \hat{b} - x_z\left(\hat{b}^\dagger + \hat{b}\right)\hat{F}_b + \frac{\hat{\Phi}_a^2}{4L} + \frac{\hat{Q}_a^2}{C_0} + \frac{\hat{\Phi}_s^2}{L+2L_0} + \frac{\hat{Q}_s^2}{4C_0} - \hat{Q}_s(2\hat{V}_{in} + 2\hat{V}_{R0} + \hat{V}_{R1} + \hat{V}_{R2}) \\ & - 2\hat{Q}_a(\hat{V}_{R2} - \hat{V}_{R1}) + \frac{g_1}{C_0\omega_s}\hat{Q}_a\hat{Q}_s\left(\hat{b} + \hat{b}^\dagger\right) + \frac{g_2}{C_0\omega_s}\hat{Q}_a^2\hat{b}^\dagger\hat{b} + \frac{g_2}{4C_0\omega_s}\hat{Q}_s^2\hat{b}^\dagger\hat{b},\end{aligned} \tag{2.37}$$

where the magnetic fluxes $\hat{\Phi}_a$ and $\hat{\Phi}_s$ are defined below. In principle, there are other terms proportional to $g_2\hat{b}\hat{b}$ and $g_2\hat{b}^\dagger\hat{b}^\dagger$ in the Hamiltonian. These are responsible for sidebands at frequencies $\omega_s \pm 2\omega_m$, that we have already encountered in section 2.2.1. For the same reasons explained there, these terms do not contribute neither to the electrical readout (homodyne measurement at frequency ω_s) nor to the heating ($g_2 \ll g_1$), and we shall therefore ignore them in the following. A quantitative reason for neglecting these two–phonon processes, is the following. With Fermi Golden rule, we can determine the rate at which these processes happen to be

$$\frac{g_2^2|\alpha|^2\gamma_\mathrm{t}}{\left(\frac{\gamma_\mathrm{r}+\gamma_\mathrm{t}}{2}\right)^2+(2\omega_\mathrm{m})^2}, \tag{2.38}$$

that is orders of magnitude lower than $\Delta n_\mathrm{b}/T$ (the one–phonon processes induced by the linear coupling), as can be estimated later in section 2.2.4, where parameters for a proposed implementation are given. Notice that the rate in Eq. (2.38) describes the two phonon processes relative to the term $\propto g_2\hat{Q}_\mathrm{s}^2$ in the Hamiltonian in Eq. (2.37). The other two phonon process, $\propto g_2\hat{Q}_\mathrm{a}^2$, is even more suppressed, as the asymmetric field is not directly driven by the input $\hat{V}_\mathrm{in}$.

From Eq. (2.37), it is possible to derive the equations of motion for the fields $\hat{Q}_\mathrm{a}$, $\hat{Q}_\mathrm{s}$, $\hat{\Phi}_\mathrm{a}$, $\hat{\Phi}_\mathrm{s}$ and $\hat{b}$. The electrical decays are included using Kirchoff laws, resulting in:

$$\begin{align}
\dot{\hat{\Phi}}_\mathrm{a} =& -2\frac{\hat{Q}_\mathrm{a}}{C_0} - \frac{g_1}{C_0\omega_\mathrm{s}}\hat{Q}_\mathrm{s}\left(\hat{b}+\hat{b}^\dagger\right) - \frac{2g_2}{C_0\omega_\mathrm{s}}\hat{Q}_\mathrm{a}\hat{n}_\mathrm{b} - \gamma_\mathrm{l}\hat{\Phi}_\mathrm{a} + 2\left(\hat{V}_\mathrm{R2}-\hat{V}_\mathrm{R1}\right), \tag{2.39a}\\
\dot{\hat{Q}}_\mathrm{a} =& \frac{\hat{\Phi}_\mathrm{a}}{2L}, \tag{2.39b}\\
\dot{\hat{\Phi}}_\mathrm{s} =& -\frac{\hat{Q}_\mathrm{s}}{2C_0} - \frac{g_1}{C_0\omega_\mathrm{s}}\hat{Q}_\mathrm{a}\left(\hat{b}+\hat{b}^\dagger\right) - \frac{g_2}{2C_0\omega_\mathrm{s}}\hat{Q}_\mathrm{s}\hat{n}_\mathrm{b} - (\gamma_\mathrm{t}+\gamma_\mathrm{r})\hat{\Phi}_\mathrm{s} + 2\hat{V}_\mathrm{in} \nonumber\\
&+ 2\hat{V}_\mathrm{R0} + \hat{V}_\mathrm{R1} + \hat{V}_\mathrm{R2}, \tag{2.39c}\\
\dot{\hat{Q}}_\mathrm{s} =& \frac{2\hat{\Phi}_\mathrm{s}}{L+2L_0}, \tag{2.39d}\\
\dot{\hat{b}} =& -i\omega_\mathrm{m}\hat{b} - \frac{i}{\hbar}\frac{g_1}{C_0\omega_\mathrm{s}}\hat{Q}_\mathrm{a}\hat{Q}_\mathrm{s} - \frac{i}{\hbar}\frac{g_2}{C_0\omega_\mathrm{s}}\left(\hat{Q}_\mathrm{a}^2+\frac{\hat{Q}_\mathrm{s}^2}{4}\right)\hat{b} - \frac{\gamma_\mathrm{b}}{2}\hat{b} + \frac{x_\mathrm{z}}{\hbar}\hat{F}_\mathrm{b}. \tag{2.39e}
\end{align}$$

To enable a direct comparison with the RLC circuit presented in section 2.2.1 we have here used the same notation. This requires small differences in the definitions, to take into account the parasitic resistances and inductances:

$$\begin{align}
\omega_\mathrm{s}^2 &= \frac{1}{C_0(L+2L_0)}, \tag{2.40a}\\
\omega_\mathrm{a}^2 &= \frac{1}{C_0L}, \tag{2.40b}\\
\gamma_\mathrm{t} &= \frac{2Z_\mathrm{out}}{L+2L_0}, \tag{2.40c}\\
\gamma_\mathrm{r} &= \frac{R+2R_0}{L+2L_0}, \tag{2.40d}\\
\gamma_\mathrm{l} &= \frac{R}{L}. \tag{2.40e}
\end{align}$$

Moreover, the linear and quadratic couplings g_1 and g_2 come from the expansions of *each* one of the two capacitors $C(\pm\hat{x})$ in the mechanical position $\hat{x}$, as suggested by the inset in Fig. 2.9. Following the same procedure used for the RLC circuit, we first study the measurement of $\hat{n}_\mathrm{b}$, and later identify the conditions under which the measurement is effectively QND.

Notice that, depending on the specific experimental setup, other circuit scheme may be better suited for describing the system. For instance, in the experiment of

Ref. [42] the mechanical oscillator is not directly connected to the circuit, and different equivalent circuit would be required. Here, we restrict ourselves to the setup in Fig. 2.9 and defer other setup for later investigation [92].

QND measurement of the phonon number, and comparison with the 'membrane in the middle' setup [78]

Assuming that the mechanical state is unchanged during the whole measurement time T, we can neglect all sources of heating in the system of equations (2.39), and take $\hat{n}_\mathrm{b}$ to be constant in time. Importantly, for the setup in Fig. 2.9 there are two mechanisms that shift the resonant frequency ω_s and thus allow for the QND measurement. The first one we encountered before for the RLC circuit, and relates to the quadratic electromechanical coupling: $\omega_\mathrm{s} \to \omega_\mathrm{s} + g_2 n_\mathrm{b}$. The second is more involved, and is the same one considered in the optomechanical setup of Ref. [45]. It relies on an effective quadratic coupling proportional to g_1^2, that arises once we substitute Eqs. (2.39a) and (2.39b) into Eqs. (2.39c) and (2.39d). To better understand this process, it is instructive to look at the final equation for $\hat{\Phi}_\mathrm{s}$ in the frequency domain:

$$\begin{aligned}\hat{\Phi}_\mathrm{s}[\Omega_k]\Bigg(&\overbrace{\frac{(\hat{n}_\mathrm{b}+1)g_1^2\omega_\mathrm{a}^2}{\omega_\mathrm{a}^2+(\Omega_k-\omega_\mathrm{m})(-i\gamma_\mathrm{l}-\Omega_k+\omega_\mathrm{m})}+\frac{\hat{n}_\mathrm{b}g_1^2\omega_\mathrm{a}^2}{\omega_\mathrm{a}^2-(\Omega_k+\omega_\mathrm{m})(i\gamma_\mathrm{l}+\Omega_k+\omega_\mathrm{m})}}^{g_1^2\text{ shift}}\\ &-\overbrace{g_2\omega_\mathrm{s}\hat{n}_\mathrm{b}}^{g_2\text{ shift}}+\Omega_k^2-\omega_\mathrm{s}^2\Bigg)=i\Omega_k(\gamma_\mathrm{r}+\gamma_\mathrm{t})\hat{\Phi}_\mathrm{s}[\Omega_k]+2i\Omega_k\hat{V}_\mathrm{in}[\Omega_k]+2i\Omega_k\hat{V}_\mathrm{R0}[\Omega_k]\\ &+i\Omega_k\hat{V}_\mathrm{R1}[\Omega_k]+i\Omega_k\hat{V}_\mathrm{R2}[\Omega_k],\end{aligned}\tag{2.41}$$

where we neglected off–resonant terms and assumed $g_2 \ll \omega_\mathrm{s}$. As indicated explicitly in Eq. (2.41), it is possible to see the frequency shifts induced by the linear g_1 and quadratic g_2 couplings. Whether the QND interaction is dominated by the quadratic coupling g_2 or the effective quadratic interaction $\propto g_1^2$, depends on the resonance condition of the symmetric $\hat{I}_\mathrm{s}$ and antisymmetric $\hat{I}_\mathrm{a}$ modes in Fig. 2.9. To have a sizeable effect of the g_1 term, we need to be near resonance with the antisymmetric mode $\Omega_k \simeq \omega_\mathrm{a} \gg \omega_\mathrm{m}, \gamma_\mathrm{l}$. At the same time, for the QND detection we probe the system at the resonance frequency $\Omega_k \simeq \omega_\mathrm{s}$. Hence, the g_1 term is dominant when we allow for a strong hybridization of the two electrical modes: $\omega_\mathrm{s} \simeq \omega_\mathrm{a}$. In such situation, by determining the heating rate for the electromechanical setup (see Sec. 2.2.2), we can derive the condition for a feasible QND detection:

$$\lambda = \frac{2}{(1+\bar{n}_\mathrm{e})(1+2\bar{n}_\mathrm{e})}\frac{g_1^2}{(\gamma_\mathrm{r}+\gamma_\mathrm{t})^2}\frac{\gamma_\mathrm{t}}{\gamma_\mathrm{l}} \gg 1. \tag{2.42}$$

This condition is similar to the one found in Ref. [78] for the experiment in Ref. [45], where strong heating was proven to forbid the QND detection. Compared to that work, however, we gain the factor $\gamma_\mathrm{t}/\gamma_\mathrm{l}$, that comes from the asymmetry between the damping of the two electrical modes. Hence, our setup does have some gain compared to the RLC circuit, if the damping of the antisymmetric mode is small: $\gamma_\mathrm{l} \ll \gamma_\mathrm{t}$. However, in this case the QND measurement still faces the challenge of a strong heating of the mechanical motion due to the large coupling between the electrical modes, and requires $g_1^2 \gg \gamma_\mathrm{l}\gamma_\mathrm{t}$.

In the following, we investigate the opposite limit, where the antisymmetric mode $\hat{I}_\mathrm{a}$ is far–off resonant from the symmetric one $\hat{I}_\mathrm{s}$. In this case, the quadratic coupling g_2 is dominant[3], and the heating induced to the mechanical mode will be strongly suppressed. If we neglect the effective quadratic coupling $\propto g_1^2$, we only need to consider Eqs. (2.39c) and (2.39d) for determining the measurement signal. In the absence of heating, these are uncoupled from both the mechanics and the other electrical modes. We can then derive relations for $\hat{\Phi}_\mathrm{s}[\Omega_k]$ and $\hat{Q}_\mathrm{s}[\Omega_k]$ similar to Eqs. (2.17):

$$\begin{aligned} -i\Omega_k\hat{\Phi}_\mathrm{s}[\Omega_k] =& -\frac{\hat{Q}_\mathrm{s}[\Omega_k]}{2C_0} - \frac{g_2\omega_\mathrm{s}L_0}{2}\hat{Q}_\mathrm{s}[\Omega_k]\hat{n}_\mathrm{b} - (\gamma_\mathrm{r}+\gamma_\mathrm{t})\hat{\Phi}_\mathrm{s}[\Omega_k] \\ &+ 2(\hat{V}_\mathrm{in}[\Omega_k] + \hat{V}_\mathrm{R0}[\Omega_k]) + \hat{V}_\mathrm{R1}[\Omega_k] + \hat{V}_\mathrm{R2}[\Omega_k], \end{aligned} \tag{2.43a}$$

$$-i\Omega_k\hat{Q}_\mathrm{s}[\Omega_k] = \frac{2\hat{\Phi}_\mathrm{s}[\Omega_k]}{L+2L_0}. \tag{2.43b}$$

The reflected field $\hat{V}_\mathrm{out}[\Omega_k]$ is

$$\hat{V}_\mathrm{out}[\Omega_k] = [1-\zeta(\Omega_k,\hat{n}_\mathrm{b})]\,\hat{V}_\mathrm{in}[\Omega_k] - \zeta(\Omega_k,\hat{n}_\mathrm{b})\left(\hat{V}_\mathrm{R0}[\Omega_k] + \frac{\hat{V}_\mathrm{R1}[\Omega_k]+\hat{V}_\mathrm{R2}[\Omega_k]}{2}\right), \tag{2.44}$$

where we have used the input/output relation $\hat{V}_\mathrm{out} = \hat{V}_\mathrm{in} - \gamma_\mathrm{t}\hat{\Phi}_\mathrm{s}$. The coefficient $\zeta(\Omega_k,\hat{n}_\mathrm{b})$ is the same as in Eq. (2.18b), except for a factor 2 coming from the fact that, here, we are considering the two halves of our capacitor. With the outcome of the homodyne detection being described by the same operator $\hat{V}_\mathrm{M}$ defined in Eq. (2.20), we can find the parameter D^2 for the setup in Fig. 2.9 to be

$$D^2 = \frac{d^2}{\sigma^2} = \frac{16}{1+2\bar{n}_\mathrm{e}}\frac{g_2^2|\alpha|^2\gamma_\mathrm{t}^2}{\left[g_2^2+(\gamma_\mathrm{t}+\gamma_\mathrm{r})^2\right]^2}. \tag{2.45}$$

Notice that for deriving Eq. (2.45) from Eq. (2.44) we assumed that the electrical reservoirs are in a thermal state with average photon number $\bar{n}_\mathrm{e}$, and that the drive is a coherent state α at the frequency ω_s. Consistent with previous sections, α is chosen to be real and the phase of the homodyne measurement is fixed such that $\theta = \pi$ in Eq. (2.20).

Membrane heating

Given that $g_2 \ll g_1$, we set the quadratic coupling to zero in this subsection. We can then rewrite the Hamiltonian in Eq. (2.37) in the form

$$\begin{aligned} \hat{\mathcal{H}} =& \hbar\omega_\mathrm{m}\hat{b}^\dagger\hat{b} - x_\mathrm{z}\left(\hat{b}^\dagger+\hat{b}\right)\hat{F}_\mathrm{b} + \frac{\hat{\Phi}_\mathrm{a}^2}{4L} + \frac{\hat{Q}_\mathrm{a}^2}{C_0} + \frac{\hat{\Phi}_\mathrm{s}^2}{L+2L_0} + \frac{\hat{Q}_\mathrm{s}^2}{4C_0} \\ &- \hat{Q}_\mathrm{s}(2\hat{V}_\mathrm{in} + 2\hat{V}_\mathrm{R0} + \hat{V}_\mathrm{R1} + \hat{V}_\mathrm{R2}) - 2\hat{Q}_\mathrm{a}(\hat{V}_\mathrm{R2} - \hat{V}_\mathrm{R1}) + \frac{g_1}{C_0\omega_\mathrm{s}}\hat{Q}_\mathrm{a}\hat{Q}_\mathrm{s}\left(\hat{b}+\hat{b}^\dagger\right). \end{aligned} \tag{2.46}$$

Moreover, by looking at Eqs. (2.39), it is possible to see that $\hat{Q}_\mathrm{s}$ and $\hat{\Phi}_\mathrm{s}$ are the only driven fields in the system (with $\hat{V}_\mathrm{R0}$, $\hat{V}_\mathrm{R1}$ and $\hat{V}_\mathrm{R2}$ being in a thermal state). Therefore, we can neglect perturbations induced by the mechanical motion, and substitute them with their average values $\langle\hat{Q}_\mathrm{s}\rangle$ and $\langle\hat{\Phi}_\mathrm{s}\rangle$. This assumption will be verified in subsection 2.2.2, where we simulate the dynamics of the electromechanical system

---

[3] This is true, as far as $g_2 \gg g_1^2/\omega_s$. In case this condition is not fulfilled, one can simply redefine the quadratic coupling to take all contributions into account.

in the general case in which the parasitic elements may differ from each other. From the Hamiltonian Eq. (2.46) we can determine the equations of motion for $\langle\hat{Q}_\mathrm{s}\rangle$ and $\langle\hat{\Phi}_\mathrm{s}\rangle$:

$$\begin{aligned} \langle\dot{\hat{\Phi}}_\mathrm{s}(t)\rangle =& -\frac{\langle\hat{Q}_\mathrm{s}(t)\rangle}{2C_0} - (\gamma_\mathrm{t}+\gamma_\mathrm{r})\langle\hat{\Phi}_\mathrm{s}(t)\rangle + 2\langle\hat{V}_\mathrm{in}(t)\rangle, && \text{(2.47a)} \\ \langle\dot{\hat{Q}}_\mathrm{s}(t)\rangle =& \frac{2\langle\hat{\Phi}_\mathrm{s}(t)\rangle}{L+2L_0}, && \text{(2.47b)} \end{aligned}$$

where $\langle\hat{V}_\mathrm{in}(t)\rangle = \alpha\sqrt{2\hbar\omega_\mathrm{s}Z_\mathrm{out}/T}\cos(\omega_\mathrm{s}t)$. Similar to above, we are mainly interested in the case of constant incident fields or long pulses, such that we ignore transient behaviours. The steady state solution for the charge $\langle\hat{Q}_\mathrm{s}(t)\rangle$ is then given by

$$\langle\hat{Q}_\mathrm{s}(t)\rangle = -\frac{2i\alpha}{\gamma_\mathrm{t}+\gamma_\mathrm{r}}\sqrt{\frac{\hbar C_0\omega_\mathrm{s}\gamma_\mathrm{t}}{T}}\left(e^{i\omega_\mathrm{s}t} - e^{-i\omega_\mathrm{s}t}\right). \tag{2.48}$$

Assuming that the strongly driven symmetric fields $\hat{Q}_\mathrm{s}$ and $\hat{\Phi}_\mathrm{s}$ are not perturbed by the mechanical dynamics, we can substitute Eq. (2.48) into the Hamiltonian of Eq. (2.46), and obtain

$$\begin{aligned} \hat{\mathcal{H}} =& \hbar\omega_\mathrm{m}\hat{b}^\dagger\hat{b} - x_\mathrm{z}\left(\hat{b}^\dagger + \hat{b}\right)\hat{F}_\mathrm{b} + \frac{\hat{\Phi}_\mathrm{a}^2}{4L} + \frac{\hat{Q}_\mathrm{a}^2}{C_0} - 2\hat{Q}_\mathrm{a}(\hat{V}_\mathrm{R1} - \hat{V}_\mathrm{R1}) \\ & - \frac{2i\hbar g_1\alpha}{\gamma_\mathrm{t}+\gamma_\mathrm{r}}\sqrt{\frac{\gamma_\mathrm{t}}{\hbar TC_0\omega_\mathrm{s}}}\left(e^{i\omega_\mathrm{s}t} - e^{-i\omega_\mathrm{s}t}\right)\hat{Q}_\mathrm{a}\left(\hat{b} + \hat{b}^\dagger\right). \end{aligned} \tag{2.49}$$

Differential equations for $\hat{Q}_\mathrm{a}$, $\hat{\Phi}_\mathrm{a}$, and the mechanical annihilation operator $\hat{b}$ can finally be derived:

$$\begin{aligned} \dot{\hat{\Phi}}_\mathrm{a} =& -2\frac{\hat{Q}_\mathrm{a}}{C_0} + \frac{2ig_1\alpha}{\gamma_\mathrm{t}+\gamma_\mathrm{r}}\sqrt{\frac{\hbar\gamma_\mathrm{t}}{TC_0\omega_\mathrm{s}}}\left(e^{-i\omega_\mathrm{s}t} - e^{i\omega_\mathrm{s}t}\right)\left(\hat{b} + \hat{b}^\dagger\right) - \gamma_1\hat{\Phi}_\mathrm{a} + 2\left(\hat{V}_\mathrm{R2} - \hat{V}_\mathrm{R1}\right), \\ & && \text{(2.50a)} \\ \dot{\hat{Q}}_\mathrm{a} =& \frac{\hat{\Phi}_\mathrm{a}}{2L}, && \text{(2.50b)} \\ \dot{\hat{b}} =& -i\omega_\mathrm{m}\hat{b} - \frac{2g_1\alpha}{\gamma_\mathrm{t}+\gamma_\mathrm{r}}\sqrt{\frac{\gamma_\mathrm{t}}{\hbar TC_0\omega_\mathrm{s}}}\left(e^{-i\omega_\mathrm{s}t} - e^{i\omega_\mathrm{s}t}\right)\hat{Q}_\mathrm{a} - \frac{\gamma_\mathrm{b}}{2}\hat{b} + i\frac{x_\mathrm{z}}{\hbar}\hat{F}_\mathrm{b}. && \text{(2.50c)} \end{aligned}$$

These equations describe the coupling of the mechanical mode to the antisymmetric electrical one. This coupling is enhanced by driving the symmetric mode with the coherent state α, and is responsible for heating up the membrane, similarly to Ref. [78]. Therefore, we need to assess to which degree this is deleterious for the QND measurement of $\hat{n}_\mathrm{b}$. Equations (2.50) are nontrivial, and exact solutions are not accessible. However, under reasonable assumptions, we are able to find an approximate analytical solution that will be subsequently confirmed by our numerical approach.

Our first step for dealing with the system (2.50) is to switch to the Fourier domain:

$$\begin{aligned}-i\Omega_k\hat{\Phi}_{\mathrm{a}}\left[\Omega_k\right] =& -2\frac{\hat{Q}_{\mathrm{a}}\left[\Omega_k\right]}{C_0}+\frac{2ig_1\alpha}{\gamma_{\mathrm{t}}+\gamma_{\mathrm{r}}}\sqrt{\frac{\hbar\gamma_{\mathrm{t}}}{TC_0\omega_{\mathrm{s}}}}\Big(\hat{b}\left[\Omega_k-\omega_{\mathrm{s}}\right]+\hat{b}^{\dagger}\left[\Omega_k-\omega_{\mathrm{s}}\right]\\ &-\hat{b}\left[\Omega_k+\omega_{\mathrm{s}}\right]-\hat{b}^{\dagger}\left[\Omega_k+\omega_{\mathrm{s}}\right]\Big)-\gamma_{\mathrm{l}}\hat{\Phi}_{\mathrm{a}}\left[\Omega_k\right]+2\left(\hat{V}_{\mathrm{R2}}\left[\Omega_k\right]-\hat{V}_{\mathrm{R1}}\left[\Omega_k\right]\right),\end{aligned} \tag{2.51a}$$

$$-i\Omega_k\hat{Q}_{\mathrm{a}}\left[\Omega_k\right]=\frac{\hat{\Phi}_{\mathrm{a}}\left[\Omega_k\right]}{2L}, \tag{2.51b}$$

$$\begin{aligned}-i\Omega_k\hat{b}\left[\Omega_k\right]=& -i\omega_{\mathrm{m}}\hat{b}\left[\Omega_k\right]-\frac{2g_1\alpha}{\gamma_{\mathrm{t}}+\gamma_{\mathrm{r}}}\sqrt{\frac{\gamma_{\mathrm{t}}}{\hbar TC_0\omega_{\mathrm{s}}}}\left(\hat{Q}_{\mathrm{a}}\left[\Omega_k-\omega_{\mathrm{s}}\right]-\hat{Q}_{\mathrm{a}}\left[\Omega_k+\omega_{\mathrm{s}}\right]\right)\\ &-\frac{\gamma_{\mathrm{b}}}{2}\hat{b}\left[\Omega_k\right]+i\frac{x_{\mathrm{z}}}{\hbar}\hat{F}_{\mathrm{b}}\left[\Omega_k\right].\end{aligned} \tag{2.51c}$$

We can employ equations (2.51a) and (2.51b) in order to obtain an expression for $\hat{b}\left[\Omega_k\right]$ that depends on the noises only

$$\begin{aligned}\hat{b}\left[\Omega_k\right]\left(\frac{\gamma_{\mathrm{b}}+\Gamma_{\mathrm{b}}(\Omega_k)}{2}-i\left[\Omega_k-\omega_{\mathrm{m}}-\omega_{\mathrm{b}}(\Omega_k)\right]\right)=i\frac{x_{\mathrm{z}}}{\hbar}\hat{F}_{\mathrm{b}}\left[\Omega_k\right]+\frac{2g_1\alpha}{\gamma_{\mathrm{t}}+\gamma_{\mathrm{r}}}\omega_{\mathrm{a}}^2\sqrt{\frac{\gamma_{\mathrm{t}}C_0}{\hbar T\omega_{\mathrm{s}}}}\times\\ \times\left(\frac{\hat{V}_{\mathrm{R2}}\left[\Omega_k-\omega_{\mathrm{s}}\right]-\hat{V}_{\mathrm{R1}}\left[\Omega_k-\omega_{\mathrm{s}}\right]}{-\omega_{\mathrm{a}}^2+\left(\Omega_k-\omega_{\mathrm{s}}\right)\left(i\gamma_{\mathrm{l}}+\Omega_k-\omega_{\mathrm{s}}\right)}-\frac{\hat{V}_{\mathrm{R2}}\left[\Omega_k+\omega_{\mathrm{s}}\right]-\hat{V}_{\mathrm{R1}}\left[\Omega_k+\omega_{\mathrm{s}}\right]}{-\omega_{\mathrm{a}}^2+\left(\Omega_k+\omega_{\mathrm{s}}\right)\left(i\gamma_{\mathrm{l}}+\Omega_k+\omega_{\mathrm{s}}\right)}\right),\end{aligned} \tag{2.52}$$

where we have defined the effective decay $\Gamma_{\mathrm{b}}(\Omega_k)$ and frequency shift $\omega_{\mathrm{b}}(\Omega_k)$, resulting from the electrical influence on the mechanical motion:

$$\begin{aligned}\Gamma_{\mathrm{b}}(\Omega_k)=\mathrm{Re}\Bigg\{&\frac{-4i\gamma_{\mathrm{t}}}{T\omega_{\mathrm{s}}}\left(\frac{\alpha g_1\omega_{\mathrm{a}}}{\gamma_{\mathrm{r}}+\gamma_{\mathrm{t}}}\right)^2\left(\frac{1}{-\omega_{\mathrm{a}}^2+(\Omega_k-\omega_{\mathrm{s}})(i\gamma_{\mathrm{l}}+\Omega_k-\omega_{\mathrm{s}})}\right.\\ &\left.+\frac{1}{-\omega_{\mathrm{a}}^2+(\Omega_k+\omega_{\mathrm{s}})(i\gamma_{\mathrm{l}}+\Omega_k+\omega_{\mathrm{s}})}\right)\Bigg\},\end{aligned} \tag{2.53a}$$

$$\begin{aligned}\omega_{\mathrm{b}}(\Omega_k)=\mathrm{Im}\Bigg\{&\frac{-4i\gamma_{\mathrm{t}}}{T\omega_{\mathrm{s}}}\left(\frac{\alpha g_1\omega_{\mathrm{a}}}{\gamma_{\mathrm{r}}+\gamma_{\mathrm{t}}}\right)^2\left(\frac{1}{-\omega_{\mathrm{a}}^2+(\Omega_k-\omega_{\mathrm{s}})(i\gamma_{\mathrm{l}}+\Omega_k-\omega_{\mathrm{s}})}\right.\\ &\left.+\frac{1}{-\omega_{\mathrm{a}}^2+(\Omega_k+\omega_{\mathrm{s}})(i\gamma_{\mathrm{l}}+\Omega_k+\omega_{\mathrm{s}})}\right)\Bigg\}.\end{aligned} \tag{2.53b}$$

Note that, for deriving Eq. (2.52), we neglected the off resonant terms $\hat{b}[\Omega_k\pm 2\omega_{\mathrm{s}}]$, $\hat{b}^{\dagger}[\Omega_k\pm 2\omega_{\mathrm{s}}]$, and $\hat{b}^{\dagger}[\Omega_k]$ (we verify this approximation numerically below in Fig. 2.11). Moreover, the Fourier components of the noises are written in their most general form, meaning that Ω_k is now allowed to be negative, with the additional constraints $\hat{V}_{\mathrm{R1}}[\Omega_k]=\hat{V}_{\mathrm{R1}}^{\dagger}[-\Omega_k]$, and $\hat{V}_{\mathrm{R2}}[\Omega_k]=\hat{V}_{\mathrm{R2}}^{\dagger}[-\Omega_k]$.

In order to have an analytical expression for $n_{\mathrm{b}}(t)\equiv\langle\hat{n}_{\mathrm{b}}(t)\rangle$, we assume that the damping γ_{b} of the mechanical motion is much smaller than its own natural frequency ω_{m}. If $\gamma_{\mathrm{b}}\ll\omega_{\mathrm{m}}$, the set of frequencies contributing to $\hat{b}[\Omega_k]$ and $\hat{b}^{\dagger}[\Omega_k]$ will be located around ω_{m} and $-\omega_{\mathrm{m}}$ respectively. This, in turn, implies that we can substitute the effective damping $\Gamma_{\mathrm{b}}(\Omega_k)$ and shift $\omega_{\mathrm{b}}(\Omega_k)$ with the values taken at the relevant frequencies $\pm\omega_{\mathrm{m}}$. Defining the constant effective decay $\Gamma_{\mathrm{b}}=\Gamma_{\mathrm{b}}(\omega_{\mathrm{m}})=\Gamma_{\mathrm{b}}(-\omega_{\mathrm{m}})$ and frequency shift $\omega_{\mathrm{b}}=\omega_{\mathrm{b}}(\omega_{\mathrm{m}})=-\omega_{\mathrm{b}}(-\omega_{\mathrm{m}})$, we can rewrite Eq. (2.52) in the following way[4]:

$$\hat{b}\left[\Omega_k\right]\left(\frac{\gamma_\mathrm{b}+\Gamma_\mathrm{b}}{2}-i\left[\Omega_k-\omega_\mathrm{m}-\omega_\mathrm{b}\right]\right)=i\frac{x_\mathrm{z}}{\hbar}\hat{F}_\mathrm{b}\left[\Omega_k\right]+\frac{2g_1\alpha}{\gamma_\mathrm{t}+\gamma_\mathrm{r}}\omega_\mathrm{a}^2\sqrt{\frac{\gamma_\mathrm{t}C_0}{\hbar T\omega_\mathrm{s}}}\times$$
$$\times\left(\frac{\hat{V}_{\mathrm{R}2}\left[\Omega_k-\omega_\mathrm{s}\right]-\hat{V}_{\mathrm{R}1}\left[\Omega_k-\omega_\mathrm{s}\right]}{-\omega_\mathrm{a}^2+\left(\Omega_k-\omega_\mathrm{s}\right)\left(i\gamma_1+\Omega_k-\omega_\mathrm{s}\right)}-\frac{\hat{V}_{\mathrm{R}2}\left[\Omega_k+\omega_\mathrm{s}\right]-\hat{V}_{\mathrm{R}1}\left[\Omega_k+\omega_\mathrm{s}\right]}{-\omega_\mathrm{a}^2+\left(\Omega_k+\omega_\mathrm{s}\right)\left(i\gamma_1+\Omega_k+\omega_\mathrm{s}\right)}\right), \tag{2.54}$$

from which we can see that Γ_b affects the dynamics as an effective decay and ω_b serves as a frequency shift.

We can now take the Fourier series of Eq. (2.54), in order to go back to the time domain, and solve formally for $\hat{b}(t)$. Defining the noise operator $\hat{N}(t)=\hat{N}^\dagger(t)$ to be

$$\hat{N}(t)=\sum_{k=-\infty}^{\infty}\hat{N}\left[\Omega_k\right]\frac{e^{-i\Omega_k t}}{\sqrt{T}}, \tag{2.55a}$$

$$\hat{N}\left[\Omega_k\right]=\left(\frac{\hat{V}_{\mathrm{R}2}\left[\Omega_k-\omega_\mathrm{s}\right]-\hat{V}_{\mathrm{R}1}\left[\Omega_k-\omega_\mathrm{s}\right]}{-\omega_\mathrm{a}^2+\left(\Omega_k-\omega_\mathrm{s}\right)\left(i\gamma_1+\Omega_k-\omega_\mathrm{s}\right)}-\frac{\hat{V}_{\mathrm{R}2}\left[\Omega_k+\omega_\mathrm{s}\right]-\hat{V}_{\mathrm{R}1}\left[\Omega_k+\omega_\mathrm{s}\right]}{-\omega_\mathrm{a}^2+\left(\Omega_k+\omega_\mathrm{s}\right)\left(i\gamma_1+\Omega_k+\omega_\mathrm{s}\right)}\right), \tag{2.55b}$$

we obtain

$$\dot{\hat{b}}(t)=\hat{b}(t)\left(-i\left(\omega_\mathrm{m}+\omega_\mathrm{b}\right)-\frac{\gamma_\mathrm{b}+\Gamma_\mathrm{b}}{2}\right)+i\frac{x_\mathrm{z}}{\hbar}\hat{F}_\mathrm{b}(t)+\frac{2g_1\alpha}{\gamma_\mathrm{t}+\gamma_\mathrm{r}}\omega_\mathrm{a}^2\sqrt{\frac{\gamma_\mathrm{t}C_0}{T\omega_\mathrm{s}\hbar}}\hat{N}(t). \tag{2.56}$$

From Eq. (2.56) it is now possible to obtain the exact solution for $\hat{b}(t)$ as a function of the quantum noises $\hat{F}_\mathrm{b}(t)$ and $\hat{N}(t)$:

$$\hat{b}(t)=\hat{b}(0)e^{-\left[\frac{\gamma_\mathrm{b}+\Gamma_\mathrm{b}}{2}+i(\omega_\mathrm{m}+\omega_\mathrm{b})\right]t}+i\frac{x_\mathrm{z}}{\hbar}\int_0^t e^{-\left[\frac{\gamma_\mathrm{b}+\Gamma_\mathrm{b}}{2}+i(\omega_\mathrm{m}+\omega_\mathrm{b})\right](t-\tau_1)}\hat{F}_\mathrm{b}(\tau_1)d\tau_1$$
$$+\frac{2g_1\alpha}{\gamma_\mathrm{t}+\gamma_\mathrm{r}}\omega_\mathrm{a}^2\sqrt{\frac{\gamma_\mathrm{t}C_0}{T\omega_\mathrm{s}\hbar}}\int_0^t e^{-\left[\frac{\gamma_\mathrm{b}+\Gamma_\mathrm{b}}{2}+i(\omega_\mathrm{m}+\omega_\mathrm{b})\right](t-\tau_1)}\hat{N}(\tau_1)d\tau_1, \tag{2.57}$$

where $\hat{b}(0)$ is the annihilation operator at the initial time $t=0$. From here one can verify that the mechanical creation and annihilation operators satisfy the standard commutation relation, $\left[\hat{b}(t),\hat{b}^\dagger(t)\right]=1$.

With the above results, we can finally determine $n_\mathrm{b}(t)$ to be

$$n_\mathrm{b}(t)=n_\mathrm{b}(0)e^{-(\gamma_\mathrm{t}+\gamma_\mathrm{r})t}$$
$$+\frac{1}{2\hbar m\omega_\mathrm{m}}\int_0^t\int_0^t e^{-\frac{\gamma_\mathrm{b}+\Gamma_\mathrm{b}}{2}(2t-\tau_1-\tau_2)}e^{-i(\omega_\mathrm{m}+\omega_\mathrm{b})(\tau_1-\tau_2)}\left\langle\hat{F}_\mathrm{b}^\dagger(\tau_1)\hat{F}_\mathrm{b}(\tau_2)\right\rangle d\tau_1 d\tau_2$$
$$+4\frac{g_1^2|\alpha|^2\omega_\mathrm{a}^4}{(\gamma_\mathrm{t}+\gamma_\mathrm{r})^2}\frac{\gamma_\mathrm{r}C_0}{T\omega_\mathrm{s}\hbar}\int_0^t\int_0^t e^{-\frac{\gamma_\mathrm{b}+\Gamma_\mathrm{b}}{2}(2t-\tau_1-\tau_2)}e^{-i(\omega_\mathrm{m}+\omega_\mathrm{b})(\tau_1-\tau_2)}\left\langle\hat{N}(\tau_1)\hat{N}(\tau_2)\right\rangle d\tau_1 d\tau_2. \tag{2.58}$$

At this stage, the whole problem is reduced to computing the variances of the mechanical noise $\left\langle\hat{F}_\mathrm{b}^\dagger(\tau_1)\hat{F}_\mathrm{b}(\tau_2)\right\rangle$ and the electric fields $\left\langle\hat{N}(\tau_1)\hat{N}(\tau_2)\right\rangle$. As a consequence of our assumption $\gamma_\mathrm{b}\ll\omega_\mathrm{m}$, we can neglect off–resonant contributions in $\left\langle\hat{F}_\mathrm{b}^\dagger(\tau_1)\hat{F}_\mathrm{b}(\tau_2)\right\rangle$ and write it as

$$\left\langle\hat{F}_\mathrm{b}^\dagger(\tau_1)\hat{F}_\mathrm{b}(\tau_2)\right\rangle\simeq 2\hbar m\omega_\mathrm{m}\gamma_\mathrm{b}\bar{n}_\mathrm{m}\delta(\tau_2-\tau_1). \tag{2.59}$$

---

[4] To be precise, the effective decay Γ_b is defined at the frequency $\omega_m+\omega_b(\omega_m)$. In practice, there is little difference between the two definitions, but formally the one presented here is more correct.

The determination of the other variance, $\left\langle \hat{N}(\tau_1)\hat{N}(\tau_2)\right\rangle$, is more involved. In general, taking the definition of $\hat{N}(t)$ in Eqs. (2.55) and substituting it into expression for the correlator, one encounters a number of products of the form

$$\frac{\left\langle \hat{V}_{Ri}\left[\Omega_h\right]\hat{V}_{Rj}\left[\Omega_m\right]\right\rangle e^{-i\Omega_h t}e^{-i\Omega_m t}}{\mathrm{Den}\left(\Omega_h,\Omega_m\right)}, \tag{2.60}$$

where $i,j = 1,2$, and Ω_h, Ω_m are generic Fourier variables. The denominators $\mathrm{Den}\left(\Omega_h,\Omega_m\right)$ can be determined from Eq. (2.55b). Considering that

$$\left\langle \hat{V}_{Ri}\left[\Omega_h\right]\hat{V}_{Rj}\left[\Omega_m\right]\right\rangle = 0, \quad \forall i \neq j, \tag{2.61a}$$

$$\begin{aligned}\left\langle \hat{V}_{Ri}\left[\Omega_h\right]\hat{V}_{Ri}\left[\Omega_m\right]\right\rangle =& \frac{\hbar\Omega_h R}{2}\bar{n}_{\mathrm{e}}(\Omega_h,T_{\mathrm{e}})\delta\left(\Omega_h+\Omega_m\right)\theta\left(-\Omega_h\right)\\ &+\frac{\hbar\Omega_h R}{2}\left[\bar{n}_{\mathrm{e}}(\Omega_h,T_{\mathrm{e}})+1\right]\delta\left(\Omega_h+\Omega_m\right)\theta\left(\Omega_h\right),\end{aligned} \tag{2.61b}$$

with $\bar{n}_{\mathrm{e}}(\Omega_h,T_{\mathrm{e}})$ being the occupation number of the electrical reservoir at the considered frequency Ω_h and temperature T_{e}, we get

$$\begin{aligned}\left\langle \hat{N}(\tau_1)\hat{N}(\tau_2)\right\rangle =& \frac{(\omega_{\mathrm{s}}-\omega_{\mathrm{m}})\hbar R\bar{n}_{\mathrm{e}}\left(\omega_{\mathrm{s}}-\omega_{\mathrm{m}},T_{\mathrm{e}}\right)\delta\left(\tau_2-\tau_1\right)}{\omega_{\mathrm{a}}^4-2\omega_{\mathrm{a}}^2\left(\omega_{\mathrm{m}}-\omega_{\mathrm{s}}\right)^2+\left(\omega_{\mathrm{m}}-\omega_{\mathrm{s}}\right)^2\left(\gamma_1^2+\left(\omega_{\mathrm{m}}-\omega_{\mathrm{s}}\right)^2\right)}\\ &+\frac{(\omega_{\mathrm{s}}+\omega_{\mathrm{m}})\hbar R\bar{n}_{\mathrm{e}}\left(\omega_{\mathrm{s}}+\omega_{\mathrm{m}},T_{\mathrm{e}}\right)\delta\left(\tau_2-\tau_1\right)}{\omega_{\mathrm{a}}^4-2\omega_{\mathrm{a}}^2\left(\omega_{\mathrm{m}}+\omega_{\mathrm{s}}\right)^2+\left(\omega_{\mathrm{m}}+\omega_{\mathrm{s}}\right)^2\left(\gamma_1^2+\left(\omega_{\mathrm{m}}+\omega_{\mathrm{s}}\right)^2\right)}.\end{aligned} \tag{2.62}$$

We have here assumed both resistances R to be at the same temperature T_{e}, and neglected fast–oscillating contributions to $\left\langle \hat{N}(\tau_1)\hat{N}(\tau_2)\right\rangle$. In Eq. (2.61b), we also denoted the Heaviside step function with the letter θ.

With this last result, we are finally able to determine the time evolution for the average phonon number operator $n_{\mathrm{b}}(t)$. In fact, using equations (2.59) and (2.62), it is possible to calculate the integrals in Eq. (2.58) and therefore obtain a clear analytical expression for $n_{\mathrm{b}}(t)$. In its most general form, the expression is rather involved. For simplicity, we restrict ourselves to a reasonable approximation that allows us to better understand the final result. Considering the limit $\omega_{\mathrm{a}} \gg \omega_{\mathrm{s}} \gg \omega_{\mathrm{m}}$, from Eqs. (2.53a) and (2.53b) with $\Omega_k \to \omega_{\mathrm{m}}$, we can rewrite the effective decay Γ_{b} and the frequency shift ω_{b} to be

$$\Gamma_{\mathrm{b}} = \frac{8g_1^2|\alpha|^2\gamma_1\gamma_{\mathrm{t}}\omega_{\mathrm{m}}}{T\left(\gamma_{\mathrm{t}}+\gamma_{\mathrm{r}}\right)^2\omega_{\mathrm{s}}\omega_{\mathrm{a}}^2}, \tag{2.63a}$$

$$\omega_{\mathrm{b}} = -\frac{4g_1^2|\alpha|^2\gamma_{\mathrm{t}}}{T\left(\gamma_{\mathrm{t}}+\gamma_{\mathrm{r}}\right)^2\omega_{\mathrm{s}}}. \tag{2.63b}$$

From now on, referring to Γ_{b} and ω_{b}, we implicitly consider the form given in these last two equations. Note, however, that Eq. (2.53a) describes the damping due to the difference in sideband strengths for a mode at frequency ω_{a} driven at frequency ω_{s}. In the limit where ω_{a} is large, this induced damping is very small. The shift of Eq. (2.53b) may be sizeable, but merely leads to a new mechanical resonance frequency, which is not important for the present discussion. Furthermore, as a consequence of $\omega_{\mathrm{s}} \gg \omega_{\mathrm{m}}$, we assume that $\bar{n}_{\mathrm{e}}(\omega_{\mathrm{s}}-\omega_{\mathrm{m}},T_{\mathrm{e}})$ and $\bar{n}_{\mathrm{e}}(\omega_{\mathrm{s}}+\omega_{\mathrm{m}},T_{\mathrm{e}})$ are approximatively equal in Eq. (2.62), such that

$$\bar{n}_{\mathrm{e}}(\omega_{\mathrm{s}} \pm \omega_{\mathrm{m}}, T_{\mathrm{e}}) \simeq \bar{n}_{\mathrm{e}}(\omega_{\mathrm{s}}, T_{\mathrm{e}}) \equiv \bar{n}_{\mathrm{e}}. \tag{2.64}$$

Putting all these results together we can finally derive $n_{\mathrm{b}}(t)$ to be

$$\begin{aligned} n_{\mathrm{b}}(t) = & n_{\mathrm{b}}(0)e^{-(\gamma_{\mathrm{b}}+\Gamma_{\mathrm{b}})t} + \frac{\gamma_{\mathrm{b}}}{\gamma_{\mathrm{b}}+\Gamma_{\mathrm{b}}}\bar{n}_{\mathrm{m}}\left(1-e^{-(\gamma_{\mathrm{b}}+\Gamma_{\mathrm{b}})t}\right) + \\ & \frac{\Gamma_{\mathrm{b}}}{\gamma_{\mathrm{b}}+\Gamma_{\mathrm{b}}}\frac{\omega_{\mathrm{s}}}{\omega_{\mathrm{m}}}\left(\bar{n}_{\mathrm{e}}+\frac{1}{2}\right)\left(1-e^{-(\gamma_{\mathrm{b}}+\Gamma_{\mathrm{b}})t}\right). \end{aligned} \tag{2.65}$$

As a conclusive part of this discussion, let us determine Δn_{b}. Recalling that Δn_{b} is the change in the phonon number for the membrane initially cooled in its ground state, we get

$$\Delta n_{\mathrm{b}} = \gamma_{\mathrm{b}}\bar{n}_{\mathrm{m}}T + \frac{\omega_{\mathrm{s}}}{\omega_{\mathrm{m}}}\Gamma_{\mathrm{b}}\left(\bar{n}_{\mathrm{e}}+\frac{1}{2}\right)T, \tag{2.66}$$

where we truncated the expansion at first order in T. This is the parameter used as denominator in $\lambda_{\mathrm{b}} = D^2/\Delta n_{\mathrm{b}}$, presented in Eq. (2.5a) neglecting the contribution from the mechanical reservoir.

The parameter Δn_{b} derived above takes into account *only* the heating induced by the redistribution of charges on the capacitor. Asymmetries are well described analytically by considering a linear coupling δg_1 and capacitance δC such that $C^{-1}(\pm\hat{x}) \propto (C_0 \pm \delta C)^{-1} \pm (g_1 \pm \delta g_1)\hat{x} + g_2\hat{n}_{\mathrm{b}}$. These are the only asymmetries directly affecting the electromechanical coupling; other ones only enter as higher order perturbation, as we will see later in subsection 2.2.2. In this case we can find an *overall* residual linear coupling $g_{\mathrm{r}} = \frac{1}{2}C_0 x_{\mathrm{z}}\omega_{\mathrm{s}}\partial_x\left[C(x)+C(-x)\right]^{-1} > 0$ of the membrane equal to

$$g_{\mathrm{r}} = \delta g_1 + 2\frac{g_1\delta C}{C_0} + \frac{\delta g_1 \delta C^2}{C_0^2}. \tag{2.67}$$

Under the assumption that the parasitic elements R and L of the circuit are smaller than the non-parasitic ones R_0 and L_0, we can neglect the coupling to the antisymmetric mode to lowest order (this mode is far off resonant, while the symmetric one is resonant). The heating is then dominated by the residual linear coupling g_{r}, similarly to the situation encountered above in subsection 2.2.1. We can thus use the result in Eq. (2.34) obtained for the *RLC* circuit to identify the contribution to the heating:

$$n_{\mathrm{b}}(t) = \frac{\tilde{\Gamma}_{\mathrm{b}}}{\gamma_{\mathrm{b}}+\Gamma_{\mathrm{b}}}(1+2\bar{n}_{\mathrm{e}})\left(1-e^{-(\gamma_{\mathrm{b}}+\Gamma_{\mathrm{b}})t}\right). \tag{2.68}$$

Here, $\tilde{\Gamma}_{\mathrm{b}}$ has been defined from Γ_{b} in Eq. (2.35) by substituting g_1 with g_{r}:

$$\tilde{\Gamma}_{\mathrm{b}} = \frac{4g_{\mathrm{r}}^2|\alpha|^2\gamma_{\mathrm{t}}}{T(\gamma_{\mathrm{t}}+\gamma_{\mathrm{r}})\left[(\gamma_{\mathrm{t}}+\gamma_{\mathrm{r}})^2+4\omega_{\mathrm{m}}^2\right]}. \tag{2.69}$$

From Eq. (2.68) we can determine Δn_{b},

$$\Delta n_{\mathrm{b}} = \tilde{\Gamma}_{\mathrm{b}}(1+2\bar{n}_{\mathrm{e}})T, \tag{2.70}$$

being the denominator of the parameter $\lambda_{\mathrm{p}} = D^2/\Delta n_{\mathrm{b}}$ presented in Eq. (2.5b) for $\delta C \to 0$.

Putting together Eqs. (2.65) and (2.68), we can find the time evolution of the average phonon number $n_{\mathrm{b}}(t)$, taking into account all sources of heating:

$$n_{\mathrm{b}}(t) = n_{\mathrm{b}}(0)e^{-(\gamma_{\mathrm{b}}+\Gamma_{\mathrm{b}})t} + \left[\gamma_{\mathrm{b}}\bar{n}_{\mathrm{m}} + \left(\Gamma_{\mathrm{b}}\frac{\omega_{\mathrm{s}}}{2\omega_{\mathrm{m}}} + \tilde{\Gamma}_{\mathrm{b}}\right)(1+2\bar{n}_{\mathrm{e}})\right]\frac{1-e^{-(\gamma_{\mathrm{b}}+\Gamma_{\mathrm{b}})t}}{\gamma_{\mathrm{b}}+\Gamma_{\mathrm{b}}}. \tag{2.71}$$

This result will be supported by our simulations, presented below.

Heating simulation

In this subsection we present two methods for simulating the membrane heating, described by $n_{\mathrm{b}}(t)$. For the 'double arm' circuit in Fig. 2.9 we cannot employ the wave function Monte–Carlo approach [93] that was used for Fig. 2.8. Quantum jump simulations apply to Markovian reservoirs, and thereby assume that there is the same number of thermal photons for all frequencies. In our case, there is a big difference in the resonance frequencies of the symmetric ω_{s} and antisymmetric ω_{a} electrical modes. Therefore, we need to address the frequency dependence of the reservoir occupation. At a given temperature T_{e} of the electrical reservoirs, the antisymmetric mode will come to equilibrium with $\bar{n}_{\mathrm{e}}(\omega_{\mathrm{a}}, T_{\mathrm{e}}) = [\exp(\hbar\omega_{\mathrm{a}}/k_{\mathrm{B}}T_{\mathrm{e}}) - 1]^{-1}$ photons at frequency ω_{a}. On the other hand, the coupling between the mechanical oscillator and the antisymmetric field is mediated by the driving, which is resonant with the symmetric mode. Hence, the membrane couples to a reservoir containing $\bar{n}_{\mathrm{e}}(\omega_{\mathrm{s}}, T_{\mathrm{e}}) \gg \bar{n}_{\mathrm{e}}(\omega_{\mathrm{a}}, T_{\mathrm{e}})$ photons, as indicated in Eq. (2.65). Therefore, more advanced methods are required for simulating the present situation.

We will investigate the approximations taken for deriving Eq. (2.71) on two different levels. First, we consider Eqs. (2.51) and solve them in the Fourier domain, keeping the off-resonant terms that have been ignored in the derivation of Eq. (2.65) above. Second, we allow for any possible deviation from the balanced circuit in Fig. 2.9, by introducing unbalanced parasitic resistances R_1 and R_2, inductances L_1 and L_2, rest capacitances C_1 and C_2, and linear couplings $g_1 + \delta g_1$ and $g_1 - \delta g_1$. In the following, since we are interested in the time evolution of the mechanical subsystem for times longer than T, we will explicitly consider a time variable $\tau > T$ in the Fourier expansion of Eq. (2.15)

Let us start our analysis by rewriting Eqs. (2.51) with the creation $\hat{a}^\dagger$ and annihilation $\hat{a}$ operators for the electrical charge $\hat{Q}_{\mathrm{a}}$ and flux $\hat{\Phi}_{\mathrm{a}}$:

$$\begin{aligned}\hat{a}[\Omega_k]\left(-i\Omega_k - i\omega_{\mathrm{a}} + \frac{\gamma_{\mathrm{l}}}{2}\right) = \frac{\gamma_{\mathrm{l}}}{2}\hat{a}^\dagger[\Omega_k] - i\frac{g_1\alpha}{\gamma_{\mathrm{r}}+\gamma_{\mathrm{t}}}\sqrt{\frac{\gamma_{\mathrm{t}}\omega_{\mathrm{a}}}{T\omega_{\mathrm{s}}}}\Big(\hat{b}[\Omega_k - \omega_{\mathrm{s}}] + \hat{b}^\dagger[\Omega_k - \omega_{\mathrm{s}}] \\ - \hat{b}[\Omega_k + \omega_{\mathrm{s}}] - \hat{b}^\dagger[\Omega_k + \omega_{\mathrm{s}}]\Big) + i\sqrt{\frac{C_0\omega_{\mathrm{a}}}{\hbar}}\left(\hat{V}_{\mathrm{R2}}[\Omega_k] - \hat{V}_{\mathrm{R1}}[\Omega_k]\right) + \frac{\hat{a}(t=0)}{\sqrt{\tau}} - \frac{\hat{a}(t=\tau)}{\sqrt{\tau}},\end{aligned} \tag{2.72a}$$

$$\begin{aligned}\hat{b}[\Omega_k]\left(-i\Omega_k - i\omega_{\mathrm{m}} + \frac{\gamma_{\mathrm{b}}}{2}\right) = -i\frac{g_1\alpha}{\gamma_{\mathrm{r}}+\gamma_{\mathrm{t}}}\sqrt{\frac{\gamma_{\mathrm{t}}\omega_{\mathrm{a}}}{T\omega_{\mathrm{s}}}}\Big(\hat{a}[\Omega_k - \omega_{\mathrm{s}}] + \hat{a}^\dagger[\Omega_k - \omega_{\mathrm{s}}] \\ - \hat{a}[\Omega_k + \omega_{\mathrm{s}}] - \hat{a}^\dagger[\Omega_k + \omega_{\mathrm{s}}]\Big) + i\frac{x_{\mathrm{z}}}{\hbar}\hat{F}_{\mathrm{b}}[\Omega_k] + \frac{\hat{b}(t=0)}{\sqrt{\tau}} - \frac{\hat{b}(t=\tau)}{\sqrt{\tau}},\end{aligned} \tag{2.72b}$$

where $\hat{Q}_{\mathrm{a}} = \sqrt{\hbar C_0\omega_{\mathrm{a}}}(\hat{a} + \hat{a}^\dagger)/2$ and $\hat{\Phi}_{\mathrm{a}} = i\sqrt{\hbar/(C_0\omega_{\mathrm{a}})}(\hat{a}^\dagger - \hat{a})$. Note that in Eqs. (2.72) we have ignored g_2 contributions ($g_2 \ll g_1$), and added boundary terms, that are required to describe non–periodic dynamics in the Fourier series. Without those, we would obtain the steady state evolution, that cannot capture the thermalisation from the ground or any other state than the equilibrium. The additional terms can be adjusted to represent the desired initial state.

In subsection 2.2.2 we truncated the Fourier series by keeping only the terms resonant with the mechanical frequency ω_{m}. Instead, we will now include additional terms at frequencies centred around $\pm\omega_{\mathrm{m}}$,

$$\begin{aligned}\hat{O}(t) = \sum_{k=-N_j}^{N_j} \sum_{l=-N_f}^{N_f} \hat{O}\left[\omega_{\mathrm{m}} + k\omega_{\mathrm{s}} + l\frac{2\pi}{\tau}\right] \frac{e^{-i\left(\omega_{\mathrm{m}}+k\omega_{\mathrm{s}}+l\frac{2\pi}{\tau}\right)}}{\sqrt{\tau}} \\ + \hat{O}\left[-\omega_{\mathrm{m}} - k\omega_{\mathrm{s}} - l\frac{2\pi}{\tau}\right] \frac{e^{i\left(\omega_{\mathrm{m}}+k\omega_{\mathrm{s}}+l\frac{2\pi}{\tau}\right)}}{\sqrt{\tau}},\end{aligned} \tag{2.73}$$

where $\hat{O}$ can be any operator $\hat{a}^{(\dagger)}$ or $\hat{b}^{(\dagger)}$, and k, l are integers corresponding to the expansion. In Eq. (2.73), the parameter N_j indicates how many sidebands we consider, while N_f is related with the convergence of the Fourier series. By setting $N_j = 0$, we are assuming that the mechanical and electrical subsystems are completely decoupled, while $N_j = 2$ is the case studied above analytically. Corrections are given for $N_j > 2$. An example of the considered frequencies is illustrated in Fig. 2.10 for $N_j = 2$ and $N_f = 4$. The Fourier components $\hat{a}\left[\pm\left(\omega_{\mathrm{m}} + k\omega_{\mathrm{s}} + l\frac{2\pi}{\tau}\right)\right]$ and $\hat{b}\left[\pm\left(\omega_{\mathrm{m}} + k\omega_{\mathrm{s}} + l\frac{2\pi}{\tau}\right)\right]$ are then derived from the set of coupled linear equations (2.72), that can be solved efficiently using the matrix notation. A comparison between the result of Eq. (2.65) and the so–derived simulations is presented in Fig. 2.11. In the left plot we present $T_{1/2}$ for different values of the linear coupling g_1. Here, $T_{1/2}$ is the time for which the average mechanical occupation is half the one of the steady state $n_{\mathrm{b}}(t \to \infty)$. In the right plot, it is possible to see the g_1–dependence of the mechanical steady state population. As it is possible to see, the simulations converge to the analytical curve of Eq. (2.65) independently from the parameter N_j. This means that off-resonant terms do not play a major role, and that the approximations taken for deriving Eq. (2.65) are appropriate. The small discrepancy between analytical and simulated results is dominated by a poor convergence of the Fourier series. By taking bigger N_f, this discrepancy would be eventually removed.

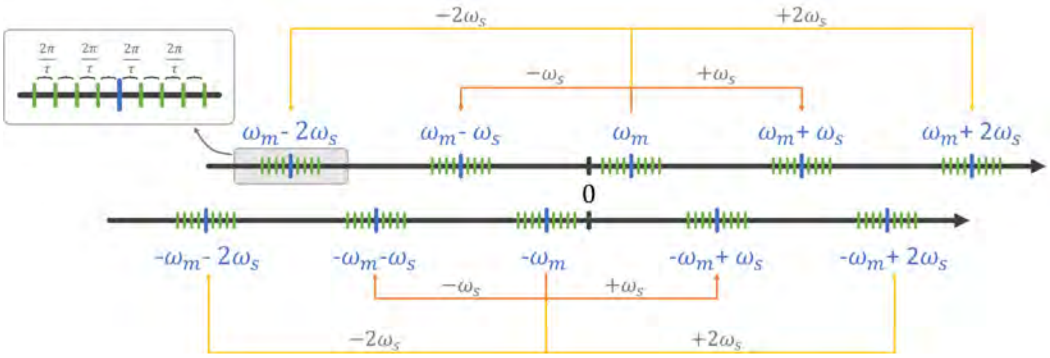

FIGURE 2.10: Example for a possible set of relevant frequencies in the truncated Fourier series of Eq. (2.73). In this particular case, we choose $N_j = 2$ and $N_f = 4$. In the **upper arrow** the frequencies obtained starting from ω_{m}, in the **lower arrow** from $-\omega_{\mathrm{m}}$.

In the second part of this subsection we simulate the electromechanical system presented in Fig. 2.9, allowing all the parasitic elements to differ between the two arms. In particular, we introduce deviations for resistances $R \to R \pm \delta R$, inductances

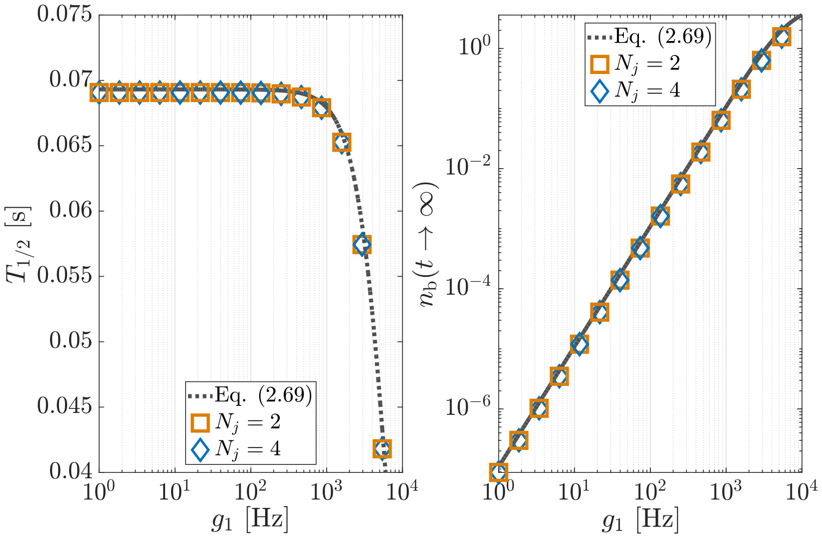

FIGURE 2.11: Comparison between Eq. (2.65) and simulations. In the **left plot**, we show $T_{1/2}$ versus the linear coupling g_1, with $T_{1/2}$ defined by the relation $n_b(T_{1/2}) = n_b(t \to \infty)/2$. In the **right plot**, the average mechanical steady state population $n_b(t \to \infty)$ is presented, as a function of g_1. Dotted lines are the analytical predictions obtained from Eq. (2.65). Red squares and blue diamonds come from simulations. The first one corresponds to the case where we allow for only one sideband ($N_j = 2$), and the second for two ($N_j = 4$). As it is possible to see, two–sidebands corrections are negligible. We assumed $L/L_0 = 10^{-4}$, $R/Z_{\text{out}} = 0.1$, $\omega_s = (2\pi)3$ GHz, $\omega_m = (2\pi)314$ MHz, $\gamma_t \simeq \gamma_r = (2\pi)100$ kHz, $\gamma_b = (2\pi)10$ Hz, $|\alpha|^2/\tau = 10^{12}$ s^{-1} and $\bar{n}_e = \bar{n}_m = 0^5$. Here, τ is the arbitrary time of the Fourier series in Eq. (2.15).

$L \to L \pm \delta L$, bare capacitances $C_0 \to C_0 \pm \delta C$, and the linear couplings $g_1 \to g_1 \pm \delta g_1$ in the left and right arms. Once we have done this, following the standard approach presented above we can derive the equations of motion of our electromechanical setup to be:

$$\dot{\hat{Q}}_{\mathrm{a}} = \frac{\hat{\Phi}_{\mathrm{a}}}{2L} + \frac{\delta L^2 \hat{\Phi}_{\mathrm{a}} - 2L\delta L \hat{\Phi}_{\mathrm{s}}}{2L\left(L^2 + 2LL_0 - \delta L^2\right)}, \tag{2.74a}$$

$$\begin{aligned}\dot{\hat{\Phi}}_{\mathrm{a}} =& -\frac{2\hat{Q}_{\mathrm{a}}}{C_0} - \frac{g_1}{C_0\omega_{\mathrm{s}}}\hat{Q}_{\mathrm{s}}\left(\hat{b} + \hat{b}^\dagger\right) - \frac{2g_2}{C_0\omega_{\mathrm{s}}}\hat{Q}_{\mathrm{a}}\hat{b}^\dagger\hat{b} - \gamma_1\hat{\Phi}_{\mathrm{a}} + 2\left(\hat{V}_{\mathrm{R2}} - \hat{V}_{\mathrm{R1}}\right) - \frac{2\delta C^2\hat{Q}_{\mathrm{a}}}{C_0\left(C_0^2 - \delta C^2\right)} \\ &+ \frac{\delta C\hat{Q}_{\mathrm{s}}}{C_0^2 - \delta C^2} - \frac{2\delta g_1}{C_0\omega_{\mathrm{s}}}\hat{Q}_{\mathrm{a}}\left(\hat{b} + \hat{b}^\dagger\right) + \frac{\delta L(-R\delta L + L\delta R)}{L\left(L^2 + 2LL_0 - \delta L^2\right)}\hat{\Phi}_{\mathrm{a}} + \frac{2R\delta L - 2L\delta R}{L^2 + 2LL_0 - \delta L^2}\hat{\Phi}_{\mathrm{s}},\end{aligned} \tag{2.74b}$$

$$\dot{\hat{Q}}_{\mathrm{s}} = \frac{2\hat{\Phi}_{\mathrm{s}}}{L + 2L_0} - \frac{\delta L\hat{\Phi}_{\mathrm{a}}}{\left(L^2 + 2LL_0 - 2\delta L^2\right)} + \frac{2\delta L^2\hat{\Phi}_{\mathrm{s}}}{\left(L + 2L_0\right)\left(L^2 + 2LL_0 - 2\delta L^2\right)}, \tag{2.74c}$$

$$\begin{aligned}\dot{\hat{\Phi}}_{\mathrm{s}} =& -\frac{\hat{Q}_{\mathrm{s}}}{2C_0} - \frac{g_1}{C_0\omega_{\mathrm{s}}}\hat{Q}_{\mathrm{a}}\left(\hat{b} + \hat{b}^\dagger\right) - \frac{2g_2}{C_0\omega_{\mathrm{s}}}\hat{Q}_{\mathrm{s}}\hat{b}^\dagger\hat{b} - (\gamma_{\mathrm{r}} + \gamma_{\mathrm{t}})\hat{\Phi}_{\mathrm{s}} + 2\left(\hat{V}_{\mathrm{in}} + \hat{V}_{\mathrm{R0}}\right) + \hat{V}_{\mathrm{R1}} + \hat{V}_{\mathrm{R2}} \\ &+ \frac{\delta C\hat{Q}_{\mathrm{a}}}{C_0^2 - \delta C^2} - \frac{\delta C^2\hat{Q}_{\mathrm{s}}}{2C_0\left(C_0^2 - \delta C^2\right)} - \frac{\delta g_1}{2C_0\omega_{\mathrm{s}}}\hat{Q}_{\mathrm{s}}\left(\hat{b} + \hat{b}^\dagger\right) + \frac{R\delta L + 2(R_0 + Z_{\mathrm{out}})\delta L - (L + 2L_0)\delta R}{2\left(L^2 + 2LL_0 - \delta L^2\right)}\hat{\Phi}_{\mathrm{a}} \\ &+ \frac{\delta L\left[\delta R(L + 2L_0) - \left(R + 2(R_0 + Z_{\mathrm{out}})\right)\delta L\right]}{\left(L + 2L_0\right)\left(L^2 + 2LL_0 - \delta L^2\right)}\hat{\Phi}_{\mathrm{s}},\end{aligned} \tag{2.74d}$$

$$\begin{aligned}\dot{\hat{b}} =& -i\omega_{\mathrm{m}}\hat{b} - i\frac{g_1}{\hbar C_0\omega_{\mathrm{s}}}\hat{Q}_{\mathrm{a}}\hat{Q}_{\mathrm{s}} - i\frac{g_2}{\hbar C_0\omega_{\mathrm{s}}}\left(\hat{b} + \hat{b}^\dagger\right)\left(\hat{Q}_{\mathrm{a}}^2 + \frac{\hat{Q}_{\mathrm{s}}^2}{4}\right) - \frac{\gamma_{\mathrm{b}}}{2}\hat{b} + i\frac{x_{\mathrm{z}}}{\hbar}\hat{F}_{\mathrm{b}} \\ &+ \frac{i\delta g_1}{\hbar C_0\omega_{\mathrm{s}}}\left(\hat{Q}_{\mathrm{a}}^2 + \frac{\hat{Q}_{\mathrm{s}}^2}{4}\right).\end{aligned} \tag{2.74e}$$

For simulating this set of equations we follow a similar approach to the one presented above, neglecting off–resonant terms that do not contribute substantially to the mechanical heating, and the quadratic coupling (since $g_2 \ll g_1$). In order to get a solution, we have linearised the symmetric and antisymmetric electrical fields, and the mechanical operators. As opposed to the previous investigations, now our simulations start at a specific time. We thus consider transient dynamics for the average mechanical operators, that we can set to have any initial value (generally zero, as for the ground state). Our simulations are thus performed with the mechanical average values being time dependent [91]. As it is possible to see from Fig. 2.3, the agreement between the analytical results and the simulations is excellent, as far as the asymmetries δR, δL and δC are small enough. The system is more susceptible to relative increase of δC as compared to δR and δL. This is because δR and δL are asymmetries of parasitic elements of the circuit, while δC affects the main (and only) capacitor. A non–vanishing value of δC directly affects the residual linear coupling g_{r} [see Eq. (2.67)] and thus has a larger influence, that is included in our analytical prediction of Eq. (2.71). Roughly speaking, whenever $\delta C/C$, $\delta R/R$ and $\delta L/L$ are smaller than 25%, the agreement between Eq. (2.71) and the simulations is very good.

In summary, we have tested the assumptions made in the derivation of our analytical results. We have proven with the Fourier analysis that off–resonant terms do not contribute significantly to the mechanical heating, while simulations of Eqs. (2.74) ensured that asymmetries play a secondary role in the electromechanical dynamics.

As a final comment, we note that the derivation of the parameter D^2 including asymmetries can be done analytically with the procedure introduced in subsections 2.2.1 and 2.2.2. We do not report the result here since including δR, δL and δC makes the expressions long and complicated. In principle, however, the parameter λ

for the most general antisymmetric setup can be derived analytically, with the simple expressions for λ_{b} and λ_{p} [given in Eqs. (2.5)] being valid for small asymmetries.

2.2.3 Measurement

The parameter λ specifies how suitable a specific experimental setup is for carrying out the QND detection. The outcome of an experimental run will, however, depend on the procedure used in the experiment. In this subsection, we consider the protocol presented in section 2.1.3 and illustrated in Fig. 2.12. We assume that the mechanical oscillator is prepared and continuously cooled to some average phonon number $\bar{n}_{\mathrm{m}}$ during the entire measurement sequence. We determine the best experimental parameter Δn_{b} to be used to maximize the visibility ξ for a given value of λ. Finally, we compare the analytical model with numerical simulations.

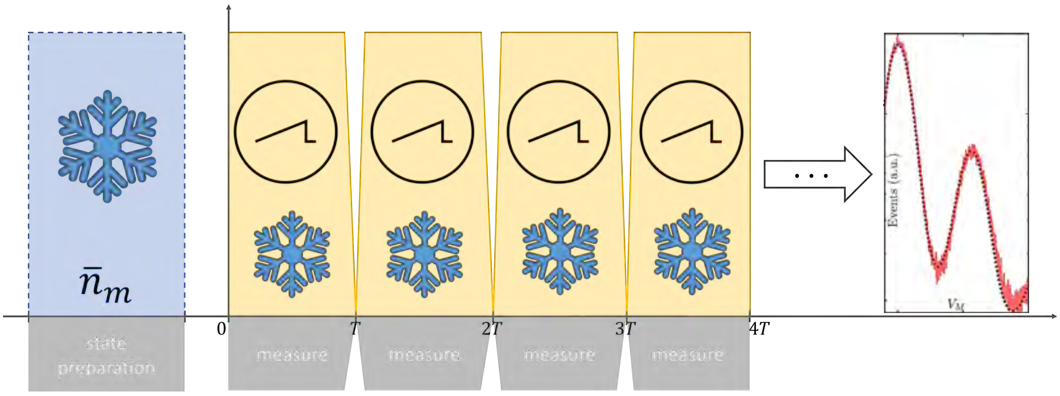

FIGURE 2.12: Considered measurement sequence. The mechanical state is cooled down to some average thermal phonon number $\bar{n}_{\mathrm{m}}$, and then measured several times, while keeping the cooling active.

First, we develop a model for the protocol presented in Fig. 2.12, where we only allow for a single jump during the measurement time T. After the state preparation, the membrane is in a mixture of the Fock states $\hat{\rho}_{\mathrm{in}} = \sum_i p_i |i\rangle\langle i|$, where $p_i = \bar{n}_{\mathrm{m}}^i / \left[1 + \bar{n}_{\mathrm{m}}\right]^{i+1}$ is the probability to be in the i–th state. When we start probing the system, the measurement outcome V_{M} follows a probability distribution that depends on three parameters: $\bar{n}_{\mathrm{m}}$, Δn_{b}, and D^2. $\bar{n}_{\mathrm{m}}$ determines the initial thermal state of the membrane, and fixes the probabilities p_i. Δn_{b} determines the rate at which the membrane jumps out the ground state, and can be used to calculate the probability, for each Fock state in $\hat{\rho}_{\mathrm{in}}$, to jump up or down. In particular, the ground state $|0\rangle$ has a probability $p_0\left(1 - \exp\left[-\Delta n_{\mathrm{b}}\right]\right)$ to jump up, while any other Fock state $|i\rangle$ has probabilities $p_i\left(1 - \exp\left[-(i+1)\Delta n_{\mathrm{b}}\right]\right)$ and $p_i\left(1 - \exp\left[-i\Delta n_{\mathrm{b}}(\bar{n}_{\mathrm{m}}^{-1} + 1)\right]\right)$ to jump up or down, respectively. Finally, D^2 sets the distance between measurement outcomes with different phonon occupations. Therefore, whenever the membrane remains in the same state during the whole duration T, the outcome V_{M} is a Gaussian distributed random number with average $n_{\mathrm{b}}d$ and variance $\sigma^2 = d^2/D^2$. If, on the other side, the mechanical state changes during the measurement, then V_{M} is again a Gaussian distributed random number with variance σ^2, but with an average value given by $T^{-1}\left[n_{\mathrm{b}}^{(i)} T_j d + n_{\mathrm{b}}^{(f)} (T - T_j) d\right]$. Here, T_j is the (uniformly distributed) random time at which the jump happens, and $n_{\mathrm{b}}^{(i)}$ and $n_{\mathrm{b}}^{(f)}$ are the phonon numbers before and after the jump. Therefore, knowing Δn_{b}, D^2 and $\bar{n}_{\mathrm{m}}$, the probability distribution function PDF of the outcomes V_{M} can be determined:

$$PDF(V_{\mathrm{M}}) = \lim_{N_{\mathrm{p}}\to\infty} \left\{ \sum_{i=0}^{N_{\mathrm{p}}} \frac{P_{\mathrm{p}}(i)}{\sqrt{2\pi}\sigma} e^{-\frac{(V_{\mathrm{M}}-id)^2}{2\sigma^2}} + \sum_{i=1}^{N_{\mathrm{p}}} \int_{(i-1)d}^{id} \frac{P_{\mathrm{r}}(i-1;1)}{\sqrt{2\pi}d\sigma} e^{-\frac{(V_{\mathrm{M}}-V)^2}{2\sigma^2}} dV \right\}, \tag{2.75}$$

where, we recall, $D = d/\sigma$, and $\sigma^2 = (\Delta V_{\mathrm{M}})^2$ is a scaling factor. In this last equation, $P_{\mathrm{p}}(i)$ is the probability for the mechanical state to remain in $|i\rangle$ for the whole measurement, while $P_{\mathrm{r}}(i-1;i)$ is the likelihood that either $|i-1\rangle$ jumps up or $|i\rangle$ jumps down. The parameter N_{p} is the size of the Hilbert space of the mechanical subsystem. Since we are interested in the peaks relative to $n_{\mathrm{b}} = 0$ and $n_{\mathrm{b}} = 1$, we can assume $N_{\mathrm{p}} = 1$ and thus rewrite (2.75) in the following form:

$$\begin{aligned} PDF(V_{\mathrm{M}}) \simeq & \sqrt{\frac{1}{2\pi\sigma^2}} \left(\frac{e^{-\frac{V_{\mathrm{M}}^2}{2\sigma^2} - \Delta n_{\mathrm{b}}}}{1+\bar{n}_{\mathrm{m}}} + \frac{e^{-\frac{(V_{\mathrm{M}}-d)^2}{2\sigma^2} - \Delta n_{\mathrm{b}}\left(3+\bar{n}_{\mathrm{m}}^{-1}\right)} \bar{n}_{\mathrm{m}}}{(1+\bar{n}_{\mathrm{m}})^2} \right) \\ & + \left[(1+\bar{n}_{\mathrm{m}})(1-e^{-\Delta n_{\mathrm{b}}}) + \bar{n}_{\mathrm{m}} \frac{1-e^{-\Delta n_{\mathrm{b}}(3+\bar{n}_{\mathrm{m}}^{-1})}}{1+e^{-\Delta n_{\mathrm{b}}(1-\bar{n}_{\mathrm{m}}^{-1})}} \right] \frac{\mathrm{Erf}\left(\frac{V_{\mathrm{M}}}{\sqrt{2}\sigma}\right) - \mathrm{Erf}\left(\frac{V_{\mathrm{M}}-d}{\sqrt{2}\sigma}\right)}{2d(1+\bar{n}_{\mathrm{m}})^2}, \end{aligned} \tag{2.76}$$

where $\mathrm{Erf}(\cdot)$ denotes the error function. From Eq. (2.76), we can derive an analytical expression for the visibility that depends on the mentioned parameters: $\xi\left(\bar{n}_{\mathrm{m}}, D^2, \Delta n_{\mathrm{b}}\right)$. Importantly, D^2 is a dummy parameter, since $\lambda = D^2/\Delta n_{\mathrm{b}}$. It follows that, for given λ and $\bar{n}_{\mathrm{m}}$, we can maximise $\xi\left(\bar{n}_{\mathrm{m}}, \lambda\Delta n_{\mathrm{b}}, \Delta n_{\mathrm{b}}\right)$ by tuning Δn_{b}. Using this model, we obtain the analytical expression for the optimal ξ in the limit of $\lambda \gg 1$, presented in Eq. (2.8). Note that tuning Δn_{b} can be done by adjusting the probe power and choosing an appropriate measurement time T.

To investigate the validity of the single jump approximation used above, we simulate the probability distribution function for the outcome V_{M} in a Monte–Carlo simulation. The results are presented in Fig. 2.13. In the simulation, we allow multiple jumps to happen by dividing the measurement time T into smaller segments, during which the mechanics is allowed to change. Similar to above, the outcome of the measurement can then be sampled from a Gaussian distribution of variance σ^2 and a mean determined by the average phonon number during the measurement. The hardly visible deviation between the analytical prediction and numerics in Fig. 2.13 comes from the single jump restriction, and can be eliminated by including the two–jumps events in the model. Note that, since the optimal Δn_{b} decreases for higher values of λ, the single jump approximation becomes more and more accurate with increasing λ. Secondly, for given λ and $\bar{n}_{\mathrm{m}}$, we can compare the analytical with the numerical maximum visibility ξ. The latter is determined using repeated Monte–Carlo simulations with different values for Δn_{b}, as shown in Fig. 2.14. Each point in such plot corresponds to a single simulation with given parameters λ, $\bar{n}_{\mathrm{m}}$ and Δn_{b}. The error bars are derived assuming Poissonian statistics in each bin of the histogram collecting the outcomes V_{M}. A polynomial fit is then used for determining the maximum visibility ξ, that is compared with the analytical prediction in Fig. 2.5 (2D plot; analytical corresponds to the red dotted line, numerical results are represented by blue circles).

As a final remark, it is important to say that the results of this section can easily be adapted to other experimental schemes [92]. For instance, it is possible to first cool down the mechanical motion to the ground state, and then let it thermalize while measuring several times. An advantage of this approach is that it reduces the probability of jumping down from the excited Fock states, since the cooling is

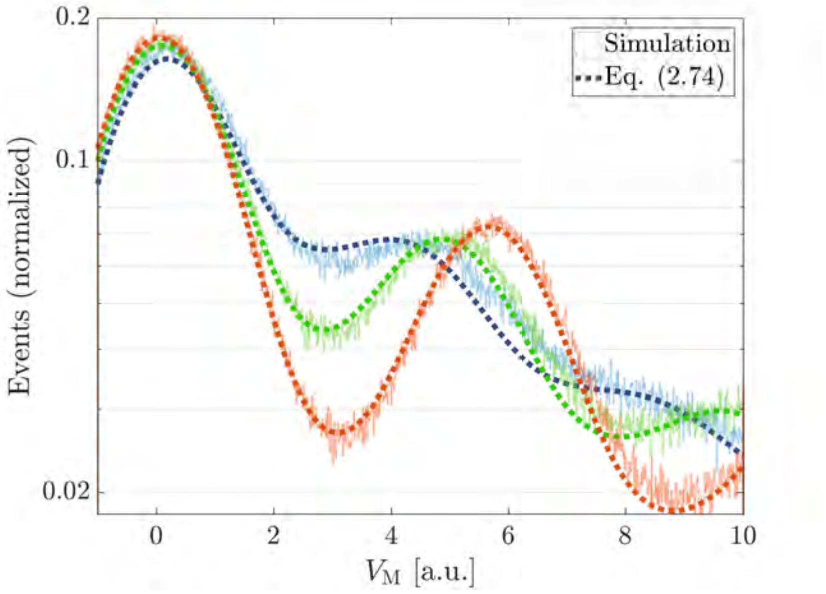

FIGURE 2.13: Analytical (dotted curves, Eq. (2.76)) and numerical (solid, noisy curves) probability distribution function for the experimental outcome V_{M}. We choose $\bar{n}_{\mathrm{m}} = 1$ and λ equal to 20 (blue), 100 (green) and 200 (red). The values of Δn_{b} that have been used were determined using the analytical maximization of the visibility ξ, with the cited λ and $\bar{n}_{\mathrm{m}}$ as free parameters.

absent. On the other hand, operating the experiment in a pulsed regime may add an extra degree of complexity, e.g., transient effects associated with the change in equilibrium position of the membrane when the fields are turned on.

2.2.4 Realistic experimental parameters

Here we study in more detail a possible experimental setup for our proposal, and the potential challenges that may arise pursuing the QND measurement of the phonon number. First, we present a simple derivation for determining the linear and quadratic electromechanical couplings g_1 and g_2 [86]. Then, we discuss the presence of a stray capacitance C_{s}, the main effect of which is to reduce these couplings. Finally, we analyse the feasibility of an experiment, considering aspects such as the intra-cavity photon number, the mechanical quality factor, the measurement time, and probe power. The parameters employed are the same as introduced in section 2.1.2: $\omega_{\mathrm{s}} = (2\pi)7$ GHz, $\omega_{\mathrm{m}} = (2\pi)80$ MHz, $\gamma_{\mathrm{r}} \simeq \gamma_{\mathrm{t}} = (2\pi)150$ kHz, $R = Z_{\mathrm{out}}/10$, $\bar{n}_{\mathrm{e}} = 0$, $g_{\mathrm{r}} = 10^{-2} g_1$ and $C_{\mathrm{s}} = 100 C_0$. The membrane is assumed to be 1 μm long and 0.3 μm wide, with a quality factor[6] $Q = 10^6$. We discuss the average occupation $\bar{n}_{\mathrm{m}}$ of the mechanical bath in the following.

The mechanical membrane is fixed along all its boundaries, such as in Fig. 2.1(a). A basis of modes describing its motion is thus $\{u_{i,j}(x,y)\}$, where

$$u_{i,j}(x,y) = \epsilon \sin\left(i\frac{\pi}{L}x\right) \sin\left(j\frac{\pi}{W}y\right) . \tag{2.77}$$

---

[6] For graphene membranes at cryogenic temperatures, quality factors between 10^5 and 10^6 have been showed in [84]. Here, the simple geometry used (monolayer sheet laid on circular support) let hope for future improvements in the quality factors of such devices.

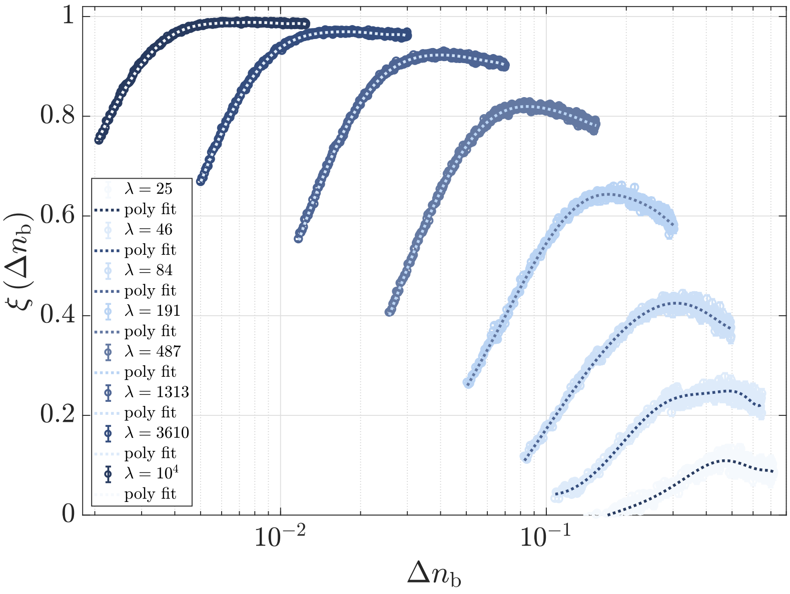

FIGURE 2.14: Visibility as a function of the parameter Δn_{b}, for different values of λ. The points are derived numerically using the Monte–Carlo method, and the dotted lines are polynomial fit. Notice that error bars are included, and have been determined assuming Poissonian statistics in each bin of the histogram collecting the outcomes V_{M}.

Here, L and W are the length and width of the membrane, respectively. The mode of interest has indices $i = 2$ and $j = 1$, and the constant ϵ fixes an effective gauge for the mass. By setting $\int_0^L \int_0^W \left|u_{i,j}(x,y)\right|^2 dxdy = 1$, we choose the gauge in which the so–called effective mass is the physical mass, and $\epsilon = 2$. Recalling that

$$g_1 = \frac{x_{\mathrm{z}}\omega_{\mathrm{s}}}{C_0}\frac{\partial C}{\partial \beta}\bigg|_{x=0}, \tag{2.78a}$$

$$g_2 = \frac{x_{\mathrm{z}}^2\omega_{\mathrm{s}}}{2C_0}\frac{\partial^2 C}{\partial \beta^2}\bigg|_{x=0}, \tag{2.78b}$$

the couplings can be determined once the derivatives are found. As discussed in Ref. [86], β describes the amplitude of the considered mode, and can be viewed as a canonical position. An approximate value of the derivatives in Eq. (2.78) is then

$$\frac{\partial^k C}{\partial \beta^k}\bigg|_{x=0} \simeq (-1)^k k! \frac{C_0}{d^k}\frac{2}{LW}\int_0^{L/2}\int_0^W u_{2,1}^k(x,y)dxdy, \tag{2.79}$$

where d is the distance separating the two capacitor's plates, and the integral is taken over *half* the membrane, for the reasons discussed in section 2.2.2. Using Eqs. (2.78) and (2.79), we can finally determine the values of g_1 and g_2 to be

$$g_1 = \frac{8}{\pi^2}\frac{x_{\mathrm{z}}\omega_{\mathrm{s}}}{d}, \tag{2.80a}$$

$$g_2 = \frac{x_{\mathrm{z}}^2\omega_{\mathrm{s}}}{d^2}. \tag{2.80b}$$

For the parameters introduced in section 2.1.2, we find $g_1 \simeq (2\pi)715$ kHz and $g_2 \simeq (2\pi)111$ Hz. Considering that we assumed an electrical damping $\gamma_{\mathrm{t}} = (2\pi)150$ kHz, it could seem that we reach the strong coupling regime $g_1 > \gamma_{\mathrm{t}}$. However, we have so far ignored stray capacitances, that are the main reason for which the strong coupling regime (and thus the phonon QND measurement) has never been accomplished in electromechanics. For such small geometries, the stray capacitance C_{s} always exceed the intrinsic capacitance C_0 by up to several orders of magnitude [84], and severely limits the attainable values of the linear and quadratic couplings [see Fig. 2.4(b)]. Looking at Eqs. (2.78), and considering that the stray capacitance does not affect the derivatives $\partial^k C/\partial\beta^k$, we replace the coupling constants by

$$g_1 \rightarrow \frac{C_0}{C_0 + C_{\mathrm{s}}} g_1, \tag{2.81a}$$

$$g_2 \rightarrow \frac{C_0}{C_0 + C_{\mathrm{s}}} g_2. \tag{2.81b}$$

For $C_{\mathrm{s}} = 100C_0$, we find $g_1 \simeq (2\pi)7$ kHz and $g_2 \simeq (2\pi)1$ Hz. This value of C_{s} is optimistic for geometries similar to the ones in Ref. [84, 85], where graphene sheets are laid on a substrate in such a way that the contact area between the two interfaces is very large. However, for a setup like the one described in Ref. [82], membranes of similar dimensions as the ones conjectured here are assembled onto small localized gates, dramatically reducing the stray capacitance. With this fabrication technique, a stray capacitance of 50 fF is obtained, for a membrane that is about two and a half times the size of the one conjectured here. In our case, this value for the stray capacitance would correspond to 376 times C_0, where $C_0 \simeq 0.13$ fF. Due to the smaller size of our membrane, we assume a reduction in the stray capacitance, such that we consider $C_{\mathrm{s}} = 100C_0$.

In our settings, reaching the strong coupling would require $C_{\mathrm{s}} < 3.8C_0$. In this regime, phonon QND detection could also be performed with the strategy proposed in [45]. With a large stray capacitance, however, we cannot accomplish such requirement, and investigate different approaches to QND detection. With the experimental parameter described above, we find $\lambda_{\mathrm{b}} = 105 \times Z_{\mathrm{out}}/R$ and $\lambda_{\mathrm{p}} = 0.014(g_1/g_{\mathrm{r}})^2$, regardless of the value of C_{s}. The highest quoted value $\lambda = 122$ is found assuming $g_{\mathrm{r}} = 10^{-2} g_1$ and $Z_{\mathrm{out}} = 10R$.

In the remainder of this section, we study the conditions under which the QND detection could be implemented, focusing on the incident power and the measurement time. First, we recall that the membrane's heating has several contributions. Two of them, denoted $\Delta n_{\mathrm{b}}^{(b)}$ and $\Delta n_{\mathrm{b}}^{(p)}$, are the ones identified in Eqs. (2.66) (rhs, second term) and (2.70), respectively. They describe the feedback of the electrical system on the mechanical motion, and are the denominators of the parameters λ_{b} and λ_{p} defined in Eqs. (2.5). The third contribution comes from the mechanical reservoir. Indicated with $\Delta n_{\mathrm{b}}^{(m)}$, this is given in Eq. (2.66) (rhs, first term), and is independent of the strength of the probing field. For determining the parameter λ, we have so far ignored $\Delta n_{\mathrm{b}}^{(m)}$, assuming that the measurement is fast enough. This is an excellent approximation, as far as $\Delta n_{\mathrm{b}}^{(m)} \ll \Delta n_{\mathrm{b}}^{(b)} + \Delta n_{\mathrm{b}}^{(p)}$. Below, we discuss the case in which there is a seizable contribution from the mechanical bath, and describe its effect on the QND detection of the phonon number.

Above we have seen that, for the considered experimental parameters, $\lambda = 122$, for which we find the optimal $\Delta n_{\mathrm{b}} = 0.21$. For $C_{\mathrm{s}} = 100C_0$, the total number of photons that we need to send within the measurement is $\alpha^2 \simeq 4.5 \cdot 10^{11}$ [see Eqs. (2.66) and (2.70)]. By sending these photons within a sufficiently short time, we can neglect the influence of the mechanical reservoir. To derive precise conditions for this, we define the effective temperature $\bar{N}_{\rm e}$ of the electrically induced reservoir:

$$\bar{N}_{\rm e} = \frac{\Delta n_{\rm b}^{(b)} + \Delta n_{\rm b}^{(p)}}{T(\gamma_{\rm b} + \Gamma_{\rm b})}. \tag{2.82}$$

This last equation is derived from Eq. (2.71), by sending the time t to infinity, and recalling the definitions of $\Delta n_{\rm b}^{(b)}$ and $\Delta n_{\rm b}^{(p)}$. $\bar{N}_{\rm e}$ is the average phonon number at which the membrane stabilizes in the absence of the mechanical reservoir. The condition $\Delta n_{\rm b}^{(m)} \ll \Delta n_{\rm b}^{(b)} + \Delta n_{\rm b}^{(p)}$, under which the mechanical bath can be neglected, can be rewritten as $\bar{n}_{\rm m} \ll \bar{N}_{\rm e}$. The measurement time T is thus a knob that allows us to adjust the relative weights of the mechanical reservoir and the electrical feedback on the membrane. For short measurement times, $\bar{N}_{\rm e}$ is increased, and this condition is easier to satisfy. As an example, if we choose $T = 0.4$ ms and $Q = 10^6$, we get $\bar{N}_{\rm e} = 1$, implying that the average occupation of the membrane's reservoir needs to be less than unity to neglect the mechanical reservoir. For our setup, this requires the temperature of the cryostat to be lower than 6 mK, a challenging task for current technology. On the other side, choosing $T = 0.04$ ms fixes $\bar{N}_{\rm e} = 10$, and the temperature for which $\bar{n}_{\rm m}$ becomes negligible is 40 mK, that has been already achieved in experiments involving graphene resonators [84]. Once the measurement time is chosen, and assuming the photon flux $|\tilde{\alpha}|^2 = |\alpha|^2/T$ to be constant, one can determine the probing power $P_{\rm in}$ and the average intracavity photon number $|\tilde{\alpha}|^2/\gamma_{\rm t}$. As an example, with $T = 0.4$ ms, $P_{\rm in}$ becomes 5.3 nW and $|\tilde{\alpha}|^2/\gamma_{\rm t} = 1.2 \cdot 10^9$. These parameters are highly dependent on the mechanical quality factor Q, and the stray capacitance, as investigated below in Fig.2.4(a).

Finally, we discuss the case in which the electrical heating is in equilibrium with the heating and damping of the mechanical reservoir. In that case, we need to renormalize λ by the total heating:

$$\lambda' = \frac{\Delta n_{\rm b}^{(b)} + \Delta n_{\rm b}^{(p)}}{\Delta n_{\rm b}^{(m)} + \Delta n_{\rm b}^{(b)} + \Delta n_{\rm b}^{(p)}}\lambda, \tag{2.83}$$

where λ contains both the terms $\lambda_{\rm b}$ and $\lambda_{\rm p}$.

Importantly, we can always make $\lambda' \simeq \lambda$ by increasing the driving strength and reducing the measurement time (thus decreasing $\Delta n_{\rm b}^{(m)} = \bar{n}_{\rm m}\gamma_{\rm b}T$). The parameter λ' substitutes λ in the description of the system. The mechanical bath thus reduces the quality of the phonon QND measurement, but the analysis above still applies, with λ' instead of λ. As an example, assume that the temperature is 14 mK [84]. Then, the average occupation of the membrane's reservoir is $\bar{n}_{\rm m} = 3$. We choose T such that the electrical heating is equal to the mechanical: $\bar{N}_{\rm e} = \bar{n}_{\rm m}$. Then $\lambda' = \lambda/2 = 61$ with the previous parameters. This value is well in the regime of good visibility ξ, and for this λ', the optimal value of the total heating is $\Delta n_{\rm b} = \Delta n_{\rm b}^{(m)} + \Delta n_{\rm b}^{(b)} + \Delta n_{\rm b}^{(p)} = 0.3$. Depending on the value of the mechanical quality factor Q and stray capacitance $C_{\rm s}$, we can then determine the required incident power and the intracavity photon number, as shown in Fig. 2.4. Since we assume $\Delta n_{\rm b}^{(m)} = \Delta n_{\rm b}/2$, the measurement time is $T = \Delta n_{\rm b}/(2\gamma_{\rm b}\bar{n}_{\rm m}) \simeq 0.05Q/\omega_{\rm m}$. For the parameters in the figure and a quality factor Q varying between 10^5 and 10^7, we find $T \in \left[10^{-5}, 10^{-3}\right]$ s.

2.3 Conclusions

We have revisited the challenge of performing phonon QND measurement. Employing symmetry to inhibit the linear coupling, the detrimental heating is suppressed while retaining the desired quadratic coupling. Contrary to the optomechanical case [78], the residual coupling to the antisymmetric mode is strongly suppressed by its higher frequency and reduced resistance. A particularly attractive feature of the current approach is that it is only sensitive to the ratio g_2/g_1, and not to their absolute values. Stray capacitances, which reduce the electromechanical couplings, can thus be compensated using stronger input fields.

These attractive features put QND detection within reach of presently available technology. A successful realization of a QND detection will not only represent a demonstration of genuine non-classical behaviour of mechanical systems, but also extend the interactions available in electro/opto–mechanics to non–Gaussian operations [94]. This will considerably expand the realm of effects that can be studied with these systems, and facilitate their application for quantum information processing [29].

The extensions of this work to the optomechanical case is considered in chapter 3. The electromechanical systems considered here can be described with Kirchoff's laws, that give rigorous results within a well defined model. The physical mechanisms behind the heating are identified to be the Johnson-Nyquist noises associated to the resistors, and fabrication imperfections. For comparison, the exact description of dissipation in a multi–mode optomechanical system is more involved. Nevertheless, the results presented here will be useful for guiding the intuition towards QND detection in the optical regime. As a further extension, it would be interesting to investigate the effect of squeezing. By reducing the vacuum noise, squeezing can lead to a direct improvement in λ, thus reducing the physical requirements for the QND detection.

Chapter 3

Membranes & optical cavities

In the following, we generalize the results presented in chapter 2 to the optical regime. We study the model in Fig. 3.1, where a membrane is placed within an optical cavity, and highlight features that all optomechanical setups have in common. The system in Fig. 3.1 has been already extensively studied, even in the context of phonon QND measurement [45, 78]. However, previous approaches focused on the strong dielectric regime, in which the membrane is highly reflective and the dominant contribution to the quadratic coupling is the induced one (see section 2.2.2). We develop a theoretical framework that incorporates the results known in the literature but extends them to the case of a weak dielectric.

The chapter is structured as follows. In section 3.1, we give equations and a numerical approach to find the optical field inside the cavity. These results are then used in section 3.2, where the optomechanical couplings are derived in both the regimes of interest. Finally, we find the figure of merit for phonon QND measurement λ in section 3.4, where we also compare the optomechanical system with the electromechanical one.

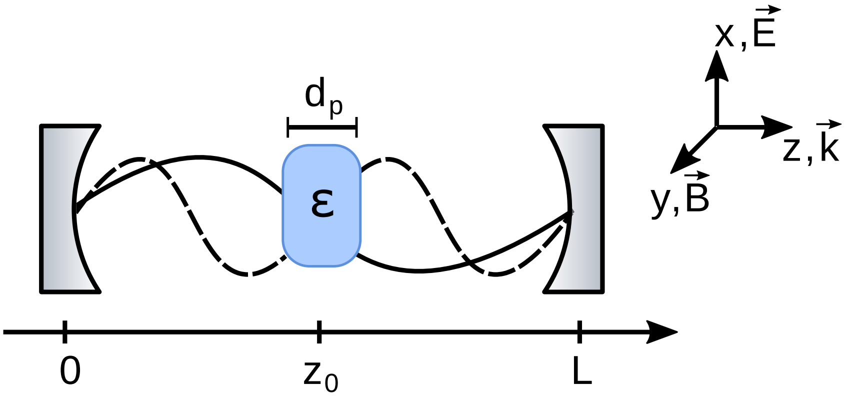

FIGURE 3.1: The optical setup. A membrane of width d_p is placed within a cavity of length L, at position z_0. The dielectric material the membrane is made of perturbs the optical modes according to its polarizability index ϵ_r. The polarization of the electric and magnetic fields, $\vec{E}$ and $\vec{B}$ respectively, is shown.

3.1 The electric field

In this section, we study the optical properties of the cavity including a dielectric. Equations for the optical field are derived both in the weak and strong dielectric limit, and a numerical approach is developed for verifying the results. We assume the membrane to be stationary and ignore the mechanical degrees of freedom. The results of this section are then used for determining the couplings and characterizing the system.

3.1.1 An exact solution

We now derive exact numerical solutions for the electric and magnetic fields in the optical cavity of Fig. 3.1. We start with Maxwell's equations without sources and in the presence of a dielectric

$$\vec{\nabla} \times \vec{E}\left(\vec{r},t\right) = -\partial_t \vec{B}\left(\vec{r},t\right), \tag{3.1a}$$

$$\vec{\nabla} \times \vec{H}\left(\vec{r},t\right) = \partial_t \vec{D}\left(\vec{r},t\right), \tag{3.1b}$$

$$\vec{\nabla} \cdot \vec{D}\left(\vec{r},t\right) = 0, \tag{3.1c}$$

$$\vec{\nabla} \cdot \vec{B}\left(\vec{r},t\right) = 0, \tag{3.1d}$$

where we defined

$$\vec{D}\left(\vec{r},t\right) = \epsilon_0 \left[1 + \epsilon_{\mathrm{r}}\left(\vec{r}\right)\right] \vec{E}\left(\vec{r},t\right), \tag{3.2a}$$

$$\vec{H}\left(\vec{r},t\right) = \frac{1}{\mu_0} \vec{B}\left(\vec{r},t\right). \tag{3.2b}$$

For simplicity, we assumed a scalar electric polarizability $\epsilon_r = 3\Re[(\epsilon - \epsilon_0)/(\epsilon + 2\epsilon_0)]$ [95], where ϵ and ϵ_0 are the membrane's and vacuum permittivity, respectively. The magnetic permittivity is neglected. A one dimensional description of the system is sufficient to extract both qualitative and quantitative dynamics. In that case, Eqs. (3.1) can be summarized by

$$\partial_z E_{\mathrm{x}}\left(z,t\right) = -\partial_t B_{\mathrm{y}}\left(z,t\right), \tag{3.3a}$$

$$\partial_z H_{\mathrm{y}}\left(z,t\right) = \partial_t D_{\mathrm{x}}\left(z,t\right), \tag{3.3b}$$

with the divergence equations (3.1c) and (3.1d) always fulfilled. The waves propagate along $\underline{z}$, and the electric and magnetic fields are polarized along $\underline{x}$ and $\underline{y}$, respectively (see Fig. 3.1). Differentiating both sides of Eq. (3.3a) in the z variable, we derive the Helmholtz equation for the electric field:

$$\left[\partial_z^2 + k^2\left(1 + \epsilon_{\mathrm{r}}(z)\right)\right] E(z) = 0, \tag{3.4}$$

where we used the Fourier decomposition (outside the dielectric)

$$E_{\mathrm{x}}(z,t) = E(z) e^{-i\omega t}. \tag{3.5}$$

In this notation, $E(z)$ is the spatial envelope of an electric field with wave vector k and angular frequency $\omega = ck$. For the setup in Fig. 3.1, we can divide the domain into three sections, and later impose boundary conditions. It follows that Eq. (3.4) becomes a system of three equations

$$\left[\partial_z^2 + k^2\right] E(z) = 0 \qquad 0 \leq z < z_0 - \frac{d_{\mathrm{p}}}{2}, \tag{3.6a}$$

$$\left[\partial_z^2 + k^2\left(1+\epsilon_{\mathrm{r}}\right)\right] E(z) = 0 \qquad z_0 - \frac{d_{\mathrm{p}}}{2} \leq z < z_0 + \frac{d_{\mathrm{p}}}{2}, \tag{3.6b}$$

$$\left[\partial_z^2 + k^2\right] E(z) = 0 \qquad z_0 + \frac{d_{\mathrm{p}}}{2} \leq z < L, \tag{3.6c}$$

whose solutions are waves of the form:

$$E(z) = \mathcal{A}_1 \cos(kz) + \mathcal{A}_2 \sin(kz) \qquad 0 \leq z < z_0 - \frac{d_{\mathrm{p}}}{2}, \tag{3.7a}$$

$$E(z) = \mathcal{B}_1 e^{ik\sqrt{1+\epsilon_{\mathrm{r}}}z} + \mathcal{B}_2 e^{-ik\sqrt{1+\epsilon_{\mathrm{r}}}z} \qquad z_0 - \frac{d_{\mathrm{p}}}{2} \leq z < z_0 + \frac{d_{\mathrm{p}}}{2}, \tag{3.7b}$$

$$E(z) = \mathcal{C}_1 \cos(kz) + \mathcal{C}_2 \sin(kz) \qquad z_0 + \frac{d_{\mathrm{p}}}{2} \leq z < L. \tag{3.7c}$$

The coefficients are determined by continuity and differentiability requirements at the interfaces, and we finally get

$$E(z) = \mathcal{A} \sin(kz), \tag{3.8a}$$

$$E(z) = \mathcal{A}\left[\frac{\cos\left[k\left(z_0 - \frac{d_{\mathrm{p}}}{2}\right)\right]}{\sqrt{\epsilon_{\mathrm{r}}+1}\csc\left[k\sqrt{\epsilon_{\mathrm{r}}+1}\left(z - z_0 + \frac{d_{\mathrm{p}}}{2}\right)\right]} + \frac{\cos\left[k\sqrt{\epsilon_{\mathrm{r}}+1}\left(z - z_0 + \frac{d_{\mathrm{p}}}{2}\right)\right]}{\csc\left[k\left(z_0 - \frac{d_{\mathrm{p}}}{2}\right)\right]}\right], \tag{3.8b}$$

$$E(z) = \frac{\mathcal{A}\sin\left[k(L-z)\right]}{\sin\left[k(L - z_0 - \frac{d_{\mathrm{p}}}{2})\right]}\left[\frac{\cos\left[k(z_0 - \frac{d_{\mathrm{p}}}{2})\right]}{\sqrt{\epsilon_{\mathrm{r}}+1}\csc\left[d_{\mathrm{p}}k\sqrt{\epsilon_{\mathrm{r}}+1}\right]} + \frac{\cos\left[d_{\mathrm{p}}k\sqrt{\epsilon_{\mathrm{r}}+1}\right]}{\csc\left[k(z_0 - \frac{d_{\mathrm{p}}}{2})\right]}\right], \tag{3.8c}$$

where the domains over which these solutions are valid, are the same as in Eqs. (3.7). The wave vectors k are found with the transcendental equation

$$\begin{aligned} &\sin\left[k\left(z_0 - \frac{d_{\mathrm{p}}}{2}\right)\right]\left[\sqrt{\epsilon_{\mathrm{r}}+1}\frac{\cos\left(d_{\mathrm{p}}k\sqrt{\epsilon_{\mathrm{r}}+1}\right)}{\tan\left[k(L - z_0 - \frac{d_{\mathrm{p}}}{2})\right]} - (\epsilon_{\mathrm{r}}+1)\sin\left(d_{\mathrm{p}}k\sqrt{\epsilon_{\mathrm{r}}+1}\right)\right] + \\ &\cos\left[k\left(z_0 - \frac{d_{\mathrm{p}}}{2}\right)\right]\left[\frac{\sin\left(d_{\mathrm{p}}k\sqrt{\epsilon_{\mathrm{r}}+1}\right)}{\tan\left[k\left(L - z_0 - \frac{d_{\mathrm{p}}}{2}\right)\right]} + \sqrt{\epsilon_{\mathrm{r}}+1}\cos\left(d_{\mathrm{p}}k\sqrt{\epsilon_{\mathrm{r}}+1}\right)\right] = 0, \end{aligned} \tag{3.9}$$

that reduces to $\sin(kL) = 0$ in the absence of dielectric. Whenever $\epsilon_{\mathrm{r}} > 0$, Eq. (3.9) can be solved numerically. It is convenient to label all possible (discrete) values of the wave vectors as $k_i = \tilde{k}_i + \delta k_i$, where $\tilde{k}_i = i\pi/L$ are the unperturbed wave vectors, and δk_i the corrections. Since the transcendental equation (3.9) generally has several solutions, it is important to find the physically relevant one. The dielectric prolongs the optical path, and therefore the wave vectors k_i decrease[1]. To find all solutions for k_i, we start with a small ϵ_r, and pick the negative value for δk_i closest to zero. By increasing ϵ_r, we then choose δk_i such that it is a continuous function in ϵ_{r}. In Fig. 3.2, we show the wave vectors k_i, for a membrane placed in the middle of the cavity $z_0 = L/2$. For small ϵ_{r}, all odd modes (dotted curves) are more perturbed than the even ones (solid curves). This follows from the fact that the odd modes have a peak at the dielectric position, while the even a node. By increasing ϵ_{r}, we

---

[1] Another way to understand this, is to look at Eq. (3.26). The system energy is reduced by the dielectric and the optical frequencies are thus required to decrease.

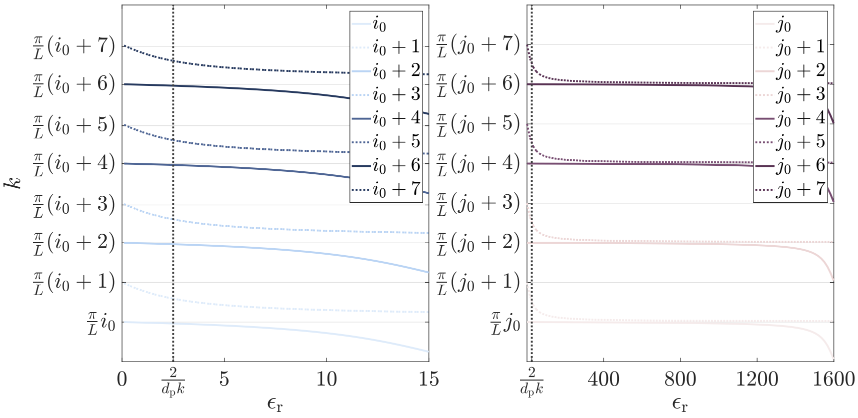

FIGURE 3.2: Optical wave vectors k_i as a function of the dielectric polarizability ϵ_r. The dotted and plain lines represent, respectively, odd and even modes. The index $i_0 = 334\,996$ corresponds to a wavelength of 400 nm, while $j_0 = 33\,496$ to a wavelength of 4 μm. The cavity is 6.7 cm long, the dielectric is placed at $z_0 = L/2$, and is $d_\mathrm{p} = 50$ nm thick. The vertical dashed lines indicate the limit $\epsilon_\mathrm{r} d_\mathrm{p} k = 2$.

prolong the optical path in the dielectric, till half of the wavelength λ fits inside. In that region, we get the opposite behaviour, with the odd modes more perturbed than the even ones. In the following, we assume that we are in the limit

$$\frac{2d_\mathrm{p}}{\lambda}\sqrt{1+\epsilon_\mathrm{r}} \ll 1, \tag{3.10}$$

which is generally desirable for strong optomechanical coupling, and therefore favours the phonon QND detection[2]. As we discuss in section 3.3, the frequency difference between optical modes is deeply involved in the heating of the mechanical system. In Fig. 3.2, it is clearly visible that the distance between consecutive modes changes with the dielectric polarizability ϵ_r. The minimum relative difference, achieved for strong dielectric, can be estimated to be $\sim \pi^2 d_\mathrm{p}/8\tilde{\lambda}_i$, where $\tilde{\lambda}_i = 2\pi/\tilde{k}_i$ is the unperturbed wavelength of the i-th mode (see section 3.1.3).

Once the wave vectors k_i are found, the only missing parameter is the normalization constant $\mathcal{A}$ in Eqs. (3.8). From quantum mechanics, the energy of the electromagnetic field is $\hbar\omega_i\left(N_\mathrm{p}+1/2\right)$, where $\omega_i = k_i c$ and N_p is the number of photons in the field. On the other side, the energy can be calculated by integrating the squared electric and magnetic fields in the cavity. To compare these two quantities, we quantize

$$D_\mathrm{x}(z,t) = D(z)\left[\hat{a}(t) + \hat{a}^\dagger(t)\right], \tag{3.11a}$$

$$H_\mathrm{y}(z,t) = iH(z)\left[\hat{a}^\dagger(t) - \hat{a}(t)\right], \tag{3.11b}$$

where we followed the procedure outlined in Ref. [96]. The spatial envelope of the magnetic field is found with $B(z) = i\partial_z E(z)/\omega$, and we introduced the creation and annihilation operators $\hat{a}^\dagger$ and $\hat{a}$ (formally defined below). Since the average of $\hat{a}^\dagger\hat{a}$

---

[2] Mostly due to the fact that thin membranes have larger zero point motion amplitudes.

gives the photons in the field, the constant $\mathcal{A}$ can be found by:

$$\frac{1}{2}\left[\int_0^L dz\,[\epsilon_0+\epsilon_{\mathrm{r}}(z)]\,|E(z)|^2+\int_0^L dz\frac{1}{\mu_0}|B(z)|^2\right]=\frac{\hbar\omega}{2}. \tag{3.12}$$

With the wave vectors and the normalization constant determined by Eq. (3.9) and Eq. (3.12) respectively, Eqs. (3.8) can be used to find the electric field for any value of the polarizability ϵ_{r}. In Fig. 3.3, the odd and the next even modes of the electric field are plotted nearby the dielectric in the limit $\epsilon_{\mathrm{r}} d_{\mathrm{p}} k \gg 2$. As it is possible to see, only the odd mode is strongly modified by the dielectric.

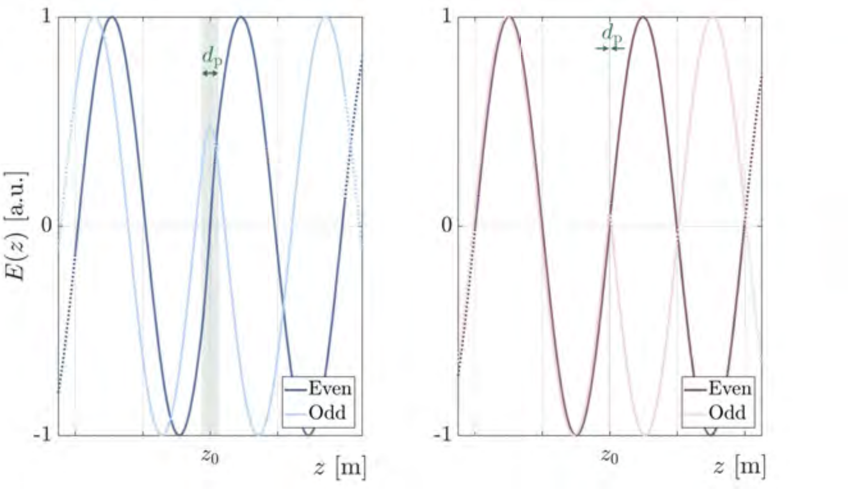

FIGURE 3.3: Spatial envelopes of the even and next odd optical modes. For the **left** plot, wavelengths around $\lambda = 400$ nm and $\epsilon_{\mathrm{r}} = 5$ have been chosen, while in the **right** one $\lambda = 4\ \mu$m and $\epsilon_{\mathrm{r}} = 500$. The dielectric, represented with the green shadowed area, is positioned in the middle of the cavity and has a width of $d_{\mathrm{p}} = 50$ nm.

3.1.2 The weak dielectric limit

In the limit $\epsilon_{\mathrm{r}} d_{\mathrm{p}} k \ll 2$, the dielectric gently perturbs the electromagnetic radiation, and analytical expressions for the fields can be derived. In the following, we introduce the unperturbed expressions for the fields and study the case of a delta-like dielectric [97, 98]. Finally, we compare these approaches with the exact solutions found above in section 3.1.1.

By solving the Helmholtz equation (3.4) without dielectric, it is possible to see that the fields in an empty cavity assume the form:

$$\hat{E}_{\mathrm{x}}(z,t)=\sum_i\sqrt{\frac{\hbar\tilde{\omega}_i}{\epsilon_0 L}}\sin\left(\tilde{k}_i z\right)\left[\hat{a}_i(t)+\hat{a}_i^\dagger(t)\right], \tag{3.13a}$$

$$\hat{B}_{\mathrm{y}}(z,t)=\frac{i}{c}\sum_i\sqrt{\frac{\hbar\tilde{\omega}_i}{\epsilon_0 L}}\cos\left(\tilde{k}_i z\right)\left[\hat{a}_i^\dagger(t)-\hat{a}_i(t)\right], \tag{3.13b}$$

where $\tilde{\omega}_i = c\tilde{k}_i$. The spatial envelopes $E^{(i)}(z)$ of the i-th mode of the unperturbed electric field is the well known:

$$E^{(i)}(z) = \sqrt{\frac{\hbar\tilde{\omega}_i}{\epsilon_0 L}} \sin\left(\tilde{k}_i z\right). \tag{3.14}$$

We refer to Eq. (3.14) as the unperturbed electric field.

Let us consider a delta-like dielectric at any position z_0 in the cavity. Following Refs. [97, 98], we substitute the step-like dielectric $\epsilon_\mathrm{r}(z)$ in Eq. (3.4) with the expression $\epsilon_\mathrm{r} d_\mathrm{p} \delta(z - z_0)$. The spatial envelope of the electric field becomes

$$E(z) = \mathcal{A}\sin(kz) \qquad 0 \leq z < z_0, \tag{3.15a}$$

$$E(z) = \mathcal{A}\frac{\sin(kz_0)}{\sin[k(L - z_0)]}\sin[k(L - z)] \qquad z_0 \leq z < L, \tag{3.15b}$$

with the discrete wave vectors k determined by:

$$d_\mathrm{p} k \epsilon_\mathrm{r}\left[\cos(kL) - \cos\left[k(L - 2z_0)\right]\right] = 2\sin(kL). \tag{3.16}$$

Like above, we find the deviation δk_i from the unperturbed value $\tilde{k}_i$ of the wave vectors:

$$\delta k_i \simeq -\tilde{k}_i \frac{d_\mathrm{p}\epsilon_\mathrm{r}\sin^2\left(\tilde{k}_i z_0\right)}{L}, \tag{3.17}$$

that is valid in the limit $\epsilon_\mathrm{r} d_\mathrm{p} k \ll 2$. With Eq. (3.12), it is possible to determine the normalization constant $\mathcal{A}$ in Eqs. (3.15) [98]:

$$|\mathcal{A}|^2 \simeq \frac{\hbar\omega}{\epsilon_0}\left[z_0 + \left(\frac{\sin(\tilde{k}_i z_0)}{\sin\left[\tilde{k}_i(L - z_0)\right]}\right)^2 (L - z_0)\right]^{-1}. \tag{3.18}$$

In Fig. 3.4, we compare the spatial envelopes $E(z)$ of the electric fields found with the three presented methods. In light blue, we show the unperturbed solution of Eq. (3.14); in blue the delta-like of Eqs. (3.15), and in dark blue the full numerical of Eqs. (3.8). The plots are in a neighbourhood of the membrane, and for different values of $\epsilon_\mathrm{r} d_\mathrm{p} k$. The figure confirms that in the weak dielectric limit $\epsilon_\mathrm{r} d_\mathrm{p} k \ll 2$ the unperturbed and the delta-like solutions describe the system well. With $\epsilon_\mathrm{r} d_\mathrm{p} k$ approaching unity, however, the unperturbed solution is clearly off, and the delta-like starts deviating from the exact one.

3.1.3 The strong dielectric limit

Deriving analytical results in the opposite limit $\epsilon_\mathrm{r} d_\mathrm{p} k \gg 2$ is challenging. The dielectric is no longer a small perturbation, and the fields are radically modified by its presence. Moreover, the additional requirement of having a small increase in the optical path $2d_\mathrm{p}\sqrt{\epsilon_\mathrm{r} + 1} \ll \lambda$ makes asymptotic expansions hard to derive. However, by carefully eliminating negligible contributions, we will find simple expressions for the relevant quantities in the most interesting case of the membrane–in–the–middle setup $z_0 = L/2$.

Since we are interested in the optomechanical couplings, we want to know the amplitude and shape of the electric field inside the dielectric. The wave vectors k_i and the field in the middle of the membrane $E^{(i)}(z_0)$ suffice to this goal. By imposing

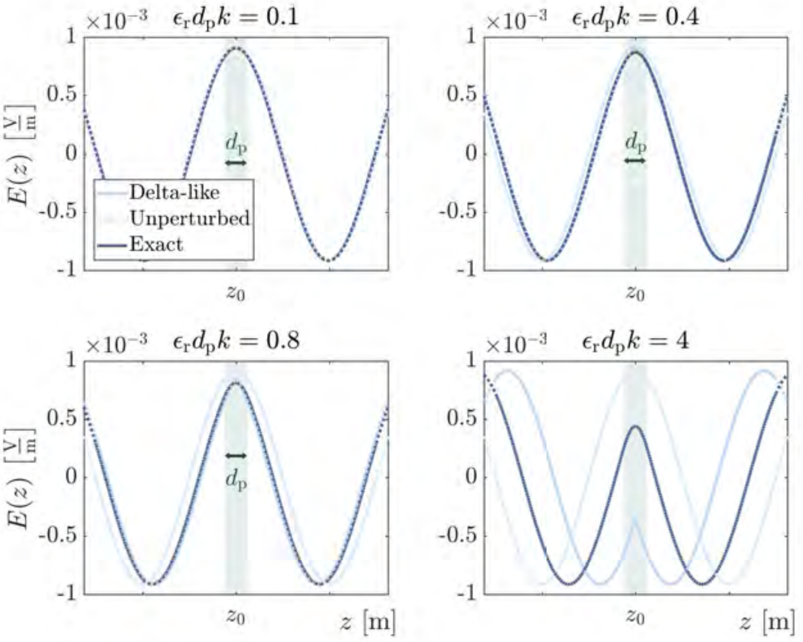

FIGURE 3.4: Spatial envelopes of the electric fields for different values of $\epsilon_r d_p k$. The three lines represent the unperturbed (light blue), the delta-like (blue), and the exact (dark blue) solutions. The green shadowed area indicates the dielectric spatial extension. We chose an odd mode with wavelength around $\lambda = 400$ nm, a cavity of length $L = 6.7$ cm, and a membrane thickness of $d_p = 50$ nm.

the above mentioned constraints into Eq. (3.9), we find:

$$\delta k_i = \frac{4}{(i-1)\pi d_p \epsilon_r} - \frac{\pi}{L} \qquad \forall \text{ odd } i > 1, \tag{3.19a}$$

$$\delta k_i = 0 \qquad \forall \text{ even } i \geq 2. \tag{3.19b}$$

With these results and Eqs. (3.8), equations for the electric fields $E^{(i)}(z)$ can be derived. By determining the normalization constant, the amplitude $E^{(i)}(z_0)$ is approximated by:

$$E^{(i)}(z_0) = 2\sqrt{\frac{\hbar c}{\epsilon_0 d_p^2} \frac{(-1)^{\frac{i-1}{2}}}{\epsilon_r \sqrt{\pi(i-1)}}} \qquad \forall \text{ odd } i > 1, \tag{3.20a}$$

$$E^{(i)}(z_0) = 0 \qquad \forall \text{ even } i \geq 2. \tag{3.20b}$$

The electric modes in the membrane can thus be approximated with their first non-zero contributions in the expansion:

$$E^{(i)}(z) = E^{(i)}(z_0)\left(1 - \frac{\left[k_i\sqrt{1+\epsilon_r}(z-z_0)\right]^2}{2}\right) \qquad \forall \text{ odd } i > 1, \tag{3.21a}$$

$$E^{(i)}(z) = (-1)^{\frac{i}{2}} k_i (z - z_0) \qquad \forall \text{ even } i \geq 2. \tag{3.21b}$$

These equations will be later used to determine the relevant optomechanical couplings. In Fig. 3.5, we compare the exact solution with the approximate ones derived for the weak and strong dielectric limits. In the two plots, the wave vectors and the field amplitudes are presented in a range of ϵ_r that spans both the regimes. As it is possible to see, the exact solution is well described by Eqs. (3.17) and (3.18) for $\epsilon_r d_p k \ll 2$, and Eqs. (3.19) and (3.21) for $\epsilon_r d_p k \gg 2$. When the optical path inside the dielectric starts to become comparable with the wavelength (the green, shadowed areas in the figure), the exact solution begins to deviate from the analytical one.

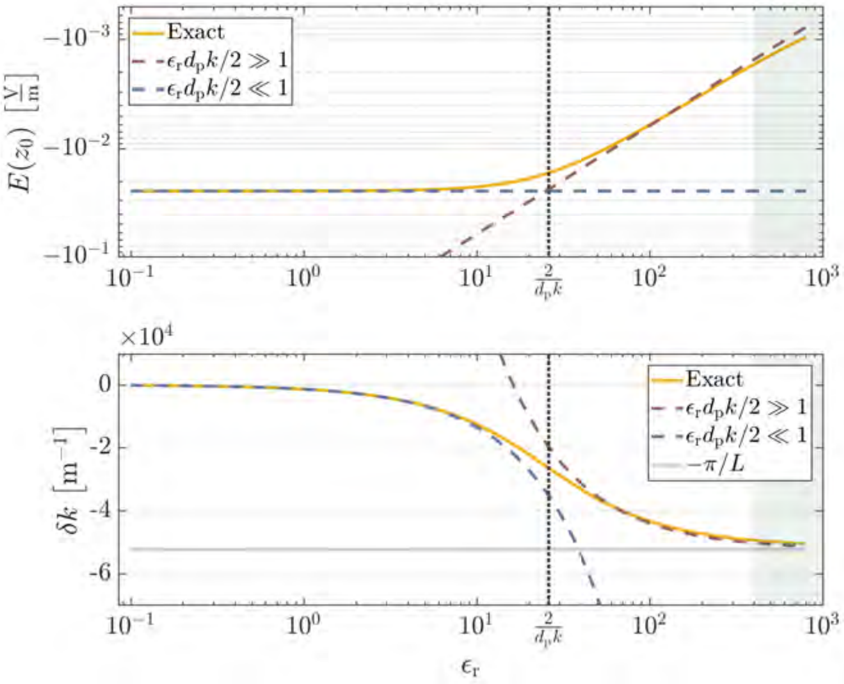

FIGURE 3.5: Electric field amplitude $E(z_0)$ and correction to the wave vector δk for an odd mode, as a function of ϵ_r. Plain lines are derived by numerically solving Maxwell equations. Dotted lines represent the analytical expressions for weak (blue) and strong (dark red) dielectric. The green shadowed areas correspond to $d_p\sqrt{1+\epsilon_r} \geq \lambda/4$. For both plots, $\lambda = 4\ \mu$m, $L = 60\ \mu$m, and $d_p = 50$ nm.

3.2 Optomechanical couplings

Here, we derive the Hamiltonian describing the optical and mechanical systems, and the optomechanical interactions. There are several ways to do that, depending whether we consider the unperturbed, the delta-like, or the exact solutions for the optical modes. In any case, we start from the energy of the optical field

$$H_o = \frac{1}{2}\left[\frac{1}{\epsilon_0}\int_0^L dz \frac{D_x^2(z,t)}{[1+\epsilon_r(z)]} + \mu_0 \int_0^L dz H_y^2(z,t)\right], \tag{3.22}$$

where the electric and magnetic fields are sums of discrete modes. The choice of using the D and H fields instead of E and B follows from Ref. [96], where it is shown that they are the conjugate momenta of the optical field. Other choices for

H_o would result in ill-defined couplings. As seen above, the dielectric hybridizes the optical modes, changing the orthonormal eigenstates of the optical system (see Figs. 3.3 and 3.4). If we describe the electric D field in terms of the exact solutions, this Hamiltonian is diagonal. Otherwise, it carries an interaction term that couples different optical modes. To clarify this, we quantize and rewrite Eq. (3.22):

$$\hat{H}_\mathrm{o} = \sum_i \frac{\hat{\Phi}_i^2}{2} + \frac{\omega_i^2}{2}\hat{Q}_i^2 + \underbrace{\sum_{i,j} g_0[i,j]\frac{\sqrt{\omega_i\omega_j}}{2}\hat{Q}_i\hat{Q}_j}_{\mathrm{off-diagonal}}, \tag{3.23}$$

where the blue term is absent for the exact solutions, and $g_0[i,j]$ is determined later. The operators $\hat{Q}_i$ and $\hat{\Phi}_i$ are the position and momentum of the field[3], as derived in Ref. [96]. The subscript 'i' refers to the i-th mode of the fields $\hat{D}_\mathrm{x}(z,t)$ and $\hat{H}_\mathrm{y}(z,t)$. As it is required for canonical operators, $\hat{Q}_i$ and $\hat{\Phi}_i$ satisfy standard commutation relations $\left[\hat{Q}_i, \hat{\Phi}_j\right] = i\hbar\delta_{i,j}$. It is possible to rewrite the optical Hamiltonian of Eq. (3.23) in terms of $\hat{a}_i$ and $\hat{a}_i^\dagger$

$$\hat{H}_\mathrm{o} = \sum_i \hbar\omega_i \hat{a}_i^\dagger \hat{a}_i + \underbrace{\hbar\sum_{i,j} g_0[i,j]\left(\hat{a}_i + \hat{a}_i^\dagger\right)\left(\hat{a}_j + \hat{a}_j^\dagger\right)}_{\mathrm{off-diagonal}}, \tag{3.24}$$

where, again, the blue term is absent for the exact solutions of the electric modes. The creation and annihilation operators can now be formally defined in terms of the quadratures:

$$\hat{a}_i = \frac{1}{\sqrt{2}}\left[\sqrt{\frac{\omega_i}{\hbar}}\hat{Q}_i - i\sqrt{\frac{1}{\hbar\omega_i}}\hat{\Phi}_i\right], \tag{3.25a}$$

$$\hat{a}_i^\dagger = \frac{1}{\sqrt{2}}\left[\sqrt{\frac{\omega_i}{\hbar}}\hat{Q}_i + i\sqrt{\frac{1}{\hbar\omega_i}}\hat{\Phi}_i\right], \tag{3.25b}$$

and satisfy the commutation relations $\left[\hat{a}_i, \hat{a}_j^\dagger\right] = \delta_{i,j}$. To find the optomechanical couplings, it is convenient to quantize and rewrite Eq. (3.22) by isolating the dielectric contribution. Adding and subtracting the integral $\int_0^L dz D_\mathrm{x}^2(z,t)/2\epsilon_0$, we get:

$$\begin{aligned}\hat{H}_\mathrm{o} = {} & \frac{1}{2\epsilon_0}\sum_{i,j}\left[\int_0^L dz D^{(i)}(z)D^{(j)}(z)\right]\left(\hat{a}_i + \hat{a}_i^\dagger\right)\left(\hat{a}_j + \hat{a}_j^\dagger\right) \\ & - \frac{1}{2\epsilon_0}\sum_{i,j}\left[\int_0^L dz \frac{\epsilon_\mathrm{r}(z;z_0)}{\epsilon_\mathrm{r}(z;z_0)+1} D^{(i)}(z)D^{(j)}(z)\right]\left(\hat{a}_i + \hat{a}_i^\dagger\right)\left(\hat{a}_j + \hat{a}_j^\dagger\right) \\ & - \frac{\mu_0}{2}\sum_{i,j}\left[\int_0^L dz H^{(i)}(z)H^{(j)}(z)\right]\left(\hat{a}_i - \hat{a}_i^\dagger\right)\left(\hat{a}_j - \hat{a}_j^\dagger\right),\end{aligned} \tag{3.26}$$

where $D^{(i)}(z)$ and $H^{(i)}(z)$ represent the spatial envelopes of the i-th mode of the electric and magnetic fields, respectively. In Eq.(3.26), we stress that the polarizability ϵ_r is a function of both the dielectric position z_0 and the z coordinate. By plugging

---

[3] At the present time, there is a lack of formality in the optical quantization. This will be clear later on, when we discuss about Eq. (3.30). Despite, for our purposes, this is not a problem, current research is focused in solving this issue.

in the spatial envelopes of the modes found in section 3.1, from Eq. (3.26) we can re-derive Eq. (3.23). The utility of Eq. (3.26), is that the membrane's position z_0 is now isolated to only one term[4], $\epsilon_r(z;z_0)$. This will be useful later, for finding the optomechanical couplings $g_n[i,j]$.

To work in a well defined environment, we introduce the mechanical Hamiltonian $\hat{H}_m$. By considering only one mode at frequency ω_m, we have that

$$\hat{H}_m = \hbar\omega_m \hat{b}^\dagger \hat{b}, \tag{3.27}$$

where $\hat{b}^\dagger$ and $\hat{b}$ are the creation and annihilation operators of a phonon, respectively. The quantized position $\hat{z}_0$ and momentum $\hat{p}_0$ of the oscillator are found from $\hat{b}^\dagger$ and $\hat{b}$ with the relations

$$\hat{z}_0 = \sqrt{\frac{\hbar}{2m\omega_m}}\left(\hat{b} + \hat{b}^\dagger\right), \tag{3.28a}$$

$$\hat{p}_0 = i\sqrt{\frac{\hbar m\omega_m}{2}}\left(\hat{b}^\dagger - \hat{b}\right), \tag{3.28b}$$

and satisfy standard commutation relations $[\hat{z}_0, \hat{p}_0] = i\hbar$. With Eq. (3.26), it is in principle possible to derive any optomechanical coupling by computing the derivatives $\xi^{(n)}_{i,j}$:

$$\xi^{(n)}_{i,j} = \left[\partial^n_{z_0}\hat{H}_o\right]_{i,j}, \tag{3.29}$$

where the subscript i,j indicate the contributions from the respective field components. From the definition of $\hat{H}_o$ in Eq. (3.26), we conclude that the only contribution to $\xi^{(n)}_{i,j}$ is given by the term in the middle, such that:

$$\xi^{(n)}_{i,j} = -\frac{1}{2\epsilon_0}\partial^n_{z_0}\int_0^L dz \frac{\epsilon_r(z;z_0)}{\epsilon_r(z;z_0)+1} D^{(i)}(z) D^{(j)}(z). \tag{3.30}$$

The quantity $\xi^{(n)}_{i,j}$ is easy to compute in the weak dielectric limit $\epsilon_r d_p k \ll 2$, where we can approximate the electric field with its unperturbed expressions of Eq. (3.14). In the opposite regime, Eq. (3.30) is well defined for $n = 1$, but diverges otherwise. As such, it cannot be used for determining the quadratic and higher order couplings, and other methods have to be sought (see sections 3.2.3 and 3.2.4). The n-th coupling $g_n[i,j]$ between the mechanical system and the optical modes i and j is then (when is well defined)

$$g_n[i,j] = \frac{x_z^n}{\hbar}\xi^{(n)}_{i,j}, \tag{3.31}$$

where $x_z = \sqrt{\hbar/2m\omega_m}$ is the zero point motion of the membrane.

The value for $\xi^{(n)}_{i,j}$, and thus $g_n[i,j]$, varies depending on the basis used for their derivation: the unperturbed, the delta-like or the exact solutions for the optical modes. We can thus confirm that the off-diagonal terms in Eqs. (3.23) and (3.26) disappear, once we consider the exact spatial envelopes of the field. The interaction Hamiltonian $\hat{H}_{int}$ between the optical and the mechanical systems can finally be

---

[4] To be precise, both the spatial envelopes and the creation (annihilation) operators of the optical fields depend on z_0. In this work, we assume that the dielectric motion slightly perturbs the electric field, and is 'slow' if compared to the optical dynamics. With 'slow', we mean that we ignore velocity effects on the polarizability. Under these assumptions, Eq. (3.26) is a good approximation of our system.

written as:

$$\hat{H}_{\text{int}} = \hbar \sum_{n\geq 1} \sum_{i,j} \frac{g_n[i,j]}{n!} \left(\hat{a}_i + \hat{a}_i^\dagger\right) \left(\hat{a}_j + \hat{a}_j^\dagger\right) \left(\hat{b} + \hat{b}^\dagger\right)^n . \tag{3.32}$$

Notice that $\hat{H}_{\text{int}}$ is usually expressed with the rotating wave approximation (RWA) $\left(\hat{a}_i + \hat{a}_i^\dagger\right)\left(\hat{a}_j + \hat{a}_j^\dagger\right) \simeq \hat{a}_i\hat{a}_j^\dagger + \hat{a}_i^\dagger\hat{a}_j$. In our case, this is not always justified, since we consider interactions between optical modes that are far off detuned from each other. However, as motivated in the following, the relevant contributions to the system's dynamics are the ones near resonance with the driven optical mode. Therefore, to simplify the following derivations, we assume the RWA.

Next, we derive analytical expressions for the linear and quadratic optomechanical couplings. These expressions describe the two fundamentally different regimes of weak and strong dielectric. We stress, however, that the exact couplings of *any* order can be derived from Eqs. (3.30) and (3.31), whenever the integral in Eq. (3.30) is convergent[5]. Moreover, in section 3.2.4 we describe a procedure allowing us to calculate them numerically for any ϵ_{r}. Unfortunately, though, the required computational resources scale badly with the order of the coupling.

3.2.1 Linear and quadratic couplings in the weak dielectric limit

In section 3.1.2, we showed that the delta-like and the unperturbed solutions accurately describe the system for $\epsilon_{\text{r}} d_{\text{p}} k \ll 2$. With the latter one, it is possible to derive all contributions to any order in z_0 of the optomechanical coupling. By setting $D^{(i)}(z) = \epsilon_0 E^{(i)}(z)$, Eq. (3.30) can be expressed by

$$\begin{aligned} g_n[i,j] = \frac{\epsilon_{\text{r}}}{\epsilon_{\text{r}}+1} \frac{\epsilon_0 x_{\text{z}}^n}{2} \partial_{z_0}^{n-1} \Bigg[& E^{(i)}\left(\tilde{k}_i z_0 - \frac{d_{\text{p}}}{2}\right) E^{(j)}\left(\tilde{k}_j z_0 - \frac{d_{\text{p}}}{2}\right) \\ & - E^{(i)}\left(\tilde{k}_i z_0 + \frac{d_{\text{p}}}{2}\right) E^{(i)}\left(\tilde{k}_j z_0 + \frac{d_{\text{p}}}{2}\right) \Bigg], \end{aligned} \tag{3.33}$$

that is valid for any $n \geq 1$. Plugging Eq. (3.14) into this last equation, we find:

$$\begin{aligned} g_n[i,j] = \frac{\epsilon_{\text{r}}}{\epsilon_{\text{r}}+1} \frac{x_{\text{z}}^n \sqrt{\tilde{\omega}_i \tilde{\omega}_j}}{2L} \partial_{z_0}^{n-1} \Bigg[& \sin\left(\tilde{k}_i z_0 - \frac{d_{\text{p}}}{2}\right) \sin\left(\tilde{k}_j z_0 - \frac{d_{\text{p}}}{2}\right) \\ & - \sin\left(\tilde{k}_i z_0 + \frac{d_{\text{p}}}{2}\right) \sin\left(\tilde{k}_j z_0 + \frac{d_{\text{p}}}{2}\right) \Bigg], \end{aligned} \tag{3.34}$$

where $\tilde{\omega}_i = c\tilde{k}_i$. The zeroth order couplings ($n = 0$) describe the interactions between different optical modes, and give the form of the off diagonal terms in Eqs. (3.23) and (3.24):

$$g_0[i,j] = -\frac{\epsilon_{\text{r}}}{\epsilon_{\text{r}}+1} \frac{\sqrt{\tilde{\omega}_i \tilde{\omega}_j}}{2L} \int_{z_0 - \frac{d_{\text{p}}}{2}}^{z_0 + \frac{d_{\text{p}}}{2}} dz \sin\left(\tilde{k}_i z\right) \sin\left(\tilde{k}_j z\right) . \tag{3.35}$$

An approximation for all couplings can be derived in the limit $d_{\text{p}} \ll \lambda$:

$$g_n[i,j] \simeq -\frac{\epsilon_{\text{r}}}{\epsilon_{\text{r}}+1} \frac{x_{\text{z}}^n d_{\text{p}} \sqrt{\tilde{\omega}_i \tilde{\omega}_j}}{2L} \partial_{z_0}^n \left[\sin\left(\tilde{k}_i z_0\right) \sin\left(\tilde{k}_j z_0\right)\right] . \tag{3.36}$$

---

[5] This is always ensured whenever $\epsilon_{\text{r}} d_{\text{p}} k \ll 2$.

From Eq. (3.35), it follows that for $\epsilon_{\mathrm{r}} d_{\mathrm{p}} k \ll 2$ the first order corrections to the unperturbed modes resemble the delta-like solutions in Eq. (3.15). Furthermore, as detailed in section 3.2.4, the unperturbed approach can be used for confirming the exact solutions. This constitutes an additional check, particularly for the couplings.

Using Eq. (3.36), we give the explicit form of $g_1[i,j]$ and $g_2[i,j]$, that represent central quantities in our analysis:

$$g_1[i,j] \simeq -\frac{x_{\mathrm{z}}}{c}\frac{\epsilon_{\mathrm{r}} d_{\mathrm{p}}}{2L}\sqrt{\tilde{\omega}_i\tilde{\omega}_j}\left[\tilde{\omega}_i \sin\left(\tilde{k}_j z_0\right)\cos\left(\tilde{k}_i z_0\right) + \tilde{\omega}_j \sin\left(\tilde{k}_i z_0\right)\cos\left(\tilde{k}_j z_0\right)\right], \tag{3.37a}$$

$$\begin{aligned} g_2[i,j] \simeq -\frac{x_{\mathrm{z}}^2}{c^2}\frac{\epsilon_{\mathrm{r}} d_{\mathrm{p}}}{4L}\sqrt{\tilde{\omega}_i\tilde{\omega}_j}\Big[& 2\tilde{\omega}_i\tilde{\omega}_j \cos\left(\tilde{k}_j z_0\right)\cos\left(\tilde{k}_i z_0\right) \\ & - \left(\tilde{\omega}_i^2 + \tilde{\omega}_j^2\right)\sin\left(\tilde{k}_j z_0\right)\cos\left(\tilde{k}_i z_0\right)\Big]. \end{aligned} \tag{3.37b}$$

Importantly, for $i = j$ Eqs. (3.37) can be derived from Eq. (3.17), confirming that the unperturbed and delta-like solutions give the same first order corrections due to the mechanical motion.

Let us state two relevant properties of $g_1[i,j]$ and $g_2[i,j]$, when the membrane is placed in the middle of the cavity $z_0 = L/2$. First, no mode is linearly coupled with the mechanical motion: $g_1[i,i] = 0$ for any i. The linear couplings always describe three body interaction between the mechanical motion and two optical modes: one even, one odd. These terms are the membrane's heating source and the main limitation to the phonon QND measurement. In Ref. [78], it is shown that the strong coupling regime is required to have a phonon QND measurement, in the particular case in which the quadratic coupling is negligible. As we proved for an electromechanical setup in chapter 2, the situation is different with an intrinsic g_2 coupling, and more general conditions for the QND measurement can be obtained [see Eqs. (2.5)]. In the following, we extend the electromechanical result to the case of multimode optomechanics. A second comment on Eqs. (3.37) regards the couplings' magnitude. While the $g_1[i,j]$ are linear in the zero point motion fluctuations, the $g_2[i,j]$ are quadratic in that parameter. Due to the smallness of the Planck constant, this implies $g_2[i,j] \ll g_1[i,j]$. This allows us to neglect the quadratic couplings, *except* for the ones of modes directly driven by strong classical fields. Similarly to what we have seen in section 2.2.1, these terms have a resonant contribution, and thus cannot be neglected.

3.2.2 Linear and quadratic couplings in the strong dielectric limit

In section 3.1.3, we found simple expressions for the electric field in the strong dielectric limit, and the membrane in the middle of the cavity $z_0 = L/2$. Using Eqs. (3.21), the linear optomechanical couplings can be found from Eq. (3.31). We start by rewriting Eq. (3.30) with the derivative inside the integral. For $n = 1$, the result is convergent and we get:

$$\xi_{i,j}^{(1)} = -\frac{1}{2\epsilon_0}\int_0^L dz \frac{\partial_{z_0}\epsilon_{\mathrm{r}}(z;z_0)}{\left[\epsilon_{\mathrm{r}}(z;z_0)+1\right]^2} D^{(i)}(z) D^{(j)}(z). \tag{3.38}$$

We rewrite the polarizability in terms of Heaviside theta functions θ:

$$\epsilon_{\mathrm{r}}(z, z_0) = \bar{\epsilon}_{\mathrm{r}}\theta\left(z - z_0 + \frac{d_{\mathrm{p}}}{2}\right)\theta\left(-z + z_0 + \frac{d_{\mathrm{p}}}{2}\right), \tag{3.39}$$

so that Eq. (3.38) becomes:

$$\xi^{(1)}_{i,j} = \frac{\bar{\epsilon}_{\mathrm{r}}}{2\epsilon_0}\int_0^L dz \frac{D^{(i)}(z)D^{(j)}(z)}{\left[1 + \epsilon_{\mathrm{r}}(z, z_0)\right]^2}\left[\delta\left(z - z_0 + \frac{d_{\mathrm{p}}}{2}\right) - \delta\left(-z + z_0 + \frac{d_{\mathrm{p}}}{2}\right)\right]. \tag{3.40}$$

Since the D field is not continuous in the coordinates identified by the two Dirac deltas, we switch to the electric field $E(z) = \epsilon^{-1}D(z)$ to rewrite Eq. (3.40):

$$\xi^{(1)}_{i,j} = \frac{\bar{\epsilon}_{\mathrm{r}}}{2\epsilon_0}\left[E^{(i)}\left(z_0 - \frac{d_{\mathrm{p}}}{2}\right)E^{(j)}\left(z_0 - \frac{d_{\mathrm{p}}}{2}\right) - E^{(i)}\left(z_0 + \frac{d_{\mathrm{p}}}{2}\right)E^{(j)}\left(z_0 + \frac{d_{\mathrm{p}}}{2}\right)\right]. \tag{3.41}$$

By plugging Eqs. (3.21) and (3.19) into Eq. (3.41), we finally find:

$$g_1\left[j_{\mathrm{e}}, j_{\mathrm{o}}\right] = c\frac{x_{\mathrm{z}}}{L^2}\frac{\pi j_{\mathrm{e}}^{3/2} i^{j_{\mathrm{e}}+j_{\mathrm{o}}-1}}{\sqrt{(j_{\mathrm{o}} - 1)}}, \tag{3.42}$$

where subscripts 'e' and 'o' indicate even and odd indices, respectively. Due to symmetry, in the limit $2d_{\mathrm{p}}\sqrt{1+\epsilon_{\mathrm{r}}} \ll \lambda$ the linear coupling is always between an odd and an even optical modes. Importantly, this result is in agreement with the literature, Refs. [78, 45], where the optomechanical system of Fig. 3.1 was modelled by two distinct cavities. Justified by the assumption of strong dielectric, these works identify the linear coupling between the mechanics, the even, and the next odd optical modes with $g_1 = (-1)^{i_{\mathrm{e}}} x_{\mathrm{z}}\omega_{\mathrm{e}}/L$. Here, ω_{e} is the frequency of the even mode i_{e}. The same result is found with our method, Eq. (3.42), by setting $j_{\mathrm{o}} = j_{\mathrm{e}} + 1$. Thus, our work generalizes the results of Refs. [78, 45], in the sense that we take into account all optical modes, and extend the predictions to any dielectric polarizability. In Fig. 3.6, we compare the values of the linear coupling obtained numerically and analytically. The solid line is derived by exactly solving Maxwell equation, and using Eq. (3.41) to evaluate $g_1[i,j]$. As it is possible to see, the numerical solution confirms both the predictions for weak [Eq. (3.37a)] and strong [Eq. (3.42)] dielectrics.

It is worth mentioning that Eq. (3.41) agrees with Ref. [99], where corrections to the optical fields due to the motion of an arbitrary dielectric are derived. In particular, Eq. (3.41) resembles the contribution of the component of the E field that is parallel to the dielectric. The other contribution involves the perpendicular component of the D field, as it is the one that is continuous at the interface. The connection between the results of Ref. [99] and the optomechanical couplings, is not straightforward. In fact, to derive $g_1[i,j]$, the optical field needs to be quantized. The generalized Coulomb gauge that we chose according to Ref. [96], generally depends on the dielectric shape and position. In the $1D$ system of Fig. 3.1, this is not the case, as there is no perpendicular component of the electric field. However, in a general $3D$ setup, it is necessary to include the contribution of the chosen gauge to the optomechanical couplings.

As said above, simple analytical expressions describing the quadratic couplings $g_2[i,j]$ are not available in the strong dielectric regime. Therefore, we pursue a different strategy. As we have seen in section 2.2.2, the total quadratic coupling has in general two contribution: one intrinsic and one induced. The latter comes from the linear three body optomechanical interactions and, as such, can be characterized

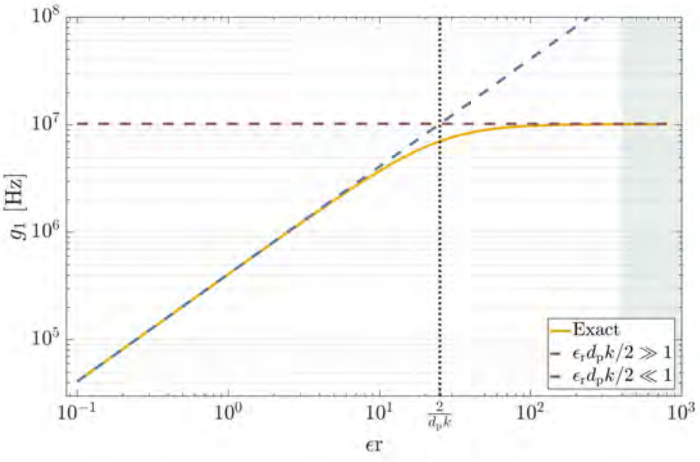

FIGURE 3.6: Linear coupling g_1 as a function of the dielectric polarizability ϵ_r. The solid line is derived by numerically solving the Maxwell equations. Dashed lines represent the analytical limits for weak [blue, Eq. (3.37a)] and strong [dark red, Eq. (3.42)] dielectric limits. The green shadowed region is identified by $d_p\sqrt{1+\epsilon_r} \geq \lambda/4$. We assumed $\lambda = 4\ \mu$m, $L = 60\ \mu$m, and $d_p = 50$ nm. The coupling is between the even and the next optical modes.

for our current system. We first compute the quadratic induced coupling, both in the weak and in the strong dielectric limits. Then, we prove that for $\epsilon_r d_p k \gg 2$, the induced coupling dominates and, as such, is sufficient for characterizing the system.

3.2.3 Intrinsic and induced optomechanical quadratic coupling

For the phonon QND measurement in an electromechanical system, we found two contributions to the non-linear interaction between the read-out mode and the phonon number. First, there is the *intrinsic* quadratic coupling, Eq. (2.41). Second, the *induced* one, allowed by the unwanted electrical mode that is detuned from the cavity resonance. The same happens in the cavity, once two (or more) optical modes are considered. Actually, this induced quadratic coupling is the main one considered in Refs. [45, 78], and in the literature so far, with few exceptions [80, 48]. This work reports the first theory where both the coupling contributions are taken into account simultaneously, to find a complete criterion for the phonon QND measurement.

We start by considering two optical modes linearly coupled to the mechanical motion. We derive the resulting induced quadratic coupling and compare it with the intrinsic one found numerically. Finally, we extend this result to an infinite number of optical modes.

Assume first that our cavity can be described by two optical modes: a driven, even one, and the next odd. Their equations of motion, including the first order mechanical interaction, are given by

$$\partial_t \hat{Q}_\mathrm{e}(t) = \hat{\Phi}_\mathrm{e}(t), \tag{3.43a}$$

$$\partial_t \hat{\Phi}_\mathrm{e}(t) = -\omega_\mathrm{e}^2 \hat{Q}_\mathrm{e}(t) - \gamma_\mathrm{e}\hat{\Phi}_\mathrm{e}(t) - 2g_1\sqrt{\omega_\mathrm{e}\omega_\mathrm{o}}\hat{Q}_\mathrm{o}(t)\left[\hat{b}(t) + \hat{b}^\dagger(t)\right] + \hat{S}_\mathrm{e}(t), \tag{3.43b}$$

$$\partial_t \hat{Q}_\mathrm{o}(t) = \hat{\Phi}_\mathrm{o}(t), \tag{3.43c}$$

$$\partial_t \hat{\Phi}_\mathrm{o}(t) = -\omega_\mathrm{e}^2 \hat{Q}_\mathrm{o}(t) - \gamma_\mathrm{o}\hat{\Phi}_\mathrm{o}(t) - 2g_1\sqrt{\omega_\mathrm{e}\omega_\mathrm{o}}\hat{Q}_\mathrm{e}(t)\left[\hat{b}(t) + \hat{b}^\dagger(t)\right] + \hat{S}_\mathrm{o}(t), \tag{3.43d}$$

where subscripts "e" and "o" indicate even and odd, respectively. The operators $\hat{S}_\mathrm{e}$ and $\hat{S}_\mathrm{o}$ generally consist of driving fields and quantum noises. By switching to the Fourier domain and setting $\hat{b}(t) = \hat{b}e^{-i\omega_\mathrm{m}t}$, we rewrite Eqs. (3.43) in the more compact form[6]:

$$-i\Omega_k \hat{Q}_\mathrm{e}\left[\Omega_k\right] = \hat{\Phi}_\mathrm{e}\left[\Omega_k\right], \tag{3.44a}$$

$$-i\Omega_k \hat{\Phi}_\mathrm{e}\left[\Omega_k\right] = -\omega_\mathrm{e}^2 \hat{Q}_\mathrm{e}\left[\Omega_k\right]\left(1 + \frac{G_2}{\omega_\mathrm{e}}\bar{n}_\mathrm{b}\right) - \gamma_\mathrm{e}\hat{\Phi}_\mathrm{e}\left[\Omega_k\right] + \hat{S}_\mathrm{e}\left[\Omega_k\right], \tag{3.44b}$$

with the Fourier frequency indicated by Ω_k, and the effect of the odd mode included in the shift G_2. To get this result, we neglected off resonant terms, the optomechanically induced decay, and the contribution from the mechanical vacuum fluctuations[7]. The parameter G_2, in capital to distinguish it from the intrinsic quadratic coupling g_2, describes the phonon dependent frequency shift that arises from the three body interaction proportional to the linear coupling in Eq. (3.32). Its general form is

$$G_2 = -\Re\left\{\frac{4g_1^2\omega_\mathrm{o}}{\omega_\mathrm{o}^2 + (\omega_\mathrm{m} - \Omega_k)(i\gamma_\mathrm{o} + \Omega_k - \omega_\mathrm{m})} + \frac{4g_1^2\omega_\mathrm{o}}{\omega_\mathrm{o}^2 - (\omega_\mathrm{m} + \Omega_k)(-i\gamma_\mathrm{o} + \Omega_k + \omega_\mathrm{m})}\right\}, \tag{3.45}$$

where $\Re$ indicates the real part. This equation includes the dynamic contribution from the mechanical motion and optical dissipation. Generally, it is possible to simplify Eq. (3.45) by driving the system on resonance $\Omega_k = \omega_\mathrm{e}$, and assuming the resolved sideband regime $\omega_\mathrm{m} \gg \gamma_\mathrm{o}$:

$$G_2 \simeq -\frac{4g_1^2\Delta\omega}{\Delta\omega^2 - \omega_\mathrm{m}^2}. \tag{3.46}$$

Here, $\Delta\omega = \omega_\mathrm{o} - \omega_\mathrm{e}$ is the frequency difference between the two optical modes. Additionally, we can assume that the change in the optical mode is adiabatic in the motion of the dielectric, $\Delta\omega \gg \omega_\mathrm{m}$, to finally write:

$$G_2 \simeq -\frac{4g_1^2}{\Delta\omega}. \tag{3.47}$$

---

[6] Notice that ω_m in the exponent of $\hat{b}(t)$ should be modified to take into account the frequency shift from the optical feedback.

[7] When we plug the solutions of Eqs. (3.43c) and (3.43d) into Eq. (3.43b), there are additional frequency shift and decay that are independent on the mechanical state. Generally, these are small compared to the intrinsic optical ones, and can be neglected. Otherwise, they can be taken into account by redefining ω_e and γ_e.

While G_2 cannot diverge by setting $\Delta\omega \to 0$ [see Eq. (3.46)], its value changes substantially by going from the weak to the strong dielectric limit. This can be understood by looking at Figs. 3.2, 3.5 and 3.6, from which it is clear that by incrementing ϵ_r we reduce $\Delta\omega$ and increase g_1 (up to a constant).

With the tools developed in sections 3.1.2 and 3.1.3, we can quantify the parameter G_2 both in the weak and strong dielectric limit. Recalling that we are basing our analysis on a strongly driven even mode and the next odd one, G_2 becomes, in the two considered regimes ($z_0 = L/2$):

$$G_2 = \frac{c d_\mathrm{p}^2 x_\mathrm{z}^2 \tilde{k}_\mathrm{e}^3 \tilde{k}_\mathrm{o}}{\pi L}\epsilon_\mathrm{r}^2 \qquad \text{for } \epsilon_\mathrm{r} d_\mathrm{p} k \ll 2, \tag{3.48a}$$

$$G_2 = \frac{c d_\mathrm{p} x_\mathrm{z}^2 \tilde{k}_\mathrm{e}^3}{L}\epsilon_\mathrm{r} \qquad \text{for } \epsilon_\mathrm{r} d_\mathrm{p} k \gg 2. \tag{3.48b}$$

Above, we defined $\tilde{k}_\mathrm{e}$ and $\tilde{k}_\mathrm{o}$ to be the unperturbed wave vectors of the even and odd optical modes, respectively. In Fig. 3.7, the induced quadratic coupling is plotted as a function of the polarizability ϵ_r. The dashed lines are Eqs. (3.48), while the solid one is derived by computing the linear coupling g_1 and the frequency difference $\Delta\omega$ with the exact method outlined above. We stress that Fig. 3.7 is derived considering only two optical modes. As motivated below, this is an excellent approximation in the strong dielectric regime, but a poor one in the opposite limit. As a consequence of that, the two dashed lines do not cross at $\epsilon_\mathrm{r} = 2/[d_\mathrm{p}k]$ as expected, but for a slightly higher value of ϵ_r. In fact, the estimate of G_2 for the small coupling regime in Eq.(3.48a) is incomplete, as it misses all contributions from other frequencies.

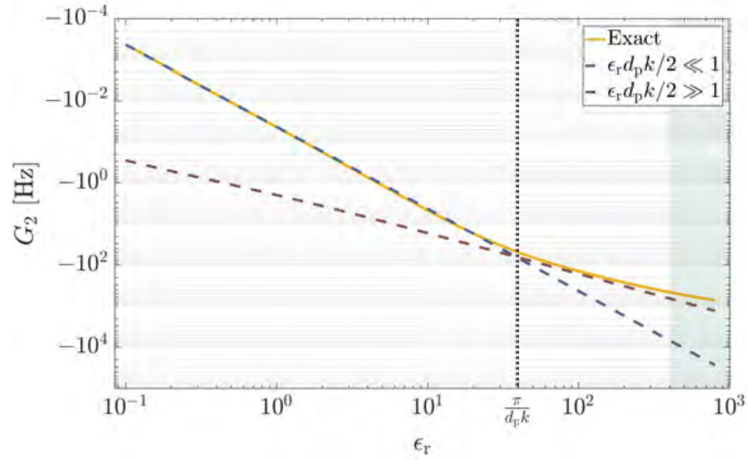

FIGURE 3.7: Induced quadratic coupling G_2 as a function of the dielectric polarizability ϵ_r. The solid lines is derived by numerically solving Maxwell equations, while the dashed lines are the analytical results for the strong [dark red, Eq. (3.48b)] and weak [blue, Eq. (3.48a)] dielectric limit, respectively. The green shadowed region is identified by $d_\mathrm{p}\sqrt{1+\epsilon_\mathrm{r}} \geq \lambda/4$. We chose $\lambda = 4$ μm, $L = 60$ μm, and $d_\mathrm{p} = 50$ nm.

Generalizing the previous results to infinite optical modes is trivial, considering that only odd modes are linearly coupled to a specific even one. Thus, in the same scenario with a strongly driven even optical mode, we find the total induced quadratic coupling G_2 by summing Eq. (3.45) over all different frequencies ω_{2j+1}.

However, this is in practice not required, as in the weak dielectric limit g_2 dominates [see Eqs. (3.48a) and (3.37b)][8], and in the opposite regime only a single odd mode contributes [see Eqs. (3.47) and (3.19a)]. The picture where only two optical modes are considered is thus sufficient to describe the induced quadratic coupling G_2.

In the remaining part of this section, we find the total quadratic coupling between any optical mode and the mechanical motion. Thereby, we confirm the results presented in Refs. [78, 45], according to which the induced quadratic coupling is preponderant in the strong dielectric limit. This can be done by numerically determining the modes frequencies ω_i as a function of the membrane position z_0, and from that extract $\partial^2_{z_0}\omega_i(z_0) \propto g_2 + G_2$. In Fig. 3.8 (left), we can see that in the strong dielectric limit the two mode approximation is indeed excellent. In particular, the numeric confirms that the frequencies of the even (green) and odd (blue) modes follow the dispersion relations of the dressed states of a two level system:

$$\omega_\mathrm{e}(z_0) = \frac{\omega_\mathrm{e} + \omega_\mathrm{o}}{2} - \sqrt{\frac{4g_1^2}{x_\mathrm{z}^2}\left(z_0 - \frac{L}{2}\right)^2 + \frac{\Delta\omega^2}{4}}, \tag{3.49a}$$

$$\omega_\mathrm{o}(z_0) = \frac{\omega_\mathrm{e} + \omega_\mathrm{o}}{2} + \sqrt{\frac{4g_1^2}{x_\mathrm{z}^2}\left(z_0 - \frac{L}{2}\right)^2 + \frac{\Delta\omega^2}{4}}. \tag{3.49b}$$

In other words, in the strong dielectric limit the induced quadratic coupling G_2 is dominant, and the intrinsic one negligible. This is also confirmed by the two plots on the right of Fig. 3.8. In the upper one, we present the ratio between the total quadratic coupling $\partial^2_{z_0}\omega_i(z_0)$ and the intrinsic quadratic coupling G_2. In the lower one, the solid line represents the total quadratic coupling, while the dashed lines the analytical results for the weak and strong dielectric limit, Eqs. (3.37b) and (3.48b) respectively.

3.2.4 Bogoliubov method

To conclude the setup characterization, and confirm our analytical predictions, we present another numerical approach. This method is based on the Bogoliubov transformations and is described in Ref. [100]. The idea is beautifully simple. We start with the cavity without the membrane, such that the optical field is described by the unperturbed relations of Eq. (3.14). Then, we imagine that a membrane suddenly appears into the cavity, perturbing the electric field inside. The optical system Hamiltonian becomes off diagonal, as in Eq. (3.24), with the off diagonal terms being given by Eq. (3.35). Without any approximation taken so far, we can diagonalize the Hamiltonian and recover the results obtained by directly solving Maxwell equations in section 3.1.1. This is indeed confirmed by Fig. 3.9 (left), where the frequencies of the different modes are presented, as a function of ϵ_r. The predictions given by solving the Maxwell equations (dashed lines) agree with the Hamiltonian diagonalization (dots). Another confirmation is given in Fig. 3.9 (bottom right), where the electric field is plotted nearby the dielectric. Diagonalizing the Hamiltonian, we also access the unitary transformation that switches the basis from the unperturbed one to the exact one. This unitary transformation can be applied to the optomechanical interaction of Eq. (3.32) [with the $g_n[i,j]$ given in Eq. (3.34)], to find exact values

---

[8] In principle we need to show this, since in the weak dielectric limit there are several contributions to G_2. We do not formally prove $G_2 \ll g_2$ in this manuscript. However, we give a small hint: the procedure involves a converging sum, such as the one discussed in section 3.3.2. Numerical results confirm that $G_2 \ll g_2$ in the weak dielectric limit.

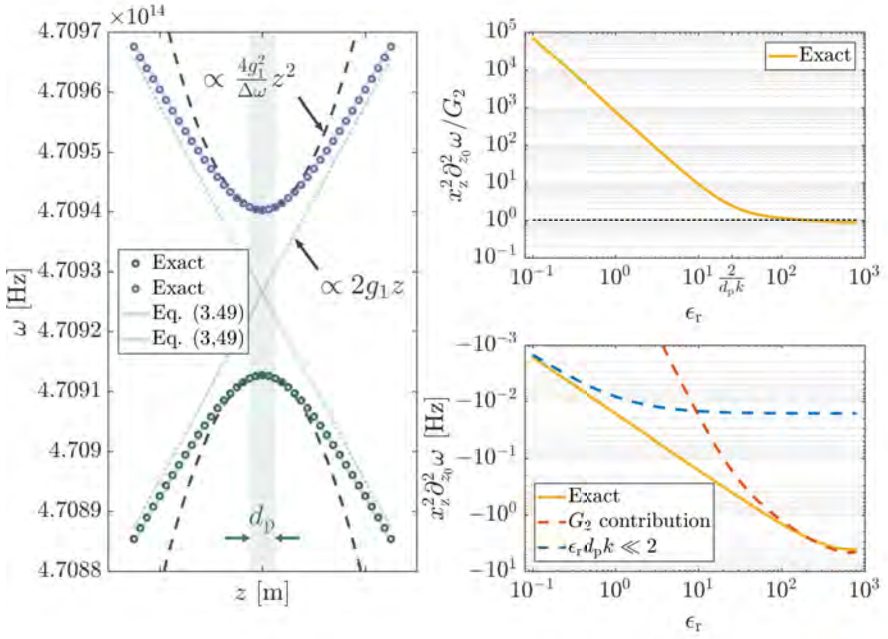

FIGURE 3.8: Intrinsic and induced contributions to the quadratic coupling. In the **left** plot, the analytical prediction for a two modes optomechanical system are compared with exact numerical results. The solid lines are Eqs. (3.49), and are confirmed by the dots representing the numerical results. We chose $\epsilon_\mathrm{r} = 100$, such that we are in the strong coupling regime. In the **right** plots, we compare the total quadratic coupling, obtained by numerically solving Maxwell equations at different positions of the dielectric, with the intrinsic and induced contributions. In particular, in the **right, upper** plot we show that the induced coupling is dominant for strong dielectric, while in the **right, lower** plot we show the different contributions (dashed lines) to the total coupling (solid line). For all figures, we chose $L = 6$ mm, $d_\mathrm{p} = 50$ nm, and $\lambda = 4$ μm.

for the couplings in the exact basis. Again, since the couplings in Eq. (3.34) are exact, the values found with this method resemble the real ones. This is indeed confirmed by Fig. 3.9 (top right), where the linear couplings obtained by exactly solving the Maxwell equations are compared with the ones derived with the Bogoliubov method.

There are two main limitations in using the Bogoliubov transformations for diagonalizing the Hamiltonian in Eq. (3.24). First, for the optical regime in which we are mostly interested, the wave index is usually high, and the discontinuity introduced by a strong dielectric large. It follows that the number of modes required to have a satisfactory convergence becomes just too big. If, by writing better algorithms[9], the convergence could be faster, the limit $2d_\mathrm{p}\sqrt{1+\epsilon_\mathrm{r}} \ll \lambda$ imposes a lower bound on the number of modes to be considered. This is why we took such a large ratio d_p/L in Fig. 3.9. The second, more practical, limitation, is the insufficient precision in the diagonalization procedure. We noticed that, by increasing the dimension of the system, the error increases. With this, we mean that the Bogoliubov transformation is not perfectly unitary, despite the method imposes that. While, in principle,

---

[9] The writer of this manuscript is not a champion in algorithm optimization.

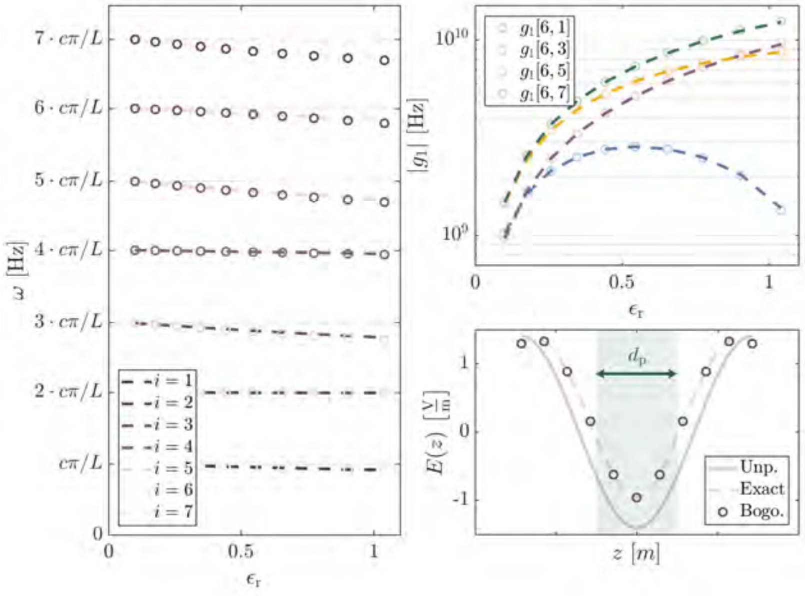

FIGURE 3.9: Comparison between the numerical results obtained by solving Maxwell equations (dashed lines), and the Bogoliubov diagonalization of the Hamiltonian (dots). In the **left** plot, the wave vectors are compared. In the **right, upper** plot, the linear couplings, and in the **right, lower** one the spatial envelope of the seventh mode of the electric field. For all figures, we chose $L = 0.5$ μm, and $d_p = 50$ nm.

this problem could be removed by increasing the precision of our computer, it still limits the maximum accuracy we can possibly get numerically.

3.3 Mechanical heating rate

In the previous sections, we derived all relevant parameters for describing the system. In the following, we find the heating rate $\Delta n_b/T$. As seen for the electromechanical setup, there are two contributions to Δn_b: the multimode and the parasitic ones described, respectively in Eqs. (2.65) and (2.68). Here, for simplicity, we only consider the first one. The parasitic contribution can be found with the results in section 2.2.1.

In Fig. 3.10 we draw a scheme of the considered system. A multitude of optical modes $\hat{a}_i$ lives within the cavity, and is coupled with two reservoirs of modes $\hat{A}_{L,i}$ and $\hat{A}_{R,i}$ through left and right mirrors, respectively. The in/out couplings $\gamma_L[i,j]$ and $\gamma_R[i,j]$ are determined by fabrication, and are generally difficult to control. Since the two reservoirs are shared by all modes $\hat{a}_i$, we start by considering the optical subsystem only. Later on, we include the mechanics to find Δn_b. In this way, we include interferences between all possible paths through which the optical system can decay or be excited.

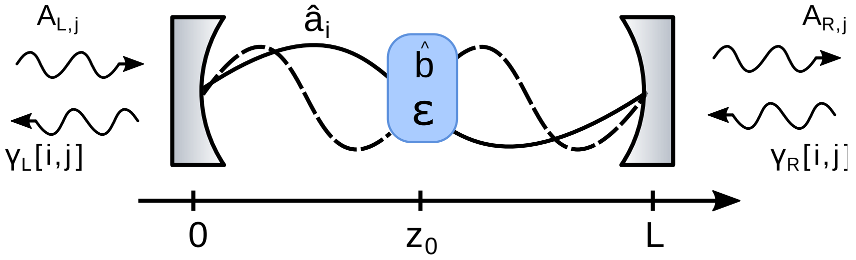

FIGURE 3.10: The optical setup used for determining $\Gamma_{0\to 1}$. The same of Fig. 3.1, the membrane is placed at $z_0 = L/2$ and the relevant modes used in the derivation of $\Gamma_{0\to 1}$ are reported. The mechanical motion is described by $\hat{b}^{(\dagger)}$, while the optical modes by $\hat{a}_i^{(\dagger)}$. The modes $\hat{A}_{\mathrm{L},j}$ and $\hat{A}_{\mathrm{R},j}$ of the left and right optical reservoirs are coupled to $\hat{a}_i$ through $\gamma_{\mathrm{L}}[i,j]$ and $\gamma_{\mathrm{R}}[i,j]$, respectively.

The optical and reservoir Hamiltonians, $\hat{H}_{\mathrm{o}}$ and $\hat{H}_{\mathrm{r}}$ respectively, are given by:

$$\hat{H}_{\mathrm{o}} = \hbar \sum_i \omega_i \hat{a}_i^\dagger \hat{a}_i, \tag{3.50a}$$

$$\hat{H}_{\mathrm{r}} = \hbar \sum_j \Omega_j \hat{A}_{\mathrm{L},j}^\dagger \hat{A}_{\mathrm{L},j} + \hbar \sum_j \Omega_j \hat{A}_{\mathrm{R},j}^\dagger \hat{A}_{\mathrm{R},j}, \tag{3.50b}$$

where we only consider the diagonal part of $\hat{H}_{\mathrm{o}}$, without the last cross terms in Eq. (3.24). In other words, here, we consider the perturbed modes given by either solving Maxwell's equation, or applying the Bogoliubov transformation. The interaction Hamiltonian $\hat{H}_{\mathrm{r,o}}$ between the system and the reservoir can be written as

$$\hat{H}_{\mathrm{r,o}} = \hbar \sum_{i,j} \sqrt{\gamma_{\mathrm{L}}[i,j]} \left(\hat{A}_{\mathrm{L},j}^\dagger \hat{a}_i + h.c. \right) + \hbar \sum_{i,j} \sqrt{\gamma_{\mathrm{R}}[i,j]} \left[(-1)^i \hat{A}_{\mathrm{R},j}^\dagger \hat{a}_i + h.c. \right], \tag{3.51}$$

where $\gamma_{\mathrm{L}}[i,j]$ ($\gamma_{\mathrm{R}}[i,j]$) couples the i-th mode in the cavity with the j-th mode of the left (right) reservoir. The factor $(-1)^j$ comes from the envelope of the field $\hat{a}_i$ at the right mirror, and follows from symmetry considerations. The equations of motion for the Hamiltonian $\hat{H}_{\mathrm{o}} + \hat{H}_{\mathrm{r}} + \hat{H}_{\mathrm{r,o}}$ are

$$\dot{\hat{a}}_i = -i\omega_i \hat{a}_i - i \sum_j \left[\sqrt{\gamma_{\mathrm{L}}[i,j]} \hat{A}_{\mathrm{L},j} + (-1)^i \sqrt{\gamma_{\mathrm{R}}[i,j]} \hat{A}_{\mathrm{R},j} \right], \tag{3.52a}$$

$$\dot{\hat{A}}_{\mathrm{L},j} = -i\Omega_j \hat{A}_{\mathrm{L},j} - i \sum_i \sqrt{\gamma_{\mathrm{L}}[i,j]} \hat{a}_i, \tag{3.52b}$$

$$\dot{\hat{A}}_{\mathrm{R},j} = -i\Omega_j \hat{A}_{\mathrm{R},j} - i \sum_i (-1)^i \sqrt{\gamma_{\mathrm{R}}[i,j]} \hat{a}_i. \tag{3.52c}$$

These last two equations can be formally integrated to give

$$\hat{A}_{\mathrm{L},j}(t) = \hat{A}_{\mathrm{L},j}(-\tau) e^{-i\Omega_j (t+\tau)} - i \sum_i \int_{-\tau}^{t} dt_1 \sqrt{\gamma_{\mathrm{L}}[i,j]} \hat{a}_i(t_1) e^{-i\Omega_j (t-t_1)}, \tag{3.53a}$$

$$\hat{A}_{\mathrm{R},j}(t) = \hat{A}_{\mathrm{R},j}(-\tau) e^{-i\Omega_j (t+\tau)} - i \sum_i (-1)^i \int_{-\tau}^{t} dt_1 \sqrt{\gamma_{\mathrm{L}}[i,j]} \hat{a}_i(t_1) e^{-i\Omega_j (t-t_1)}, \tag{3.53b}$$

where τ is an arbitrary time, generally longer that the cavity's lifetime. Plugging Eqs. (3.53) into Eq. (3.52a) we rewrite the equation of motion for $\hat{a}_i$

$$\begin{aligned}\dot{\hat{a}}_i =& - i\omega_i\hat{a}_i - \frac{\gamma_\mathrm{L}[i,i] + \gamma_\mathrm{R}[i,i]}{2}\hat{a}_i - \overbrace{\sum_{j\neq i}\frac{\sqrt{\gamma_\mathrm{L}[i,j]\gamma_\mathrm{L}[j,j]} + (-1)^{i+j}\sqrt{\gamma_\mathrm{R}[i,j]\gamma_\mathrm{R}[j,j]}}{2}\hat{a}_j}^{\simeq 0} \\ & - i\sum_j\left[\sqrt{\gamma_\mathrm{L}[i,j]}\hat{A}_{\mathrm{L},j}(-\tau)e^{-i\Omega_j(t+\tau)} + (-1)^i\sqrt{\gamma_\mathrm{R}[i,j]}\hat{A}_{\mathrm{R},j}(-\tau)e^{-i\Omega_j(t+\tau)}\right],\end{aligned} \tag{3.54}$$

where we used Markov approximation and ignored the Lamb shift (that can be included in the frequencies ω_i). As highlighted in this last equation, we neglect the additional couplings introduced by the interferences between the system modes. While this is generally a good approximation, since the detuning between different modes is big, in our case may not be. In fact, the leading contribution to Δn_b comes from detuned optical modes, of which one (the even) is strongly driven, the other (the odd) is not. The additional couplings in Eq. (3.54) mix the modes, generally influencing the mechanical heating rate. By carefully looking at the terms in the sum, however, we notice that the couplings vanish between even and odd modes, whenever the mirrors are identical: $\gamma_\mathrm{L}[i,j] = \gamma_\mathrm{R}[i,j]$. This is crucial, since we require the membrane to be at a node (or an anti-node) of the relevant modes to suppress any linear coupling by symmetry. This condition is ensured at $z_0 = L/2$, if there is no mixing of even and odd terms. The residual (weak) coupling of modes of the same parity can then be included as a minor modification. On the other hand, if the mirrors do not have the same decay rates, the position of the membrane should be adjusted to ensure a vanishing linear coupling due to the admixture of even and odd modes (including the Lamb shift contribution). For simplicity, we ignore this small shift and restrict ourselves to the situation corresponding to equal decay rates $\gamma_\mathrm{L}[i,j] = \gamma_\mathrm{R}[i,j] = \gamma[i,j]/2$.

From Eq. (3.54), it is possible to understand how interferences between different decay paths suppress the mechanical heating. Since the operators $\hat{A}_{\mathrm{L},j}$ and $\hat{A}_{\mathrm{R},j}$ are shared between all modes $\hat{a}_i$, the mechanics can be excited through different optical paths, that can interfere destructively. We formally solve the differential equation (3.54), the solution of which will be used later to find the heating rate $\Delta n_\mathrm{b}/T$:

$$\begin{aligned}\hat{a}_i(t) =& \hat{a}_i(-\tau)e^{-\left(i\omega_i+\frac{\gamma_i}{2}\right)(t+\tau)} - i\sum_j\sqrt{\frac{\gamma[i,j]}{2}}\int_{-\tau}^{t}dt_1\hat{A}_{\mathrm{L},j}(-\tau)e^{-i\Omega_j(t_1+\tau)}e^{-\left(i\omega_i+\frac{\gamma_i}{2}\right)(t-t_1)} \\ & - i\sum_j(-1)^i\sqrt{\frac{\gamma[i,j]}{2}}\int_{-\tau}^{t}dt_1\hat{A}_{\mathrm{R},j}(-\tau)e^{-i\Omega_j(t_1+\tau)}e^{-\left(i\omega_i+\frac{\gamma_i}{2}\right)(t-t_1)}.\end{aligned} \tag{3.55}$$

Here, we have defined the total decay for the $i-th$ mode $\gamma_i = 2\gamma[i,i]$.

With the optical system completely characterized, we now include the membrane's dynamics, to determine the heating rate. The interaction between the membrane and the optical modes inside the cavity is described by the Hamiltonian in Eq. (3.32). Since this interaction is extremely weak, we restrict ourselves to first and second order expansions in the mechanical position, such that:

$$\begin{aligned}\hat{H}_\mathrm{int} =& \hbar\sum_{i,j}g_1[i,j]\left(\hat{a}_i + \hat{a}_i^\dagger\right)\left(\hat{a}_j + \hat{a}_j^\dagger\right)\left(\hat{b} + \hat{b}^\dagger\right) \\ & + \hbar\sum_{i,j}\frac{g_2[i,j]}{2}\left(\hat{a}_i + \hat{a}_i^\dagger\right)\left(\hat{a}_j + \hat{a}_j^\dagger\right)\left(\hat{b} + \hat{b}^\dagger\right)^2.\end{aligned} \tag{3.56}$$

We recall that the couplings $g_1[i,j]$ and $g_2[i,j]$ can always be determined numerically using the approaches described in section 3.2 (see Fig. 3.6, 3.7 and 3.8). Moreover, we have simple expressions for both the weak and strong coupling regimes. For $\epsilon_\mathrm{r} d_\mathrm{p} k \ll 2$, they are given by Eqs. (3.37). On the other side, for $\epsilon_\mathrm{r} d_\mathrm{p} k \gg 2$, the linear couplings are given in Eq. (3.42), while the quadratic ones are the induced G_2 given in Eq. (3.47). In this strong dielectric limit, the two mode description (even and next odd one) is sufficient, and the quadratic coupling is dominated by the induced one G_2. To avoid confusion, in the remainder of this chapter we do not further specify whether the quadratic coupling is the intrinsic or the induced one. It will always be the total contribution.

Being interested in the heating of the mechanical system, we neglect the quadratic couplings ($g_1 \gg g_2$) so that, in the resolved sideband regime $\omega_\mathrm{m} \gg \gamma_i$, we can ignore the sidebands coming from $\hat{b}^\dagger \hat{b}^\dagger$ and $\hat{b}\hat{b}$. The remaining term proportional to $\hat{b}^\dagger \hat{b}$ does not lead to heating. The Hamiltonian then becomes

$$\hat{H}_\mathrm{int} = \hbar \sum_{i,j} g_1[i,j] \left(\hat{a}_i + \hat{a}_i^\dagger\right) \left(\hat{a}_j + \hat{a}_j^\dagger\right) \left(\hat{b} + \hat{b}^\dagger\right), \tag{3.57}$$

and we recall that the membrane is described by $\hat{H}_\mathrm{m} = \hbar\omega_\mathrm{m} \hat{b}^\dagger \hat{b}$. As a consequence of symmetry, the linear interaction couples an even and an odd optical modes with the membrane's position. The Hamiltonian in Eq. (3.57) can thus be rewritten as

$$\hat{H}_\mathrm{int} = \hbar \sum_{i,j} g_1[2i, 2j+1] \left(\hat{a}_{2i}\hat{a}_{2j+1}^\dagger + \hat{a}_{2i}^\dagger \hat{a}_{2j+1}\right) \left(\hat{b} + \hat{b}^\dagger\right), \tag{3.58}$$

where we used the RWA: $(\hat{a}_i + \hat{a}_i^\dagger)(\hat{a}_j + \hat{a}_j^\dagger) \simeq \hat{a}_i \hat{a}_j^\dagger + \hat{a}_i^\dagger \hat{a}_j$.

Assuming that only one even mode is driven, we linearise it such that $\hat{a}_e^{(\dagger)}(t) \to \alpha_\mathrm{e}^{(*)}(t) + \hat{\delta a}_e^{(\dagger)}(t)$, for a certain even index e. If the drive is strong enough, a good approximation is to only include terms which are enhanced by the strong drive. Eq. (3.58) then becomes

$$\begin{aligned} \hat{H}_\mathrm{int}(t) =& \hbar \sum_j g_1[e, 2j+1] \left(\tilde{\alpha}_\mathrm{e} \hat{a}_{2j+1}^\dagger(t) e^{-i\omega_\mathrm{e} t} + \tilde{\alpha}_\mathrm{e}^* \hat{a}_{2j+1}(t) e^{i\omega_\mathrm{e} t}\right) \left(\hat{b} + \hat{b}^\dagger\right) \\ =& \hat{F}(t) \left(\hat{b} + \hat{b}^\dagger\right), \end{aligned} \tag{3.59}$$

where we have explicitly written the time dependency of $\alpha_\mathrm{e}(t) = \tilde{\alpha}_\mathrm{e} e^{-i\omega_\mathrm{e} t}$. In analogy to the electromechanical case, we consider the situation in which the even mode is continuosly driven at its resonant frequency, such that $\tilde{\alpha}_\mathrm{e} \simeq i\alpha/\sqrt{T\gamma_\mathrm{e}}$, with $|\alpha|^2$ the number of photons sent into the cavity during the probe duration T. Using the Fermi Golden Rule, the heating rate $\Delta n_\mathrm{b}/T$ is found to be

$$\frac{\Delta n_\mathrm{b}}{T} = \frac{1}{\hbar^2} \left\langle \hat{F}\hat{F} \right\rangle_{-\omega_\mathrm{m}}, \tag{3.60}$$

where $\hat{F}$ is the optical part of the interaction Hamiltonian in Eq. (3.59), and $\left\langle \hat{F}\hat{F} \right\rangle_\Omega$ the Fourier transform

$$\left\langle \hat{F}\hat{F} \right\rangle_\Omega = \int_{-\infty}^{\infty} dt e^{i\Omega t} \left\langle \hat{F}(t)\hat{F}(0) \right\rangle. \tag{3.61}$$

To compute $\left\langle \hat{F}\hat{F}\right\rangle_{-\omega_{\mathrm{m}}}$, we explicitly write down $\left\langle \hat{F}(t)\hat{F}(0)\right\rangle$

$$\begin{aligned}\left\langle \hat{F}(t)\hat{F}(0)\right\rangle = \hbar^2 \sum_{i,j} g_1[e,2i+1]g_1[e,2j+1]\Big\langle & \left(\tilde{\alpha}_{\mathrm{e}}\hat{a}^{\dagger}_{2i+1}(t)e^{-i\omega_{\mathrm{e}}t} + \tilde{\alpha}^{*}_{\mathrm{e}}\hat{a}_{2i+1}(t)e^{i\omega_{\mathrm{e}}t}\right) \\ & \times \left(\tilde{\alpha}_{\mathrm{e}}\hat{a}^{\dagger}_{2j+1}(0) + \tilde{\alpha}^{*}_{\mathrm{e}}\hat{a}_{2j+1}(0)\right) \Big\rangle,\end{aligned} \tag{3.62}$$

where the time evolution of the operators $\hat{a}_i$ is described by Eq. (3.55). Ignoring non contributing terms[10], we simplify the product within the brackets in Eq. (3.62):

$$\left\langle \left|\tilde{\alpha}_{\mathrm{e}}\right|^2 \hat{a}^{\dagger}_{2i+1}(t)\hat{a}_{2j+1}(0)e^{-i\omega_{\mathrm{e}}t} + \left|\tilde{\alpha}_{\mathrm{e}}\right|^2 \hat{a}_{2i+1}(t)\hat{a}^{\dagger}_{2j+1}(0)e^{i\omega_{\mathrm{e}}t}\right\rangle, \tag{3.63}$$

We ignore the state of the optical fields inside the cavity at the initial time $-\tau$ (this is equivalent to saying that our system does not have infinite memory), and impose the noise correlators:

$$\left\langle \hat{A}_{\mathrm{L},i}(-\tau)\hat{A}^{\dagger}_{\mathrm{L},j}(-\tau)\right\rangle = \delta_{i,j}, \tag{3.64a}$$

$$\left\langle \hat{A}_{\mathrm{R},i}(-\tau)\hat{A}^{\dagger}_{\mathrm{R},j}(-\tau)\right\rangle = \delta_{i,j}. \tag{3.64b}$$

All other correlators are zero, if we assume the average thermal occupation to be null at the relevant optical frequencies. Putting all together, we find the optomechanical heating rate

$$\frac{\Delta n_{\mathrm{b}}}{T} = \left|\tilde{\alpha}_{\mathrm{e}}\right|^2 \left| \sum_j \frac{g_1[e,2j+1]\sqrt{\gamma[2j+1,e-m]}}{i\left(\omega_{2j+1}-\omega_{\mathrm{e}}+\omega_{\mathrm{m}}\right) + \frac{\gamma[2j+1,2j+1]}{2}} \right|^2, \tag{3.65}$$

where the index m refers to the mechanical frequency ω_{m}. Before proceeding, let us comment on this result. First, the contributions from the counter rotating terms, that we have ignored with the RWA, would appear in Eq. (3.65) as additional terms in the sum. These would have denominators $i\left(\omega_{2j+1}+\omega_{\mathrm{e}}\pm\omega_{\mathrm{m}}\right)+\gamma[2j+1,2j+1]/2$, which are separated by large optical frequencies and can be neglected. In other words, the terms for which the RWA does not apply, do not contribute to the heating. While this result looks obvious, it is not. At first sight, the terms of the sum in Eq. (3.65) scale as one over the frequency difference. This results in a logarithmic divergence with significant contributions from highly off-resonant terms, where the RWA is questionable. However, the convergence is ensured by interferences between optical modes[11], hidden in factors $(-1)^j$ inside the couplings $g_1[e,2j+1]$. This means that there is only a neighbour of frequencies around ω_{e} that effectively contributes to the mechanical heating, and for these the RWA is justified (see Fig. 3.11, top right). Second, we assumed that there are no thermal photons at the relevant frequencies. While this assumption is legit, their contribution can be included in an overall factor $(1+2\bar{n}_{\mathrm{e}})$ multiplying the whole rate. To be annoyingly precise, the number of average thermal photons in the reservoir $\bar{n}_{\mathrm{e}}$ is frequency dependent. For the same reasons explained above, however, an excellent approximation is to consider the thermal photons at the frequency of the driven mode ω_{e}. Finally, internal dissipation can be taken into account by modifying the factors $\gamma[2j+1,2j+1]/2$ in

---

[10] $\hat{a}^{\dagger}_{2i+1}(t)\hat{a}^{\dagger}_{2j+1}(0)$ and $\hat{a}_{2i+1}(t)\hat{a}_{2j+1}(0)$ only contain noise terms which correlators are null [see Eq. (3.64)].

[11] Technically speaking, the finite-size of the dielectric also helps making the sum converging. However, interferences are just much more important.

the denominators of Eq. (3.65), and by including the corresponding contributions. While generally this results in modifications to $\Delta n_\mathrm{b}/T$, in our case it makes practically no difference. In fact, the additional heating coming from the internal dissipation is compensated by a reduced intensity of the optical field inside the cavity. Adding an additional channel does not increase the noise; vacuum is always vacuum. And this is true for atoms, membranes, butterflies and freight trains [101].

In the remainder of this section, we determine simple expressions for the heating rate $\Delta n_\mathrm{b}/T$ in the limits of weak and strong dielectric. We assume that the minimum gap between two optical frequencies is bigger than both the mechanical frequency and the optical decay rate: $|\omega_i - \omega_j| \gg \omega_\mathrm{m}, \gamma[k,l]$ for any i,j,k,l. Moreover, we embrace the shared belief according to which the rates $\gamma[i,j]$ are constant for a wide spectrum, such that $\gamma[i,j] \simeq \gamma$ for any i,j. We thus rewrite Eq. (3.65) in the following way:

$$\frac{\Delta n_\mathrm{b}}{T} = |\tilde{\alpha}_\mathrm{e}|^2 \gamma \left(\sum_j \frac{g_1[e,2j+1]}{\Delta\omega_{2j+1}} \right)^2, \tag{3.66}$$

where $\Delta\omega_{2j+1} = \omega_{2j+1} - \omega_\mathrm{e}$.

3.3.1 Optomechancial heating rate in the strong dielectric limit

In the strong dielectric limit, the denominator $\Delta\omega_{2j+1}$ in Eq. (3.66) almost vanishes for the next odd mode $2j+1 = e+1$ (see Fig. 3.2 and section 3.1.3). For all other indices j, the contribution to the series is negligible [see Fig. 3.11 (top right)]. We thus approximate the rate $\Delta n_\mathrm{b}/T$ with

$$\frac{\Delta n_\mathrm{b}}{T} \simeq |\tilde{\alpha}_\mathrm{e}|^2 \gamma \left(\frac{g_1[e,2j+1]}{\Delta\omega_{e+1}} \right)^2 \xrightarrow{\text{Eqs.(3.19),(3.42)}} \frac{d_\mathrm{p}^2 x_\mathrm{z}^2 |\alpha|^2}{16T} \frac{\omega_\mathrm{e}^4}{c^4} \epsilon_\mathrm{r}^2, \tag{3.67}$$

where we substituted the average intracavity photons $\tilde{\alpha}_\mathrm{e}$ with the expression

$$\tilde{\alpha}_\mathrm{e} = \frac{i\alpha}{\sqrt{T\gamma}}. \tag{3.68}$$

We recall that $|\alpha|^2$ is the total number of photons sent during the probing time T. This substitution is for consistency with the notation introduced in chapter 2.

3.3.2 Optomechancial heating rate in the weak dielectric limit

Deriving a practical expression for the heating rate $\Delta n_\mathrm{b}/T$ in the weak dielectric limit is slightly more involved, since we cannot consider only one contribution in the sum in Eq. (3.66). We start by recalling that the linear couplings $g_1[e, e+2j+1]$ are given in Eq. (3.37a), such that:

$$\frac{\Delta n_\mathrm{b}}{T} = \epsilon_\mathrm{r}^2 \frac{d_\mathrm{p}^2 x_\mathrm{z}^2 |\alpha|^2}{4TL^2} \frac{\omega_\mathrm{e}^3}{c^2} \left(\sum_j \frac{(-1)^j \sqrt{\omega_{e+2j+1}}}{\Delta\omega_{2j+1}} \right)^2. \tag{3.69}$$

This equation shows the power of interference. Different decay paths interfere destructively, making the sum convergent and thus reducing the mechanical heating. This can be understood in Fig. 3.11 (top right, blue line), where Eq. (3.69) is evaluated for different numbers of contributions j. In particular, on the $\underline{x}$ axis there are the number of contributions, in pairs, around the even index 'e'. By taking only the two terms $e \pm 1$, we overestimate the heating. The next odd pair $e \pm 3$ partially corrects the result, that converges to within 10% of the real value in few other iterations. Another way to understand this behaviour, we can think at the modes in the optical field, and at the force that they exert on the membrane. From physical consideration, this force is proportional to the electric field difference at the interfaces of the dielectric [see Eq. (3.41)]. And since the odd modes switch sign by increasing the index, it follows that half of them push, half pull the membrane, such that the resulting force is a compromise between these two contributions.

We rewrite Eq. (3.69) by approximating $\sqrt{\omega_{e+2j+1}} \simeq \sqrt{\omega_{e+1}}$. This is justified, since optical frequencies are generally characterized by high indices. Recalling that $\Delta\omega_{2j+1} = c\pi(2j+1)/L$, we get:

$$\frac{\Delta n_{\mathrm{b}}}{T} = \epsilon_{\mathrm{r}}^2 \frac{d_{\mathrm{p}}^2 x_{\mathrm{z}}^2 |\alpha|^2}{4TL^2} \frac{\omega_{\mathrm{e}}^3}{c^2} \left(\sqrt{\omega_{e+1}} \frac{L}{c\pi} \overbrace{\sum_j \frac{(-1)^j}{2j+1}}^{=\pi/2} \right)^2 = \frac{d_{\mathrm{p}}^2 x_{\mathrm{z}}^2 |\alpha|^2}{16T} \frac{\omega_{\mathrm{e}}^3 \omega_{e+1}}{c^4} \epsilon_{\mathrm{r}}^2, \tag{3.70}$$

where $\omega_{e+1} \simeq \omega_{\mathrm{e}}$ (for the same reason explained above). Quite surprisingly, the weak and strong dielectric limits in Eqs. (3.67) and (3.70) give almost the same expression, even though they are derived in completely different limits. We stress that interferences between the electric fields at the edges of the membrane cancel the divergence of the sum. For getting this result, we assumed that all modes share the same reservoir, with identical couplings. Other scenarios could be interesting to investigate, to see whether it is possible to reduce the optomechanical heating. The trivial case of each mode talking to an independent reservoir, for instance, is a horrible, horrible idea. It eliminates the field interferences and increases the heating[12]. Fortunately, such scenario is not the typical situation in practice.

---

[12] Notice that, even in this case, the sum over all optical modes is still convergent. This is due to the fact that, outside the limit $2d_{\mathrm{p}}\sqrt{1+\epsilon_{\mathrm{r}}} \ll \lambda$, Eq. (3.37a) ceases to be valid and the linear couplings $g_1[e, 2j+1]$ are reduced.

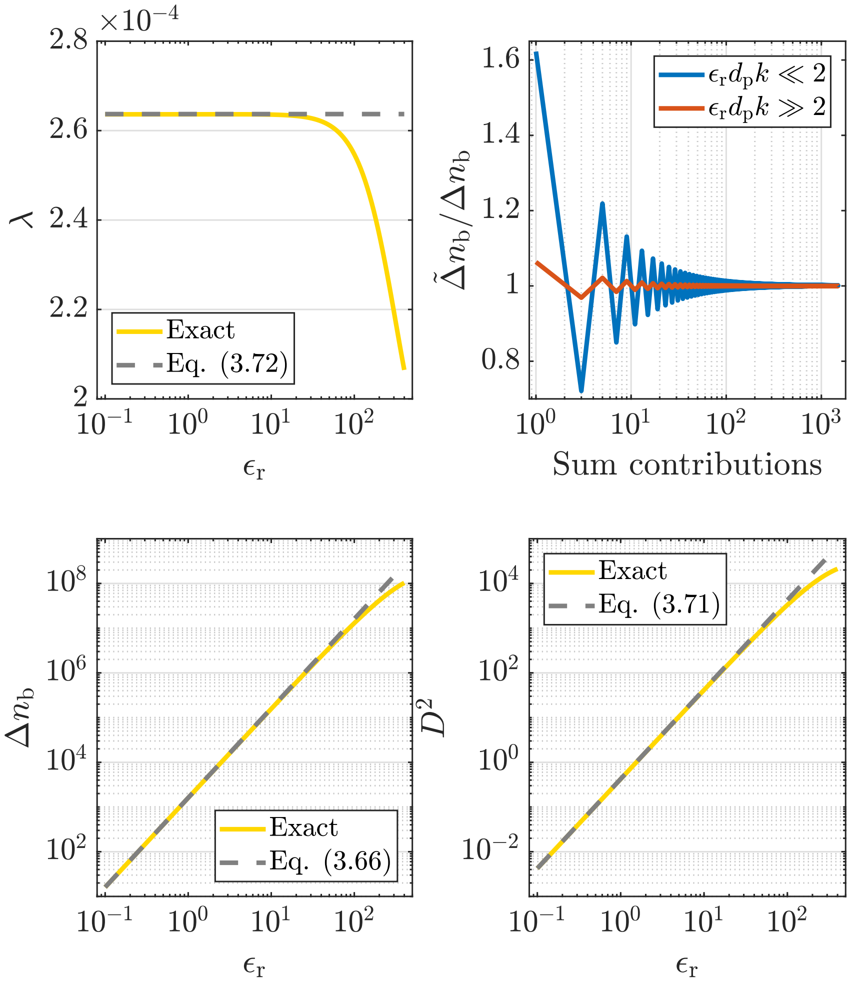

FIGURE 3.11: λ and other relevant parameters for the phonon QND measurement. In the **upper, left** plot, we compare the numerical values for λ (solid line) with the analytical prediction of Eq. (3.73) (dashed line). In the **upper, right** plot, we investigate the convergence of the sum in Eq. (3.69) in the weak (blue, $\epsilon_r = 0.1$) and strong (red, $\epsilon_r = 100$) dielectric regime. $\tilde{\Delta n}_b$ is the value of the parameter Δn_b in Eq. (3.65), with the sum evaluated up to the associated number of contributions. The heating Δn_b is represented in the **lower, left** figure. The numerical value (solid line) is plotted along with the analytical prediction (dotted line) of Eq. (3.67). In the **lower, right** plot, the parameter D^2 is computed numerically (solid line) and analytically [dashed line, Eq. (3.72)]. For all figures, we set $\lambda = 4$ μm, $L = 6$ mm, $d_p = 50$ nm, $\omega_m = (2\pi)80$ MHz, $\gamma = (2\pi)1.5$ kHz, $|\alpha| = 10^9$, and $x_z = 1.3$ pm.

3.4 The parameter λ and the phonon QND measurement

In the previous section, we determined the heating rate $\Delta n_{\mathrm{b}}/T$. While a general formula is given in Eq. (3.65), practical expressions in the limits of strong and weak dielectric have also been derived, and presented in Eqs. (3.67) and (3.70), respectively. Since the frequencies of the strongly driven even mode and the next odd one are almost identical for typical setups, we assume $\omega_{e+1} = \omega_{\mathrm{e}}$ in the following. As a consequence, the heating rates Δn_{b} in the strong and weak dielectric limit become identical and take the form in Eq. (3.67). Below, we derive the signal to noise ratio D^2 introduced in section 2.1, and the figure of merit for the phonon QND measurement: the parameter λ. We then comment about the two different regimes, and how to improve the experiment.

Following the procedure outlined in section 2.2.1, we determine the signal to noise ratio D^2 for the optomechanical system

$$D^2 = \frac{g_2^2 |\alpha|^2 \gamma_{\mathrm{out}}^2}{\left(\gamma_{\mathrm{out}} + \gamma_{\mathrm{in}}\right)^4}, \tag{3.71}$$

where γ_{out} is the desired outcoupling, and γ_{in} takes into account internal dissipation. Using previous results, we substitute the quadratic coupling g_2 with Eqs. (3.37b) and (3.47), to find simple expressions in the strong and weak dielectric limits. Interestingly, these equations reduce to the same result, such that D^2 becomes

$$D^2 = \frac{d_{\mathrm{p}}^2 x_{\mathrm{z}}^4 \left|\alpha\right|^2}{16\gamma^2 L^2} \frac{\omega_{\mathrm{e}}^6}{c^4} \epsilon_{\mathrm{r}}^2, \tag{3.72}$$

no matter in which regime. Here, to be consistent with the electromechanical case studied in chapter 2, we set $\gamma_{\mathrm{out}} = \gamma_{\mathrm{in}} = \gamma$. Including both D^2 and Δn_{b}, the parameter λ can be derived to be

$$\lambda = \frac{x_{\mathrm{z}}^2 \omega_{\mathrm{e}}^2}{L^2 \gamma^2}, \tag{3.73}$$

both in the strong and weak dielectric limit. For current technology, it is highly challenging to have $\lambda > 1$. As an example, the experiment in Ref. [45], that aims at performing the phonon QND measurement, is characterized by $\lambda \lesssim 10^{-10}$. In Fig. 3.11 (top left), we compare the parameter λ computed numerically with Eq. (3.73). Deviations are to be ascribed to hybridization of the even optical mode, that have not been considered in the theory. For comparison, the mechanical frequency ω_{m} and zero point motion amplitude x_{z} are taken identical to the one used for the electromechanical setup. In the same figure, we show the signal to noise ratio D^2 (bottom right), and the heating Δn_{b} (bottom left).

It is useful to express the parameter λ in different ways, to discover qualitative differences between the weak and strong dielectric limit. The fact that λ is the same in both cases, follows from the particular geometry chosen. In other experiments, it may be advantageous to work in one of the two regimes. In the following section, we highlight which settings have to be tuned to increase λ, to achieve the phonon QND measurement. In particular, we explain why the electromechanical system allows for the QND measurement, while the optomechanical one not. To do so, we start from the general equations for D^2 and Δn_{b} given in Eqs. (3.66) and (3.71), respectively. These have been determined without imposing any constraint from the particular system used[13], and are therefore more general than the membrane–in–the–middle setup of Fig. 3.10.

3.4.1 The parameter λ in the strong dielectric limit

Whenever the condition $\epsilon_r d_p k \gg 2$ is satisfied, the optical modes are strongly hybridized. As such, the frequency difference between the driven even mode ω_e and the next odd one ω_o goes to zero. Therefore, we approximate again the sum in Eq. (3.66) with the single term with index $2j+1 = e+1 = o$, to get

$$\frac{\Delta n_b}{T} = \frac{|\alpha|^2 g_1^2}{T \Delta\omega^2}, \tag{3.74}$$

where $g_1 = g_1[e, o]$. As a consequence of the strong hybridization of the optical modes, the total quadratic coupling is dominated by the induced one G_2 discussed in section 3.2.3, Eq. (3.47). We can thus rewrite the signal to noise rate D^2 in Eq. (3.71) as

$$D^2 = \frac{|\alpha|^2 g_1^4}{\Delta\omega^2 \gamma^2}. \tag{3.75}$$

With this and the heating rate Δn_b in Eq. (3.74), we determine the parameter λ to be

$$\lambda = \frac{g_1^2}{\gamma^2}, \tag{3.76}$$

confirming the results of Ref. [78, 79]. Not surprisingly, we recover the condition according to which strong optomechanical coupling is required to achieve phonon QND measurement. In addition to the literature, here we have developed the tools to demonstrate that the two modes description of the system is rigorous in the strong coupling regime. Motivated by the degeneracy in the even and odd frequencies, our numerical tools confirms this description. Moreover, we give simple expressions for the relevant quantities, that only depend on easily accessible parameters such as the polarizability ϵ_r, the cavity length L and the membrane's width d_p.

3.4.2 The parameter λ in the weak dielectric limit

The strong dielectric limit puts a severe requirement for the phonon QND measurement. The reason is that the frequency difference is directly related to the quadratic coupling, as shown in Eq. (3.47). In the weak dielectric limit, however, the quadratic coupling is completely unrelated from $\Delta\omega$. To get an expression for λ in this regime, we take a reasonable assumption to rewrite the sum in Eq. (3.66). As seen in section 3.3.2, the frequencies contributing to the heating rate Δn_b are numerous. However, the core is centred around the even mode, where the linear couplings are slowly varying. Moreover, interferences of the electric fields play a central role in reducing the heating, such that:

$$\frac{\Delta n_b}{T} = \frac{|\alpha|^2}{T} \left(\sum_j \frac{g_1[e, 2j+1]}{\Delta\omega_{2j+1}} \right)^2 \overset{\dagger}{\simeq} \frac{|\alpha|^2 g_1^2}{T} \left(\frac{\pi}{2\Delta\omega} \right)^2, \tag{3.77}$$

---

[13] For simplicity we still consider the situation in which optical frequencies set the highest scale in the system, and we include internal optical dissipation. Generalizations have been done, but do not add insight to the problem.

where $g_1 = g_1[e, o]$ and $\Delta\omega = \omega_o - \omega_e$. The equality marked with '†' deserves few comments, the first being that it is not quantitatively correct, but gives powerful qualitative insights. The absolute value of the couplings $g_1[e, 2j+1]$ has been taken outside the sum, and assumed approximately equal to $g_1[e, o]$. The symmetry of the system is such that a factor $(-1)^j$ remains inside the sum, as a consequence of interferences between the electric fields. With the frequency differences $\Delta\omega_{2j+1}$ proportional to the indices, the sum converges to $\pi/[2\Delta\omega]$, as seen above in Eq. (3.70). While these assumptions could change from system to system, Eq. (3.77) describes a behaviour that is shared by all setups, and can be used to find an approximate value of the parameter λ. With the signal to noise ratio given in Eq. (3.71), we determine

$$\lambda \simeq \frac{1}{4\pi^2}\left(\frac{g_2}{g_1}\right)^2\left(\frac{\Delta\omega}{\gamma}\right)^2, \tag{3.78}$$

with $g_2 = g_2[e, e]$. This result really shows the potential of fabrication engineering for phonon QND measurement. Moreover, it explains why the electromechanical setup is capable of seeing quantum jumps, while the optical cavity is not. The difference resides in the frequency difference $\Delta\omega = \omega_o - \omega_e$. While the electrical circuit can be designed such that $\Delta\omega \simeq \omega_o \gg \omega_e$, for the optical cavity it is $\Delta\omega = \pi c/L$, a small fraction of ω_e. In fact, by substituting $\Delta\omega$ with ω_o (and imposing $Z_{\text{out}} = R$) in Eq. (3.78), we recover the parameter λ_b in Eq. (2.5b). This result sheds light on how to achieve phonon QND measurement in the optical regime. While the strong dielectric limit remains inconvenient for the reasons discussed above, in the weak dielectric limit we may be successful. However, we need to carefully engineer the system, such that the frequency difference between the even and odd optical modes is big.

3.5 Conclusions

The limit for which the phonon QND measurement can be achieved in the optical cavity of Fig. 3.1, can be rewritten in terms of the finesse $\mathcal{F}$. With $\mathcal{F} = \Delta\omega/\gamma$, Eq. (3.73) becomes

$$\lambda = 4\left(\frac{x_z}{\tilde{\lambda}_e}\right)^2 \mathcal{F}^2, \tag{3.79}$$

where $\tilde{\lambda}_e$ is the wavelength of the driven optical mode. Therefore, to have $\lambda \gg 1$, we require $\mathcal{F} \gg \tilde{\lambda}_e/2x_z$. For the experiment in Ref. [45], the optical wavelength and the zero point motion amplitude are $\tilde{\lambda}_e = 400$ nm and $x_z = 7.86$ fm, respectively. The finesse is thus required to be $\mathcal{F} \gg 2.5 \cdot 10^7$. This limit being inaccessible for current technology, we need to lower the requirements. A possible strategy is to increase the zero point motion amplitude of the membrane. As suggested in [45] and demonstrated in [102], taking a SiN membrane 50 nm thick and with 40 μm diameter, it is possible to increase x_z. For $x_z = 222$ fm, the required finesse to achieve phonon QND measurement becomes $\mathcal{F} \gg 9 \cdot 10^5$. Despite the challenge, this limit is not necessarily science fiction [103, 104]. However, we believe that a smarter way consists in engineering an experiment in which the frequency difference between the even and odd modes $\Delta\omega$ is big enough to relax the requirement on the cavity finesse. This can perhaps be achieved with photonic crystals [105].

Chapter 4

Measurement device independent quantum key distribution

In the following, we present the results summarized in [4]. We study a setup allowing for QKD, in the settings where a third party, Charlie, measures the qubits sent by Alice and Bob. The chapter is structured as follows. In section 4.1, we introduce the high dimensional mdi–QKD protocol. The secret key rate is then derived in section 4.2, for the information encoded both in the spatial or temporal degrees of freedom of the travelling photons. Finally, we collect the results in section 4.3.

4.1 Protocol definition

We consider the setups presented in Fig. 4.1, where Alice and Bob both send a photon to Charlie. These are the general settings for mdi–QKD, where, to eliminate detectors loopholes, the measurement is delegated to an untrusted third party. Since we are interested in Hi–D encoding, we cannot consider the situation described in Ref. [64], where polarization is the degree of freedom used. Instead, the setup of Fig. 4.1(a) is based on spatial encoding of the qubit, while the one in Fig. 4.1(b) on temporal encoding. These are not upper bounded and, as such, are well suited for Hi–D mdi–QKD. Moreover, the bidimensional case is completely equivalent to the one of Ref. [64].

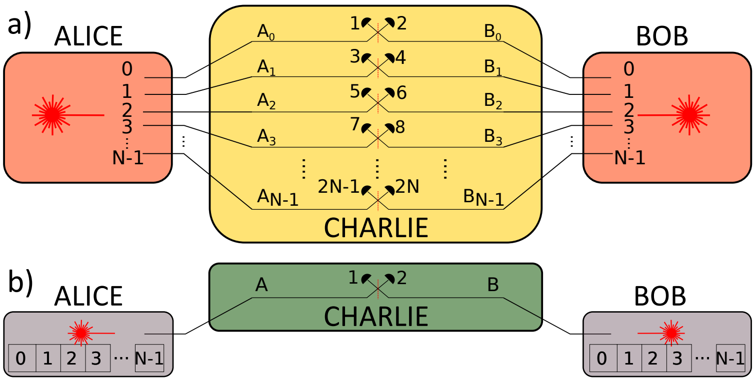

FIGURE 4.1: Schematic of the proposed setup for Hi-D-mdi QKD. *(a)* Space is used to encode information in different paths (multi-core fibers can be used as transmission channels). $2N$ single photon detectors are necessary for this configuration. *(b)* Time encoding scheme, where different time-slots are used to encode the qudits. The number of detectors is independent of the dimension N.

Most QKD protocols are based on mutually unbiased bases (MUBs). Usually, the computational Z basis ($\{|0\rangle, |1\rangle\}$ for qubits) is less susceptible to errors than the X basis ($\{|\phi_0\rangle, |\phi_1\rangle\}$, with $|\phi_0\rangle = (|0\rangle + |1\rangle)/\sqrt{2}$ and $|\phi_1\rangle = (|0\rangle - |1\rangle)/\sqrt{2}$). This is also the case for the encodings in Fig. 4.1, where different wave packets may dephase, but are unlikely to switch from one bin to another. Thus, the Z basis is used for key generation, and the X basis for error estimation. Generalizations of the Z and X bases are, respectively, $\{|0\rangle, |1\rangle, ..., |N-1\rangle\}$, and $\{|\phi_0\rangle, ..., |\phi_{N-1}\rangle\}$. Here, $|\phi_i\rangle$ are the N orthonormal superpositions of all the elements of the Z basis, with equal and real weights. As an example, for $N = 4$:

$$|\phi_0\rangle = \frac{1}{2}\left(|0\rangle + |1\rangle + |2\rangle + |3\rangle\right), \tag{4.1a}$$

$$|\phi_1\rangle = \frac{1}{2}\left(|0\rangle - |1\rangle - |2\rangle + |3\rangle\right), \tag{4.1b}$$

$$|\phi_2\rangle = \frac{1}{2}\left(|0\rangle + |1\rangle - |2\rangle - |3\rangle\right), \tag{4.1c}$$

$$|\phi_3\rangle = \frac{1}{2}\left(|0\rangle - |1\rangle + |2\rangle - |3\rangle\right). \tag{4.1d}$$

Our N dimensional mdi–QKD protocol for two MUBs is given by the procedure:

1. Alice and Bob choose, with probability $P_b \in (0, 1)$, the Z basis and with probability $1 - P_b$ the X basis.
2. Alice and Bob randomly generate one of the N qudits in the chosen basis, and send it to Charlie.
3. Whenever Charlie gets a coincidence click of two detectors, he publicly announces the outcome of his measurement. Otherwise, the event is discarded.
4. Steps (1) to (4) are repeated, to have enough statistics to estimate the quantum bit error rate (QBER), and sufficiently many bits of key.
5. Alice and Bob announce their bases, and estimate the QBER. If the QBER is too high, they abort the protocol.
6. Alice and Bob proceed with classical error correction and privacy amplification.

For simplicity (when not otherwise specified), we describe the protocol in the space encoding of Fig. 4.1(a), with straightforward generalization to the time encoding. Assume first that Alice and Bob both choose the Z basis. Whenever they send the same element $|i\rangle$, two photons arrive at the same BS and bunch together. There is thus no coincidence event, and the outcome is discarded. When Alice and Bob generate different states $|i\rangle$ and $|j\rangle$ ($i \neq j$), these photons necessarily end up in different detectors, and Charlie gets a coincidence click. The measurement collapses the state onto the two–dimensional space $\{|i\rangle_A \otimes |j\rangle_B; |j\rangle_A \otimes |i\rangle_B\}$, with the first state being Alice's, the latter Bob's. An eavesdropper Eve cannot distinguish whether Alice sent the state $|i\rangle$ and Bob $|j\rangle$ or vice versa, and thus can only guess with 50% probability the bit of key. In the X basis interference only allows half of all possible coincidence clicks to happen, and this permits determining the QBER relative to all two dimensional subspaces. For example, consider the case $N = 2$, and assume that both Alice and Bob send states with the same phase. Then, only coincidences on the same side of the BSs of Fig. 4.1(a) are allowed. If Alice and Bob choose different phases, opposite outcomes are permitted. This concept is generalizable to $N > 2$, considering that the detection collapses the state onto a two dimensional subspace, so that only the relative phases within this subspace matter. Alice and Bob can thus determine the contributions $\epsilon_x^{i,j}$ to the QBER ϵ_x, where $i, j = 0, ..., N-1$ are all possible indices of the 2–dimensional subspaces of the composite Hilbert space. For finite key length and high dimensions, there may be insufficient statistics to estimate each individual error rate $\epsilon_x^{i,j}$. In this case, the QBER can be determined by merging all X measurements into a single error rate ϵ_x. The QBER for the N dimensional protocol can thus be estimated with the same resources as for the standard 2 dimensional protocol [106]. If the error rates $\epsilon_x^{i,j}$ are different (e.g. due to different detectors), a better key rate can be obtained by treating the errors independently. For simplicity, we restrict ourselves to the simplest strategy and only consider a single error rate ϵ_x.

4.2 Secret key rate

We first prove that our Hi–D protocol is unconditionally secure, both for single photon sources and for coherent states with the decoy state method [73]. Then, we investigate all elements of the setup – sources, channels and detectors – to determine the QBER and raw key generation rate per application of the protocol (R_p) in the single photon case and for realistic experimental conditions. Finally, we consider the detector saturation regime.

In order to prove that Hi–D mdi–QKD is unconditionally secure, we show that the security of the N dimensional protocol follows from the two dimensional case [64, 107, 108, 109]. The key argument is that, whenever Charlie announces a coincidence click, the wave function is projected onto a two dimensional subspace, with all other states being erased by the measurement. As an example, consider Fig. 4.1(a), and assume that one of detectors 1 and 2 and one of detectors 7 and 8 click. The system is thus projected onto the Bell states $(|0\rangle_A|3\rangle_B \pm |3\rangle_A|0\rangle_B)/\sqrt{2}$, with the sign determined by the parity of the measurement (clicks in 1 & 7 or 2 & 8 lead to a plus, 1 & 8 or 2 & 7 to a minus). It follows that, if Alice and Bob both chose the X basis, all states other than $|0\rangle$ and $|3\rangle$ are erased by the measurement. On the other hand, if the Z basis was used, the parties had to have chosen these particular states as qudits. Every successful realization of the Hi–D protocol, is thus equivalent to an application of the two dimensional protocol, with the specific states identified by Charlie's measurement.

To complete the security proof, we follow Ref. [64] and consider the virtual qudit approach [110]. We imagine that both parties prepare an entangled state of two qudits, of which one is sent to Charlie, and the other (the virtual one) is kept. The travelling photons are then encoded in the basis states by measuring the virtual qudits. Since these measurements can be postponed till after Charlie's outcome is revealed, and since this outcome projects the state onto a two dimensional subsystem, the protocol is equivalent to the entanglement based protocol for qubits [111, 112].

The secret key rate r can be derived from Ref. [64, 110, 113, 114]:

$$r = R\left[1 - H\left(\epsilon_x\right) - f\left(\epsilon_z\right) H\left(\epsilon_z\right)\right], \tag{4.2}$$

where R is the raw key rate, $f(x) \geq 1$ is an inefficiency function for the error correction, and $H(x)$ the binary entropy. The same security proof can be adapted to the case of weak coherent pulses with the decoy state technique [64]. Since the measurement collapses the system to a two dimensional subspace, high–dimensional entanglement cannot be fully exploited with the current settings. It is thus not surprising that the Hi–D protocol can be described in terms of standard mdi–QKD protocols. However, as we will see in the following, our protocol still allows for improvements.

With the protocol proven unconditionally secure, we now estimate the key rate taking into account realistic sources, channels and detectors. Above and in the following we assumed identical channels and detectors.

4.2.1 Sources' contribution to the noise

In Hi–D mdi–QKD both Alice and Bob are required to generate qudits. These Hi–D photons have to interfere to generate the key, and therefore need to be identical. We quantify the errors introduced by distinguishable photons, assuming different shapes of the emitted photons. This can be described by expanding Alice's state $|i_A\rangle_A$ ($i = 0, ..., N-1$) in terms of Bob's wave function according to $|i_A\rangle_A \rightarrow \beta|i_B\rangle_A + \sqrt{1-|\beta|^2}|I\rangle_A$, where $|I\rangle_A$ shares the encoding of Bob's state (meaning that is in the same path/time slot), but is in one or more modes other than $|i_B\rangle_A$. If both parties use the Z basis, there should never be coincidences between detectors associated with the same BS in Fig. 4.1(a), and if the photons are in different paths it does not matter if they are distinguishable. Hence, the influence of distinguishable photons can be identified and never leads to errors in the key rate. However, for the X basis, there is a probability $|\beta|^2$ that the photons interfere correctly, and a probability $1 - |\beta|^2$ that they click at random detectors, thus incrementing the QBER ϵ_x by $(1 - |\beta|^2)/2$.

4.2.2 Channels' contribution to the noise

The most general errors affecting qudits in transmission lines are bit–flips and phase–shifts [115]. We neglect the first ones, since the probability that a photon disappears and reappears in another spatially or temporally separated slot is small [70, 69]. Instead, within the transmission channel any state $|i\rangle_J$ acquires a random phase, such that $|i\rangle_J \rightarrow e^{i\theta_i^J}|i\rangle_J$. Here, $i = 0, ..., N-1$ and $J = A, B$ indicates whether the qudit was generated by Alice or Bob. Like before, the Z basis is unaffected by phase noise, since bits of key are only exchanged when photons do not interfere. However, for any pair of elements in the X basis, interference prevents half of the allowed coincidence clicks. Whenever phase noise affects the qudits, wrong clicks happen with a probability

$$\frac{1 - \langle\cos\left(\theta_i^A - \theta_j^A - \theta_i^B + \theta_j^B\right)\rangle}{2}, \tag{4.3}$$

with $i \neq j$ (the case $i = j$ is automatically discarded). To quantify this effect, a noise model for the random variables $\theta_i^A - \theta_j^A$ and $\theta_j^B - \theta_i^B$ is required. Different models are better suited for different transmission lines and encoding schemes. In the space one, we consider a homogeneous situation, such that relative phases $\theta_i^A - \theta_j^A$ and $\theta_j^B - \theta_i^B$ are Gaussian distributed, with zero average and identical variance σ^2. In the time domain, phase drifts in the sources can be added as independent noise contributions in this model. Here, we assume white noise between subsequent pulses, such that the variances of $\theta_i^A - \theta_j^A$ and $\theta_j^B - \theta_i^B$ are $|i-j|\sigma^2$. Alternatively, if the interferometer is slowly drifting, an appropriate model would be $|i-j|^2\sigma^2$.

4.2.3 Detectors' contribution to the noise

For long distances, dark counts prevail over real clicks, increasing the QBER. We define P_{dc} the probability that a single detector clicks without a photon, and

$$P_s = \eta 10^{-\alpha_0 d/10} \tag{4.4}$$

the probability that a photon arrives at a detector and clicks. Here, η is the detector's efficiency, α_0 the fiber loss coefficient and d the distance separating both Alice and Bob from Charlie. In the Z basis, Alice and Bob verify if Charlie's announcement is compatible with the qudit they sent. A wrong bit of key is shared if and only if Alice and Bob send the same state, and a bit–flip (induced by dark counts) occurs. If none or one photon arrives, a random bit of key is shared with probabilities

$$4\frac{N-1}{N}(1-P_s)^2 P_{dc}^2 (1-P_{dc})^{2N-2} \qquad \text{for 0 photons,} \tag{4.5a}$$

$$4\frac{N-1}{N}P_s(1-P_s)P_{dc}(1-P_{dc})^{2N-2} \qquad \text{for 1 photon.} \tag{4.5b}$$

In case both photons click at the detectors, the probability to share a correct bit is

$$\frac{N-1}{N}P_s^2(1-P_{dc})^{2N-2}. \tag{4.6}$$

A wrong bit is produced by two photons bunching together and a different detector firing, which happens with a probability

$$2\frac{N-1}{N}P_s^2 P_{dc}(1-P_{dc})^{2N-2}. \tag{4.7}$$

From these, it is possible to find how many wrong bits of key are shared on average, and thus the QBER ϵ_z and the raw rate per application of the protocol R_p in the Z basis.

We now explicitly calculate the QBER ϵ_x in the X basis, including phase noise and distinguishability. If no photons arrive at Charlie, half the coincidence clicks are correct, half wrong, both occurring with probability

$$(1-P_s)^2 N(N-1)P_{dc}^2(1-P_{dc})^{2N-2}. \tag{4.8}$$

With a single photon clicking, the probability to have a correct or wrong coincidence click is

$$2P_s(1-P_s)(N-1)P_{dc}(1-P_{dc})^{2N-2}. \tag{4.9}$$

When both photons click at Charlie's detectors, the probabilities for the outcome to be correct or wrong are

$$P_s^2(1-P_{dc})^{2N-2}\left[P_{\text{good}}^{(X)} + (N-1)P_{dc}P_{\text{double}}^{(X)}\right] \qquad \text{correct click,} \tag{4.10a}$$

$$P_s^2(1-P_{dc})^{2N-2}\left[P_{\text{bad}}^{(X)} + (N-1)P_{dc}P_{\text{double}}^{(X)}\right] \qquad \text{wrong click.} \tag{4.10b}$$

Here, $P_{\text{double}}^{(X)} = (1+|\beta|^2)/N$ is the probability that both photons end up in the same detector. $P_{\text{bad}}^{(X)} = \left[N(N-1) - 2|\beta|^2 f_N\right]/[2N^2]$ and $P_{\text{good}}^{(X)} = \left[N(N-1) + 2|\beta|^2 f_N\right]/[2N^2]$ are the probabilities to have or not have the photonic interference spoiled by phase noise and distinguishability. The function f_N depends on the considered phase noise

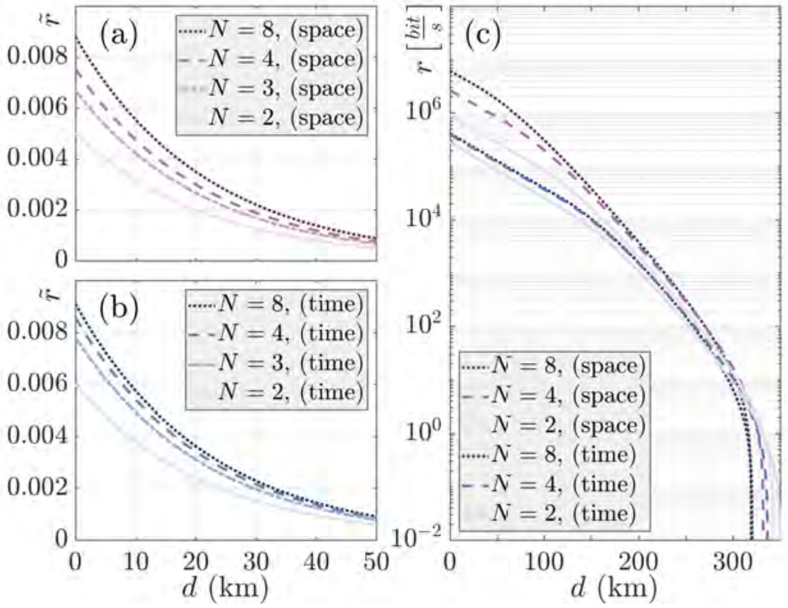

FIGURE 4.2: Secure key rate as a function of distance. Plain lines refer to $N = 2$, dash–dotted lines to $N = 3$, dashed lines to $N = 4$ and dotted lines to $N = 8$. *(a,b)*: No detector dead time, $\tau_d = 0$. The secret key rate without detector dead time $\tilde{r}$, is found using Eq. (4.2), with R substituted by R_p, i.e.: $\tilde{r}$ is in *bit* per application of the protocol. *(c)*: Secret key rate per second r as a function of distance. The dead time is $\tau_d = 20$ ns, and the minimum pulse separation $\tilde{T}_p = 200$ ps ($\tau_d/\tilde{T}_p = 100$). Common parameters are: $P_{dc} = 1 \cdot 10^{-6}$, $f(\epsilon_z) = 1$, $|\beta|^2 = 0.85$, $\eta = 0.145$ and σ equal to 0.175 (time) or 0.325 (space). σ is chosen such that, for $N = 2$ when only including dephasing, there is a QBER ϵ_x of 1.5% (time) or 5% (space).

model:

$$f_N = N(N-1)e^{-\sigma^2}/2 \qquad \text{space encoding,} \quad (4.11a)$$

$$f_N = \left[N\left(1-e^{-\sigma^2}\right) + e^{-N\sigma^2} - 1\right] / \left[2\sinh\left(\sigma^2/2\right)\right]^2 \qquad \text{time encoding.} \quad (4.11b)$$

With these results, it is possible to find how many bits of key are wrong on average, and thus the QBER ϵ_x in the X basis.

By merging the results above for sources, channel and detection imperfection, we derive Fig. 4.2(a,b), where the secret key rate per application of the protocol is determined using Eq. (4.2), with R substituted by the raw key rate per application of the protocol R_p. From the plot we find the advantage of Hi–D mdi–QKD, as compared to standard mdi–QKD. The probability that Alice and Bob send the same state $|i\rangle$ (resulting in a useless event) asymptotically goes to zero. This implies that, for small P_{dc}, the performance is improved by a factor $2(N-1)/N$ compared to the standard mdi–QKD protocol, where half of the events are lost even if Alice and Bob select the same basis.

4.2.4 Detector saturation regime

In the following, we study the regime where the detector's dead time τ_d is comparable to the timescale at which photons click at Charlie's detectors, and dark counts are negligible. We assume that during τ_d Alice and Bob send n pulses separated by $T_p = \tau_d/n$. In this regime, ordinary QKD has proven to gain advantage from high dimensional encoding [72, 116]. In the following, we extend this result to mdi–QKD, considering space and time encodings separately.

(*Space*) For any dimension N of the Hilbert space, $2N$ detectors are used (see Fig. 4.1). The probability per pulse P_{hit} that a detector is hit by a photon is

$$P_{\text{hit}} = \frac{1}{2N}\left[2P_s(1-P_s) + P_s^2(2N-1)/N\right]. \tag{4.12}$$

In the continuous limit ($t \gg T_p$), the cumulative distribution for a detector being hit within a time t is $1 - e^{-P_{\text{hit}}t/T_p}$. From this, the probability P_{alive} that a detector is not dark can be found to be

$$P_{\text{alive}} = P_{\text{hit}}^{-1}/(P_{\text{hit}}^{-1} + n), \tag{4.13}$$

where we assume that a detector remains dark for a time τ_d, no matter how many photons arrive while it is dark. The average number of raw bits N_{raw} exchanged during a dead time τ_d is therefore

$$N_{\text{raw}} = \frac{\tau_d}{T_p}\frac{(N-1)P_s^2 P_{\text{alive}}^2}{N}. \tag{4.14}$$

Maximizing N_{raw} with respect to T_p, we find the maximum of N_{raw} (assuming $P_s \ll N$):

$$\frac{N_{\text{raw}}^{(M)}}{\tau_d} = \max_{T_p}\left\{\frac{N_{\text{raw}}(T_p, P_s, N)}{\tau_d}\right\} = \frac{P_s(N-1)}{4\tau_d}. \tag{4.15}$$

(*Time*) In the time encoding, two detectors are used [see Fig. 4.1(b)], and the minimum time separation between two consecutive qudits is NT_p. Following the same procedure outlined above, we find N_{raw}, that is the same as in Eq. (4.14), but divided by a factor 2. This follows from the fact that during a train of N pulses, the same detector cannot click twice, leading to a better performance of the space protocol for short distances (see Fig. 4.3). The maximum number of bits exchanged during the detector's dead time τ_d is thus ($P_s \ll N$):

$$\frac{N_{\text{raw}}^{(M)}}{\tau_d} = \frac{P_s(N-1)}{8\tau_d N}. \tag{4.16}$$

Including the results found for the saturation regime, and limiting the interval T_p between consecutive pulses to some minimal value $\tilde{T}_p$, the raw key rate R can finally be determined to be:

$$R = \frac{N_{\text{raw}}^{(M)}}{\tau_d} R_p \tag{4.17}$$

where the raw key rate per application of the protocol R_p assumes no detector dead time $\tau_d = 0$. Here, $N_{\text{raw}}^{(M)}$ is either Eq. (4.15) (space encoding) or Eq. (4.16) (time encoding) when the optimal T_p is bigger than $\tilde{T}_p$. Otherwise, $N_{\text{raw}}^{(M)}$ is given by Eq. (4.14) with the substitution $T_p \to \tilde{T}_p$. Since the number of pulses is varied to reach the optimal performance, we evaluate the raw key rate in units of the detector dead time

τ_d. Therefore, while R_p is in bit/pulse, R is in unit of bit/s.

Since detectors are usually the limiting resource, we renormalize the raw key rate R in Eq. (4.17) with respect to the number of detectors n_{det} employed. This renormalization takes into account that $2N$ detectors could be used to perform N parallel applications of a two dimensional protocol, possibly outperforming the Hi–D setup. The rates per resource are shown in Fig. 4.3, with the plain dots referring to $\tilde{T}_p = \tau_d/100$, the empty ones to $\tilde{T}_p = \tau_d/20$. Figure 4.3 shows that with a limited rate of pulse generation (and thus finite $\tilde{T}_p$), there exists an optimal dimension N_{opt} for the best key rate ($P_s \ll N$):

$$N_{\text{opt}} = 2 + P_s\tau_d/\tilde{T}_p. \tag{4.18}$$

For $P_s\tau_d/T_p \gtrsim 1$, we see that with Hi–D mdi–QKD we increase the key rate *per detector*, due to the factor $2(N-1)/N$ found above.

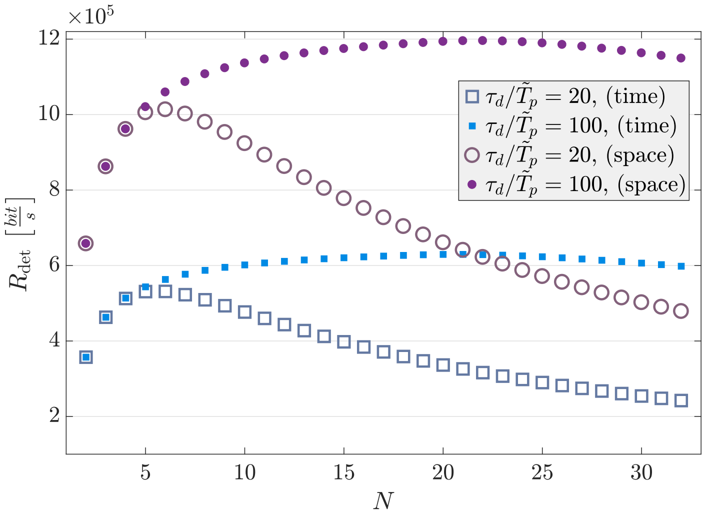

FIGURE 4.3: Raw key per detector $R_{\text{det}} = R/n_{\text{det}}$ as a function of the dimension N, in the detector saturation regime. Violet circles (full and empty) are used for the space encoding. Blue squares (full and empty) for the time encoding. The number of pulses n within τ_d is optimized to achieve the highest rate. The maximum possible number of qubits $\tau_d/\tilde{T}_p$ is either equal to 20 (empty circles and squares) or 100 (full circles and squares). $P_s = 0.2$, $\tau_d = 20$ ns, and $n_{\text{det}} = 2N$ (space) or $n_{\text{det}} = 2$ (time).

Our work allows, for given experimental conditions, to evaluate *a priori* which is the best setting to be employed in order to achieve the highest secret key rate. As an example, Fig. 4.2(c) shows the secret key rate r as a function of distance. For these curves, we used Eqs. (4.17) and (4.2) to determine the raw (R) and the secret (r) key rates, respectively. With the chosen parameters, for short distances it is better to use Hi–D mdi–QKD in the space encoding, while for very long distances low dimensional time encoding is preferable. Three regimes are visible in the plot: in the central region the rate scales as P_s^2, as two clicks are required. In the detector saturation regime, the probability for the detectors not to be dark is P_s^{-1}, meaning that the rate is linear in P_s. Finally, for large distances dark counts prevail, making QKD impossible. Note that for an accurate cost analysis, the number of detectors employed must also be considered, as in Fig. 4.3.

4.3 Conclusions

In conclusion, we have generalized the standard mdi–QKD protocol to higher dimensions N. In our analysis we consider the main sources of errors, and we prove the advantages of Hi–D mdi–QKD, particularly in the detector saturation regime. This result improves previous mdi–QKD schemes, allowing for higher communication rates. The considered generalization to Hi–D mdi–QKD is only one out of many possibilities. An attractive feature of our proposal, is that it can directly be implemented with existing technology. The protocol works by projecting the state onto a two dimensional Hilbert space, through the Bell state measurement performed by Charlie. Genuine Hi–D Bell state analysers would allow higher key rates, by increasing the PIE and reducing the informations acquired by Eve. However, discriminating Bell states with linear optics is challenging, leaving the Hi–D ones inaccessible [74]. The proposals in Refs. [117, 118, 119] for Hi–D Bell state analysis, may allow for genuine exploitation of high dimensional Bell states, but remain experimentally challenging. The present approach is thus the most attractive from a practical perspective.

Chapter 5

Conclusions & Outlook

In this last chapter, we briefly summarize the results derived above and present the outlooks for future research. In section 5.1, we focus on the opto- and electromechanical part, while in section 5.2 on QKD.

5.1 Towards mechanical quantum computers

In chapters 2 and 3, we suggested that current technology is mature enough to push opto- and electromechanics beyond linear interaction. We derived the figure of merit λ, telling us whether a setup is or is not capable of spotting quantum jumps – a purely non classical feature. We investigated existing experiments and proved that λ can exceed the limit allowing for the phonon QND measurement. Besides the fundamental result of proving macroscopic systems to behave quantumly, an interesting question is whether this work allows for practical applications. Here, we try to foresee short and long term developments, extending the role of mechanics in quantum information.

In our system, the mechanics is coupled both linearly and quadratically to the optical modes. As such, we access non Gaussian operations[1], which are in principle sufficient to build a fully operational quantum computer [94]. However, with λ exceeding unity, we only proved the phonon QND measurement to be available. In other regimes, the quadratic coupling may be negligible, and as such the interactions allowing for single and two qubits gates could remain inaccessible. Below, we outline proposals for using mechanical elements for quantum information purposes, giving qualitative arguments for their feasibility.

Direct outcomes of the phonon QND measurement are readout and initialization of the mechanical wave vector. Since the measure projects the membrane onto a Fock state, combinations of red (blue) sideband cooling (heating) with the QND measurement, allow for preparing any desired number state. More indirect applications of our work are found by thinking at the expansion of $(\hat{b}+\hat{b}^\dagger)^2$. The resonant term $\hat{b}^\dagger\hat{b}$ is the one extensively studied for the QND measurement, and is selected by resonantly driving the even optical mode: $\Delta \equiv \omega_{\mathrm{drive}} - \omega_{\mathrm{e}} = 0$. With a different detuning, however, one of the other terms can be chosen: $\hat{b}^\dagger\hat{b}^\dagger$ for $\Delta = 2\omega_{\mathrm{m}}$ and $\hat{b}\hat{b}$ for $\Delta = -2\omega_{\mathrm{m}}$. Importantly, for all these processes, deleterious effects related to the linear couplings are the same. In fact, both for $\Delta = 0$ and $\Delta = \pm 2\omega_{\mathrm{m}}$, the sidebands at $\pm\omega_{\mathrm{m}}$ are equally suppressed by the same frequency difference. As such, we believe that the condition under which these processes dominate is similar (or even the same) to the one derived for the QND measurement: $\lambda \geq 42$.

---

[1] Other ways to access non Gaussian operations have been proposed, for simulators of mechanical systems, in Refs. [120, 121].

Let us now discuss about $\hat{b}^\dagger\hat{b}^\dagger$ and $\hat{b}\hat{b}$. The first one describes squeezing of the mechanical state. Limited only by the environment and the linear couplings, this squeezing is in principle unbounded and can exceed the maximum of 3 dB allowed by the linear coupling (without back action evasion schemes) [22, 23, 24, 11, 12]. More interesting is the term $\hat{b}\hat{b}$, that identifies a quite special mechanical cooling. An input photon here annihilates two phonons, to create an excitation into the cavity. The first excited mechanical state is thus protected, as there is not enough energy for compensating the conversion. The membrane is transformed into an effective two dimensional system, with only its ground and first excited states in the Hilbert space. In other words, we have a mechanical qubit.

With the necessity of building gates, we finally describe how to achieve all rotations in the Bloch sphere. The idea is to induce Rabi oscillations in the system, exploiting the linear interaction with a blue detuned laser. And this is quite straightforward; in fact, the real challenge is to make the two phonon cooling work (i.e.: build a system for which $\lambda \gg 1$). Once the membrane is an effective two level system, we can use the linear coupling to rotate the vector on the Bloch sphere. Now intentionally driving the cavity at $\Delta = \omega_\mathrm{m}$, we choose the rotation axis with the laser phase, and its magnitude with intensity and duration of the pulse. Notice that combining the Bloch sphere rotations with the QND readout, we can perform a full tomography of the mechanical density matrix.

In conclusion, we extended the role of mechanical systems in quantum computing. With a lack of humbleness, we developed the idea of a mechanical qubit. We derived a clear condition – the parameter λ – that tells us whether membranes show or hide their quantum features. In electromechanics, we proved that the phonon QND measurement is possible, and found the critical features to be addressed in the fabrication of optical setups. As said in chapter 1, other platforms are mature for running the first quantum algorithms. However, mechanical systems are unbeatable in terms of coherence times and can be easily scaled. As such, future quantum computers may benefit from these new qubits. Maybe a purely mechanical machine will be never built, but hybrid quantum computers could be the best option we have[2]. With the computational tasks distributed between the different platforms, we can really gain an advantage from all the good properties, and maybe push the performance beyond classical computers.

5.2 Guessing the future of QKD

QKD is the technology leading the second quantum revolution, where non classical features such as entanglement are used to accomplish otherwise impossible tasks. While the quantum computer struggles to outperform classical machines, QKD is a mature application. Devices can be bought online, and metropolitan networks are being developed right now [123, 124, 125]. A global phenomenon, QKD reaches the vastness of space, with dedicated satellites communicating with the ground [126, 127, 128]. As such, what is left to do is improving existing setups, tackling the current limitations: short communication distances, security loopholes, and low key rates. As said above, mdi–QKD addresses the first two, but needs to compromise with a lower key rate. Our work allows retaining all advantages of standard mdi–QKD, without compromising on the key rate. Importantly, it does not increase the system complexity and, as such, permits current platforms to be improved without

---

[2] I actually believe in that. It is not advertisement for the new centre of *Hybrid* Quantum Networks (Hy-Q). That, by the way, is quite remarkable!

significant effort. As a contribution to the field, we developed simple ways to estimate a priori the secret key rate of the device. With the noise sources characterized, it is possible to find the best settings for given resources (or vice versa). Moreover, generalizing our results to different kinds of dephasing can be done just by modifying the function f_N in Eq. (4.11). Including bit flips is more complicated, but also feasible (and likely not required). Altogether, Hi–D mdi–QKD has been extensively characterized, in the setting where Charlie projects the state onto two dimensional subspaces. As such, the future of mdi–QKD is likely related to real exploitation of high dimensional entanglement, to increase the PIE of single pulses. From one side, this promises performance increments that are only bounded by the technical difficulties of operating with high dimensional states. On the other side, designing a setup allowing for discrimination of Bell states is challenging using only linear optics [74]. Potentially, this is a long term limitation. Another promising approach beyond mdi–QKD is twin field (tf) QKD, which has been recently proposed in Ref. [129]. Here, in a similar configuration as the one investigated above, the advantages of mdi–QKD are retained, but the communication distance considerably extended. By using two optical fields resulting in a single photon interference followed by a single photon detection event, tf–QKD allows for key exchange beyond 500 km of distance. In a near future, unconditional security against general attacks has to be demonstrated for tf–QKD. Next, generalization to higher dimensions could be done, despite difficulties related to the specific encoding used. Finally, the long term gamble of QKD is to achieve device independent QKD. Extremely difficult due to the requirement of high quality entanglement creation and storage, di–QKD is secure against all loopholes, and a step in between standard QKD and cloud quantum computing. Despite the promising results achieved in Refs. [130, 131], the way is still long, with similar challenges as the ones for building a quantum computer.

Bibliography

[1] Luca Dellantonio et al. "Multipartite entanglement detection with nonsymmetric probing". In: *Phys. Rev. A* 95 (4 2017), p. 040301. DOI: `10.1103/PhysRevA.95.040301`. URL: `https://link.aps.org/doi/10.1103/PhysRevA.95.040301`.

[2] Luca Dellantonio. *Entanglement Criteria for Spin Squeezing*. Niels Bohr Institute, Copenhagen University, 2015.

[3] Luca Dellantonio et al. "Quantum nondemolition measurement of mechanical motion quanta". In: *Nature Communications* 9.1 (2018), p. 3621. ISSN: 2041-1723. DOI: `10.1038/s41467-018-06070-y`. URL: `https://doi.org/10.1038/s41467-018-06070-y`.

[4] Luca Dellantonio, Anders S Sørensen, and Davide Bacco. "High dimensional measurement device independent quantum key distribution on two dimensional subspaces". In: *arXiv preprint arXiv:1809.04405* (2018).

[5] John M. Martinis, Michel H. Devoret, and John Clarke. "Energy-Level Quantization in the Zero-Voltage State of a Current-Biased Josephson Junction". In: *Phys. Rev. Lett.* 55 (15 1985), pp. 1543–1546. DOI: `10.1103/PhysRevLett.55.1543`. URL: `https://link.aps.org/doi/10.1103/PhysRevLett.55.1543`.

[6] Markus Aspelmeyer, Tobias J Kippenberg, and Florian Marquardt. "Cavity optomechanics". In: *Reviews of Modern Physics* 86.4 (2014), p. 1391.

[7] JD Teufel et al. "Circuit cavity electromechanics in the strong-coupling regime". In: *Nature* 471.7337 (2011), pp. 204–208.

[8] J. D. Teufel et al. "Sideband cooling of micromechanical motion to the quantum ground state". In: *Nature* 475 (7356 2011), pp. 359–363. DOI: `10.1038/nature10261`.

[9] A. D. O'Connell et al. "Quantum ground state and single-phonon control of a mechanical resonator". In: *Nature* 464 (7289 2010), pp. 697–703. DOI: `10.1038/nature08967`.

[10] Georg Heinrich and Florian Marquardt. "Coupled multimode optomechanics in the microwave regime". In: *EPL (Europhysics Letters)* 93.1 (2011), p. 18003. URL: `http://stacks.iop.org/0295-5075/93/i=1/a=18003`.

[11] Emma Edwina Wollman et al. "Quantum squeezing of motion in a mechanical resonator". In: *Science* 349.6251 (2015), pp. 952–955.

[12] C. F. Ockeloen-Korppi et al. "Noiseless Quantum Measurement and Squeezing of Microwave Fields Utilizing Mechanical Vibrations". In: *Phys. Rev. Lett.* 118 (10 2017), p. 103601. DOI: `10.1103/PhysRevLett.118.103601`. URL: `https://link.aps.org/doi/10.1103/PhysRevLett.118.103601`.

[13] Ewold Verhagen et al. "Quantum-coherent coupling of a mechanical oscillator to an optical cavity mode". In: *Nature* 482.7383 (2012), p. 63.

[14] Jasper Chan et al. "Laser cooling of a nanomechanical oscillator into its quantum ground state". In: *Nature* 478 (7367 2011), pp. 89–92. DOI: `10.1038/nature10461`.

[15] R. W. Peterson et al. "Laser Cooling of a Micromechanical Membrane to the Quantum Backaction Limit". In: *Phys. Rev. Lett.* 116 (6 2016), p. 063601. DOI: `10.1103/PhysRevLett.116.063601`. URL: `https://link.aps.org/doi/10.1103/PhysRevLett.116.063601`.

[16] A. Schliesser et al. "Radiation Pressure Cooling of a Micromechanical Oscillator Using Dynamical Backaction". In: *Phys. Rev. Lett.* 97 (24 2006), p. 243905. DOI: `10.1103/PhysRevLett.97.243905`. URL: `https://link.aps.org/doi/10.1103/PhysRevLett.97.243905`.

[17] Žarko Zobenica et al. "Integrated nano-opto-electro-mechanical sensor for spectrometry and nanometrology". In: *Nature communications* 8.1 (2017), p. 2216.

[18] JD Teufel et al. "Nanomechanical motion measured with an imprecision below that at the standard quantum limit". In: *Nature nanotechnology* 4.12 (2009), pp. 820–823.

[19] Eduardo Gil-Santos et al. "Nanomechanical mass sensing and stiffness spectrometry based on two-dimensional vibrations of resonant nanowires". In: *Nat Nano* 5 (9 2010), pp. 641–645. DOI: `10.1038/nnano.2010.151`.

[20] MS Hanay et al. "Single-protein nanomechanical mass spectrometry in real time". In: *Nature nanotechnology* 7.9 (2012), pp. 602–608.

[21] P. Weber et al. "Force sensitivity of multilayer graphene optomechanical devices". In: *Nature Communications* 7 (2016), p. 12496. DOI: `10.1038/ncomms12496`.

[22] Daniel WC Brooks et al. "Non-classical light generated by quantum-noise-driven cavity optomechanics". In: *Nature* 488.7412 (2012), pp. 476–480.

[23] Amir H Safavi-Naeini et al. "Squeezed light from a silicon micromechanical resonator". In: *Nature* 500.7461 (2013), pp. 185–189.

[24] T. P. Purdy et al. "Strong Optomechanical Squeezing of Light". In: *Phys. Rev. X* 3 (3 2013), p. 031012. DOI: `10.1103/PhysRevX.3.031012`. URL: `https://link.aps.org/doi/10.1103/PhysRevX.3.031012`.

[25] Christoffer B Møller et al. "Back action evading quantum measurement of motion in a negative mass reference frame". In: *Nature* 547.2 (2017), p. 191. DOI: `http://dx.doi.org/10.1038/nature22980`.

[26] C. F. Ockeloen-Korppi et al. "Quantum Backaction Evading Measurement of Collective Mechanical Modes". In: *Phys. Rev. Lett.* 117 (14 2016), p. 140401. DOI: `10.1103/PhysRevLett.117.140401`. URL: `https://link.aps.org/doi/10.1103/PhysRevLett.117.140401`.

[27] B. P. Abbott et al. "Observation of Gravitational Waves from a Binary Black Hole Merger". In: *Phys. Rev. Lett.* 116 (6 2016), p. 061102. DOI: `10.1103/PhysRevLett.116.061102`. URL: `https://link.aps.org/doi/10.1103/PhysRevLett.116.061102`.

[28] Simon Gröblacher et al. "Observation of strong coupling between a micromechanical resonator and an optical cavity field". In: *Nature* 460.7256 (2009), pp. 724–727.

[29] Seth Lloyd and Samuel L. Braunstein. "Quantum Computation over Continuous Variables". In: *Phys. Rev. Lett.* 82 (8 1999), pp. 1784–1787. DOI: `10.1103/PhysRevLett.82.1784`. URL: `https://link.aps.org/doi/10.1103/PhysRevLett.82.1784`.

[30] Thaddeus D Ladd et al. "Quantum computers". In: *Nature* 464.7285 (2010), p. 45.

[31] D. Leibfried et al. "Quantum dynamics of single trapped ions". In: *Rev. Mod. Phys.* 75 (1 2003), pp. 281–324. DOI: `10.1103/RevModPhys.75.281`. URL: `https://link.aps.org/doi/10.1103/RevModPhys.75.281`.

[32] Hannes Bernien et al. "Probing many-body dynamics on a 51-atom quantum simulator". In: *Nature* 551.7682 (2017), p. 579.

[33] Daniel Barredo et al. "Synthetic three-dimensional atomic structures assembled atom by atom". In: *Nature* 561.7721 (2018), p. 79.

[34] Patrice Bertet et al. "Dephasing of a superconducting qubit induced by photon noise". In: *Physical review letters* 95.25 (2005), p. 257002.

[35] Bibek Pokharel et al. "Demonstration of fidelity improvement using dynamical decoupling with superconducting qubits". In: *arXiv preprint arXiv:1807.08768* (2018).

[36] Esteban A Martinez et al. "Real-time dynamics of lattice gauge theories with a few-qubit quantum computer". In: *Nature* 534.7608 (2016), pp. 516–519.

[37] Kuntal Halder et al. "Digital Quantum Simulation of Laser-Pulse Induced Tunneling Mechanism in Chemical Isomerization Reaction". In: *arXiv preprint arXiv:1808.00021* (2018).

[38] Sergio Boixo et al. "Characterizing quantum supremacy in near-term devices". In: *Nature Physics* 14.6 (2018), p. 595.

[39] Yeghishe Tsaturyan et al. "Ultracoherent nanomechanical resonators via soft clamping and dissipation dilution". In: *Nature nanotechnology* 12.8 (2017), p. 776.

[40] Rick Leijssen et al. "Nonlinear cavity optomechanics with nanomechanical thermal fluctuations". In: *Nature communications* 8 (2017), ncomms16024.

[41] Jack C Sankey et al. "Strong and tunable nonlinear optomechanical coupling in a low-loss system". In: *Nature Physics* 6.9 (2010), p. 707.

[42] Tolga Bagci et al. "Optical detection of radio waves through a nanomechanical transducer". In: *Nature* 507.7490 (2014), pp. 81–85.

[43] Freek Ruesink et al. "Optical circulation in a multimode optomechanical resonator". In: *Nature communications* 9.1 (2018), p. 1798.

[44] Alexey V. Gorshkov et al. "Universal Approach to Optimal Photon Storage in Atomic Media". In: *Phys. Rev. Lett.* 98 (12 2007), p. 123601. DOI: `10.1103/PhysRevLett.98.123601`. URL: `https://link.aps.org/doi/10.1103/PhysRevLett.98.123601`.

[45] J. D. Thompson et al. "Strong dispersive coupling of a high-finesse cavity to a micromechanical membrane". In: *Nature* 452 (7183 2008). DOI: `10.1038/nature06715`. URL: `http://www.nature.com/nature/journal/v452/n7183/suppinfo/nature06715_S1.html`.

[46] A M Jayich et al. "Dispersive optomechanics: a membrane inside a cavity". In: *New Journal of Physics* 10.9 (2008), p. 095008. URL: `http://stacks.iop.org/1367-2630/10/i=9/a=095008`.

[47] Max Ludwig et al. "Enhanced Quantum Nonlinearities in a Two-Mode Optomechanical System". In: *Phys. Rev. Lett.* 109 (6 2012), p. 063601. DOI: `10.1103/PhysRevLett.109.063601`. URL: `https://link.aps.org/doi/10.1103/PhysRevLett.109.063601`.

[48] Yariv Yanay and Aashish A Clerk. "Shelving-style QND phonon-number detection in quantum optomechanics". In: *New Journal of Physics* 19.3 (2017), p. 033014.

[49] Shiqian Ding et al. "Cross-Kerr Nonlinearity for Phonon Counting". In: *Phys. Rev. Lett.* 119 (19 2017), p. 193602. DOI: `10.1103/PhysRevLett.119.193602`. URL: `https://link.aps.org/doi/10.1103/PhysRevLett.119.193602`.

[50] Antonio Acín et al. "Device-Independent Security of Quantum Cryptography against Collective Attacks". In: *Phys. Rev. Lett.* 98 (23 2007), p. 230501. DOI: `10.1103/PhysRevLett.98.230501`. URL: `https://link.aps.org/doi/10.1103/PhysRevLett.98.230501`.

[51] Chi-Hang Fred Fung et al. "Phase-remapping attack in practical quantum-key-distribution systems". In: *Phys. Rev. A* 75 (3 2007), p. 032314. DOI: `10.1103/PhysRevA.75.032314`. URL: `https://link.aps.org/doi/10.1103/PhysRevA.75.032314`.

[52] Bing Qi et al. "Time-shift attack in practical quantum cryptosystems". In: *arXiv preprint quant-ph/0512080* (2005).

[53] Yi Zhao et al. "Quantum hacking: Experimental demonstration of time-shift attack against practical quantum-key-distribution systems". In: *Phys. Rev. A* 78 (4 2008), p. 042333. DOI: `10.1103/PhysRevA.78.042333`. URL: `https://link.aps.org/doi/10.1103/PhysRevA.78.042333`.

[54] Feihu Xu, Bing Qi, and Hoi-Kwong Lo. "Experimental demonstration of phase-remapping attack in a practical quantum key distribution system". In: *New Journal of Physics* 12.11 (2010), p. 113026. URL: `http://stacks.iop.org/1367-2630/12/i=11/a=113026`.

[55] Lars Lydersen et al. "Hacking commercial quantum cryptography systems by tailored bright illumination". In: *Nature photonics* 4.10 (2010), pp. 686–689.

[56] Lars Lydersen et al. "Thermal blinding of gated detectors in quantum cryptography". In: *Opt. Express* 18.26 (2010), pp. 27938–27954. DOI: `10.1364/OE.18.027938`. URL: `http://www.opticsexpress.org/abstract.cfm?URI=oe-18-26-27938`.

[57] Lars Lydersen et al. "Controlling a superconducting nanowire single-photon detector using tailored bright illumination". In: *New Journal of Physics* 13.11 (2011), p. 113042. URL: `http://stacks.iop.org/1367-2630/13/i=11/a=113042`.

[58] L. Lydersen, J. Skaar, and V. Makarov. "Tailored bright illumination attack on distributed-phase-reference protocols". In: *Journal of Modern Optics* 58.8 (2011), pp. 680–685. DOI: `10.1080/09500340.2011.565889`. eprint: `https://doi.org/10.1080/09500340.2011.565889`. URL: `https://doi.org/10.1080/09500340.2011.565889`.

[59] C Wiechers et al. "After-gate attack on a quantum cryptosystem". In: *New Journal of Physics* 13.1 (2011), p. 013043. URL: `http://stacks.iop.org/1367-2630/13/i=1/a=013043`.

[60] Shihan Sajeed et al. "Attacks exploiting deviation of mean photon number in quantum key distribution and coin tossing". In: *Phys. Rev. A* 91 (3 2015), p. 032326. DOI: `10.1103/PhysRevA.91.032326`. URL: `https://link.aps.org/doi/10.1103/PhysRevA.91.032326`.

[61] Dominic Mayers and Andrew Yao. "Quantum cryptography with imperfect apparatus". In: *Foundations of Computer Science, 1998. Proceedings. 39th Annual Symposium on*. IEEE. 1998, pp. 503–509.

[62] Matthew McKague. "Quantum information processing with adversarial devices". In: *arXiv preprint arXiv:1006.2352* (2010).

[63] Samuel L. Braunstein and Stefano Pirandola. "Side-Channel-Free Quantum Key Distribution". In: *Phys. Rev. Lett.* 108 (13 2012), p. 130502. DOI: `10.1103/PhysRevLett.108.130502`. URL: `https://link.aps.org/doi/10.1103/PhysRevLett.108.130502`.

[64] Hoi-Kwong Lo, Marcos Curty, and Bing Qi. "Measurement-Device-Independent Quantum Key Distribution". In: *Phys. Rev. Lett.* 108 (13 2012), p. 130503. DOI: `10.1103/PhysRevLett.108.130503`. URL: `https://link.aps.org/doi/10.1103/PhysRevLett.108.130503`.

[65] Michael Bass, Casimer DeCusatis, and Jay Enoch. *Handbook of optics*. Vol. 2. McGraw-Hill New York, 2001.

[66] M Lucamarini et al. "Overcoming the rate–distance limit of quantum key distribution without quantum repeaters". In: *Nature* (2018), p. 1.

[67] HF Chau et al. "Qudit-Based Measurement-Device-Independent Quantum Key Distribution Using Linear Optics". In: *arXiv preprint arXiv:1608.08329* (2016).

[68] Davide Bacco et al. "Two-dimensional distributed-phase-reference protocol for quantum key distribution". In: *Scientific reports* 6 (2016).

[69] Yunhong Ding et al. "High-Dimensional Quantum Key Distribution based on Multicore Fiber using Silicon Photonic Integrated Circuits". In: *npj Quantum Information* 3:25 (2017).

[70] Yang Liu et al. "Experimental Measurement-Device-Independent Quantum Key Distribution". In: *Phys. Rev. Lett.* 111 (13 2013), p. 130502. DOI: `10.1103/PhysRevLett.111.130502`. URL: `https://link.aps.org/doi/10.1103/PhysRevLett.111.130502`.

[71] Nurul T. Islam et al. "Provably secure and high-rate quantum key distribution with time-bin qudits". In: *Science Advances* 3.11 (2017). DOI: `10.1126/sciadv.1701491`. URL: `http://advances.sciencemag.org/content/3/11/e1701491`.

[72] Zheshen Zhang et al. "Unconditional Security of Time-Energy Entanglement Quantum Key Distribution Using Dual-Basis Interferometry". In: *Phys. Rev. Lett.* 112 (12 2014), p. 120506. DOI: `10.1103/PhysRevLett.112.120506`. URL: `https://link.aps.org/doi/10.1103/PhysRevLett.112.120506`.

[73] Hoi-Kwong Lo, Xiongfeng Ma, and Kai Chen. "Decoy State Quantum Key Distribution". In: *Phys. Rev. Lett.* 94 (23 2005), p. 230504. DOI: `10.1103/PhysRevLett.94.230504`. URL: `https://link.aps.org/doi/10.1103/PhysRevLett.94.230504`.

[74] John Calsamiglia. "Generalized measurements by linear elements". In: *Phys. Rev. A* 65 (3 2002), p. 030301. DOI: `10.1103/PhysRevA.65.030301`. URL: `https://link.aps.org/doi/10.1103/PhysRevA.65.030301`.

[75] Lev Vaidman and Nadav Yoran. "Methods for reliable teleportation". In: *Phys. Rev. A* 59 (1 1999), pp. 116–125. DOI: `10.1103/PhysRevA.59.116`. URL: `https://link.aps.org/doi/10.1103/PhysRevA.59.116`.

[76] Vladimir B Braginsky and F Ya Khalili. "Quantum nondemolition measurements: the route from toys to tools". In: *Reviews of Modern Physics* 68.1 (1996), p. 1.

[77] Aashish A Clerk et al. "Introduction to quantum noise, measurement, and amplification". In: *Reviews of Modern Physics* 82.2 (2010), p. 1155.

[78] Haixing Miao et al. "Standard Quantum Limit for Probing Mechanical Energy Quantization". In: *Phys. Rev. Lett.* 103 (10 2009), p. 100402. DOI: `10.1103/PhysRevLett.103.100402`. URL: `https://link.aps.org/doi/10.1103/PhysRevLett.103.100402`.

[79] Yariv Yanay, Jack C. Sankey, and Aashish A. Clerk. "Quantum backaction and noise interference in asymmetric two-cavity optomechanical systems". In: *Phys. Rev. A* 93 (6 2016), p. 063809. DOI: `10.1103/PhysRevA.93.063809`. URL: `https://link.aps.org/doi/10.1103/PhysRevA.93.063809`.

[80] I. Martin and W. H. Zurek. "Measurement of Energy Eigenstates by a Slow Detector". In: *Phys. Rev. Lett.* 98 (12 2007), p. 120401. DOI: `10.1103/PhysRevLett.98.120401`. URL: `https://link.aps.org/doi/10.1103/PhysRevLett.98.120401`.

[81] Michel H Devoret et al. "Quantum fluctuations in electrical circuits". In: *Les Houches, Session LXIII* 7.8 (1995).

[82] Xuefeng Song et al. "Stamp Transferred Suspended Graphene Mechanical Resonators for Radio Frequency Electrical Readout". In: *Nano Letters* 12.1 (2012). PMID: 22141577, pp. 198–202. DOI: `10.1021/nl203305q`. eprint: `http://dx.doi.org/10.1021/nl203305q`. URL: `http://dx.doi.org/10.1021/nl203305q`.

[83] J. Scott Bunch et al. "Electromechanical Resonators from Graphene Sheets". In: *Science* 315.5811 (2007), pp. 490–493. ISSN: 0036-8075. DOI: `10.1126/science.1136836`. URL: `http://science.sciencemag.org/content/315/5811/490`.

[84] V. Singh et al. "Optomechanical coupling between a multilayer graphene mechanical resonator and a superconducting microwave cavity". In: *Nat Nano* 9 (10 2014), pp. 820–824. DOI: `10.1038/nnano.2014.168`.

[85] P. Weber et al. "Coupling Graphene Mechanical Resonators to Superconducting Microwave Cavities". In: *Nano Letters* 14.5 (2014). PMID: 24745803, pp. 2854–2860. DOI: `10.1021/nl500879k`. eprint: `http://dx.doi.org/10.1021/nl500879k`. URL: `http://dx.doi.org/10.1021/nl500879k`.

[86] Emil Zeuthen. "Electro-Optomechanical Transduction & Quantum Hard-Sphere Model for Dissipative Rydberg-EIT Media". PhD thesis. The Niels Bohr Institute, Faculty of Science, University of Copenhagen, 2015.

[87] R. De Alba et al. "Tunable phonon-cavity coupling in graphene membranes". In: *Nat Nano* 11 (9 2016), pp. 741–746. DOI: `10.1038/nnano.2016.86`.

[88] John P. Mathew et al. “Dynamical strong coupling and parametric amplification of mechanical modes of graphene drums”. In: *Nat Nano* 11 (9 2016), pp. 747–751. DOI: `10.1038/nnano.2016.94`.

[89] Changyao Chen et al. “Performance of monolayer graphene nanomechanical resonators with electrical readout”. In: *Nat Nano* 4 (12 2009), pp. 861–867. DOI: `10.1038/nnano.2009.267`.

[90] T Rocheleau et al. “Preparation and detection of a mechanical resonator near the ground state of motion”. In: *Nature* 463.7277 (2010), p. 72.

[91] Bing He et al. “Radiation Pressure Cooling as a Quantum Dynamical Process”. In: *Phys. Rev. Lett.* 118 (23 2017), p. 233604. DOI: `10.1103/PhysRevLett.118.233604`. URL: `https://link.aps.org/doi/10.1103/PhysRevLett.118.233604`.

[92] Luca Dellantonio et al. in preparation.

[93] Jean Dalibard, Yvan Castin, and Klaus Mølmer. “Wave-function approach to dissipative processes in quantum optics”. In: *Physical review letters* 68.5 (1992), p. 580.

[94] Samuel L. Braunstein and Peter van Loock. “Quantum information with continuous variables”. In: *Rev. Mod. Phys.* 77 (2 2005), pp. 513–577. DOI: `10.1103/RevModPhys.77.513`. URL: `https://link.aps.org/doi/10.1103/RevModPhys.77.513`.

[95] Ottaviano Fabrizio Mossotti. *Discussione analitica sull'influenza che l'azione di un mezzo dielettrico ha sulla distribuzione dell'elettricità alla superficie di più corpi elettrici disseminati in esso*. dai tipi della r. D. camera, 1846.

[96] Roy J. Glauber and M. Lewenstein. “Quantum optics of dielectric media”. In: *Phys. Rev. A* 43 (1 1991), pp. 467–491. DOI: `10.1103/PhysRevA.43.467`. URL: `https://link.aps.org/doi/10.1103/PhysRevA.43.467`.

[97] W. Fader. “Theory of two coupled lasers”. In: *IEEE Journal of Quantum Electronics* 21.11 (1985), pp. 1838–1844. ISSN: 0018-9197. DOI: `10.1109/JQE.1985.1072577`.

[98] Andreas Kronwald. “Nonlinear quantum effects and squeezing in cavity optomechanics”. PhD thesis. The Max Planck Institute for the science of light, 2015.

[99] Steven G. Johnson et al. “Perturbation theory for Maxwell's equations with shifting material boundaries”. In: *Phys. Rev. E* 65 (6 2002), p. 066611. DOI: `10.1103/PhysRevE.65.066611`. URL: `https://link.aps.org/doi/10.1103/PhysRevE.65.066611`.

[100] Mario F. Gely et al. “Convergence of the multimode quantum Rabi model of circuit quantum electrodynamics”. In: *Phys. Rev. B* 95 (24 2017), p. 245115. DOI: `10.1103/PhysRevB.95.245115`. URL: `https://link.aps.org/doi/10.1103/PhysRevB.95.245115`.

[101] Tilman Esslinger and Klaus Mølmer. “Atoms and Molecules in Lattices: Bose-Einstein Condensates Built on a Shared Vacuum”. In: *Phys. Rev. Lett.* 90 (16 2003), p. 160406. DOI: `10.1103/PhysRevLett.90.160406`. URL: `https://link.aps.org/doi/10.1103/PhysRevLett.90.160406`.

[102] Onur Kilic et al. “Photonic crystal slabs demonstrating strong broadband suppression of transmission in the presence of disorders”. In: *Optics letters* 29.23 (2004), pp. 2782–2784.

[103] H Mabuchi et al. “Real-time detection of individual atoms falling through a high-finesse optical cavity”. In: *Optics letters* 21.17 (1996), pp. 1393–1395.

[104] P. Münstermann et al. “Dynamics of Single-Atom Motion Observed in a High-Finesse Cavity”. In: *Phys. Rev. Lett.* 82 (19 1999), pp. 3791–3794. DOI: `10.1103/PhysRevLett.82.3791`. URL: `https://link.aps.org/doi/10.1103/PhysRevLett.82.3791`.

[105] John D Joannopoulos et al. *Photonic crystals: molding the flow of light*. Princeton university press, 2011.

[106] Marcos Curty et al. “Finite-key analysis for measurement-device-independent quantum key distribution”. In: *Nature communications* 5 (2014), p. 3732.

[107] Hitoshi Inamori. “Security of Practical Time-Reversed EPR Quantum Key Distribution”. In: *Algorithmica* 34.4 (2002), pp. 340–365. ISSN: 1432-0541. DOI: `10.1007/s00453-002-0983-4`. URL: `https://doi.org/10.1007/s00453-002-0983-4`.

[108] Won-Young Hwang. “Quantum Key Distribution with High Loss: Toward Global Secure Communication”. In: *Phys. Rev. Lett.* 91 (5 2003), p. 057901. DOI: `10.1103/PhysRevLett.91.057901`. URL: `https://link.aps.org/doi/10.1103/PhysRevLett.91.057901`.

[109] Xiang-Bin Wang. “Beating the Photon-Number-Splitting Attack in Practical Quantum Cryptography”. In: *Phys. Rev. Lett.* 94 (23 2005), p. 230503. DOI: `10.1103/PhysRevLett.94.230503`. URL: `https://link.aps.org/doi/10.1103/PhysRevLett.94.230503`.

[110] Daniel Gottesman et al. “Security of quantum key distribution with imperfect devices”. In: *Information Theory, 2004. ISIT 2004. Proceedings. International Symposium on*. IEEE. 2004, p. 136.

[111] Hoi-Kwong Lo and Hoi Fung Chau. “Unconditional security of quantum key distribution over arbitrarily long distances”. In: *science* 283.5410 (1999), pp. 2050–2056.

[112] Peter W. Shor and John Preskill. “Simple Proof of Security of the BB84 Quantum Key Distribution Protocol”. In: *Phys. Rev. Lett.* 85 (2 2000), pp. 441–444. DOI: `10.1103/PhysRevLett.85.441`. URL: `https://link.aps.org/doi/10.1103/PhysRevLett.85.441`.

[113] Hoi-Kwong Lo, Hoi Fung Chau, and Mohammed Ardehali. “Efficient quantum key distribution scheme and a proof of its unconditional security”. In: *Journal of Cryptology* 18.2 (2005), pp. 133–165.

[114] Masato Koashi. “Simple security proof of quantum key distribution via uncertainty principle”. In: *arXiv preprint quant-ph/0505108* (2005).

[115] Michael A Nielsen and Isaac L Chuang. “Quantum computation and quantum information”. In: *Quantum* 546 (2000), p. 1231.

[116] Tian Zhong et al. “Photon-efficient quantum key distribution using time–energy entanglement with high-dimensional encoding”. In: *New Journal of Physics* 17.2 (2015), p. 022002.

[117] Jake A Smith and Lev Kaplan. “Approaching near-perfect state discrimination of photonic Bell states through the use of unentangled ancilla photons”. In: *arXiv preprint arXiv:1802.10527* (2018).

[118] Sandeep K Goyal et al. “Qudit-teleportation for photons with linear optics”. In: *Scientific reports* 4 (2014), p. 4543.

[119] Miloslav Dušek. "Discrimination of the Bell states of qudits by means of linear optics". In: *Optics communications* 199.1-4 (2001), pp. 161–166.

[120] Olga Shevchuk, Gary A Steele, and Ya M Blanter. "Strong and tunable couplings in flux-mediated optomechanics". In: *Physical Review B* 96.1 (2017), p. 014508.

[121] Eun-jong Kim, J. R. Johansson, and Franco Nori. "Circuit analog of quadratic optomechanics". In: *Phys. Rev. A* 91 (3 2015), p. 033835. DOI: `10.1103/PhysRevA.91.033835`. URL: `https://link.aps.org/doi/10.1103/PhysRevA.91.033835`.

[122] Sungkun Hong et al. "Hanbury Brown and Twiss interferometry of single phonons from an optomechanical resonator". In: *Science* 358.6360 (2017), pp. 203–206.

[123] Momtchil Peev et al. "The SECOQC quantum key distribution network in Vienna". In: *New Journal of Physics* 11.7 (2009), p. 075001.

[124] Masahide Sasaki et al. "Field test of quantum key distribution in the Tokyo QKD Network". In: *Optics express* 19.11 (2011), pp. 10387–10409.

[125] Damien Stucki et al. "Long-term performance of the SwissQuantum quantum key distribution network in a field environment". In: *New Journal of Physics* 13.12 (2011), p. 123001.

[126] Giuseppe Vallone et al. "Experimental Satellite Quantum Communications". In: *Phys. Rev. Lett.* 115 (4 2015), p. 040502. DOI: `10.1103/PhysRevLett.115.040502`. URL: `https://link.aps.org/doi/10.1103/PhysRevLett.115.040502`.

[127] Sheng-Kai Liao et al. "Long-distance free-space quantum key distribution in daylight towards inter-satellite communication". In: *Nature Photonics* 11.8 (2017), p. 509.

[128] Hideki Takenaka et al. "Satellite-to-ground quantum-limited communication using a 50-kg-class microsatellite". In: *Nature photonics* 11.8 (2017), p. 502.

[129] M Lucamarini et al. "Overcoming the rate–distance limit of quantum key distribution without quantum repeaters". In: *Nature* 557.7705 (2018), p. 400.

[130] Bas Hensen et al. "Loophole-free Bell inequality violation using electron spins separated by 1.3 kilometres". In: *Nature* 526.7575 (2015), p. 682.

[131] Norbert Kalb et al. "Entanglement distillation between solid-state quantum network nodes". In: *Science* 356.6341 (2017), pp. 928–932.